

UC Berkeley

UC Berkeley Electronic Theses and Dissertations

Title

Amorphous Silicon-Carbon Nanostructure Photovoltaic Devices

Permalink

<https://escholarship.org/uc/item/5z2810x8>

Author

Schrive, Maria Christine

Publication Date

2012

Peer reviewed|Thesis/dissertation

Amorphous Silicon-Carbon Nanostructure Photovoltaic Devices

by

Maria Christine Schriver

A dissertation submitted in partial satisfaction of the

requirements for the degree of

Doctor of Philosophy

in

Mechanical Engineering

in the

Graduate Division

of the

University of California, Berkeley

Committee in charge:

Professor Lydia Sohn, Co-Chair

Professor Alex Zettl, Co-Chair

Professor Michael Crommie

Professor Liwei Lin

Fall 2012

Amorphous Silicon-Carbon Nanostructure Photovoltaic Devices

Copyright 2012

by

Maria Christine Schriver

Abstract

Amorphous Silicon-Carbon Nanostructure Photovoltaic Devices

by

Maria Christine Schriver

Doctor of Philosophy in Mechanical Engineering

University of California, Berkeley

Professor Lydia Sohn, Co-Chair

Professor Alex Zettl, Co-Chair

A novel solar cell architecture made completely from the earth abundant elements silicon and carbon has been developed. Hydrogenated amorphous silicon (aSi:H), rather than crystalline silicon, is used as the active material due to its high absorption through a direct band gap of 1.7eV, well matched to the solar spectrum to ensure the possibility of improved cells in this architecture with higher efficiencies. The cells employ a Schottky barrier design wherein the amorphous silicon absorber layer generates electron-hole pairs from incoming photons and holes are preferentially extracted through a metallic material consisting of a carbon nanostructure. Both graphene and buckypaper were used as the metallic component of the Schottky junction to effectively convert incoming light to electricity.

Subsequent work focused on graphene-based cells because graphene offers better transparency and conductance compared to buckypaper, making it promising as a top conductor in a solar cell. Reactions of the graphene-aSi:H interface were investigated and strategies developed to minimize reactions that lead to performance degradation. Finally, photon management strategies were executed to significantly enhance the performance of the cells using silver nanoparticles to increase the absorbance of light and extraction of charges in a thin aSi:H film. Solar cells optimized with these improvements show performance enhancements of 1-2 orders of magnitude compared to initially published cells in this architecture.

In addition to yielding strategies for improved protection and performance of the solar cells presented in this thesis, investigations presented here into reactions at the graphene-silicon interface should inform further research into applications of graphene.

Contents

List of Figures	iii
List of Tables	vii
1 Introduction	1
2 Amorphous Silicon Material	3
2.1 Background	3
2.1.1 Hydrogenated Amorphous Silicon as a Photovoltaic Material .	3
2.1.2 Deposition Methods	5
2.1.3 Staebler-Wronski Effect	7
2.2 Pressure Experiments	8
3 Carbon Nanomaterials: Buckypaper and Graphene	11
3.1 Graphene	11
3.1.1 Structure	11
3.1.2 Properties	11
3.1.3 Growth Methods	13
3.1.4 Applications	14
3.2 Buckypaper	16
3.2.1 Fabrication	16
3.2.2 Properties	19
4 Photovoltaics	20
4.1 Motivation and Material Choice	20
4.2 Economics	24
4.3 Physics of Photovoltaics	24
4.3.1 Thermodynamic Approach	26
4.3.2 Processes	30
4.3.3 Equivalent Circuit	30
4.4 Amorphous Silicon-Carbon Nanostructure Solar Cells	34
4.4.1 Fabrication	34

4.4.2	Photovoltaic Model	35
4.4.3	Performance	37
4.4.4	Future Direction	45
5	Oxidation and Reduction Reactions and the Graphene-Substrate Interface	47
5.1	Introduction	47
5.2	Copper Foil Oxidation	47
5.3	Electronic and Photovoltaic Performance	50
5.4	Experimental Details	57
5.5	Conclusion	58
6	Photon Management	59
6.1	Light Trapping Theory	59
6.2	Light Trapping in aSi:H	63
6.3	Device Fabrication	64
6.4	Results and Discussion	66
6.4.1	Performance	66
6.4.2	Spectral Performance	72
6.5	Conclusion	74
7	Conclusion	76
	Bibliography	77

List of Figures

2.1	Hydrogenated amorphous silicon structure. Silicon atoms (gray) try to be tetrahedrally bonded, but lack of order strains bonds and leaves some atoms with 3 or 5 bonds instead of 4. Hydrogen atoms saturate some dangling bonds to reduce charge trapping[41].	4
2.2	Curve showing theoretically achievable efficiencies (curve) and actual device efficiencies (points) for various materials. Although aSi:H performs poorly compared to cSi in devices, the potential efficiency just based on the band gap is nearly as high[54].	6
2.3	Schematic showing experimental process for applying monodirectional compressive or expansive stress to a thin aSi:H film.	8
2.4	Results of pressure experiment. Compressive pressure, or rolling the foil with the active material to the inside, results in increased conductance. Expansive strain results in decreased conductance.	9
3.1	Monolayer graphene is a single layer of carbon atoms in a honeycomb structure. A few layers of this structure is called multilayer graphene, but tens or hundreds of layers behaves as bulk graphite[75].	12
3.2	Monolayer graphene dispersion relation. The points where the conduction and valence band touch at one point are the K points and here the dispersion relation is linear near the intersection. This is in contrast to semiconductors, which have parabolic dispersion relations near the conduction band minima and valence band maxima[53].	13
3.3	Raman spectrum of mono-layer and few layer graphene. Raman is an effective way to identify graphene and to differentiate between single and few layer films[64].	14
3.4	Growth process used for graphene films in this thesis. An in initial hydrogen anneal cleans the copper surface and increases grain size in the substrate. A low methane flow stage causes slow nucleation relative to grain growth, leading to large grains but not a continuous film. The final high methane flow stage fills in any gaps between grains to create a continuous film.	15
3.5	Photographic image of buckypaper on filter paper.	17

3.6	Scanning electron micrograph of buckypaper showing individual nanotubes.	18
3.7	Ultraviolet and visible transmission spectrum of buckypaper prepared as described above and deposited on a glass slide.	19
4.1	Chart showing the most, and least, abundant elements in the earth's crust as a fraction of the abundance of silicon[69].	21
4.2	Historical data and future predictions by the European Photovoltaics Industry Association for annual photovoltaics installations globally[5].	22
4.3	Total global energy use using past data and predicted future needs. From the Energy Information Administration[2].	23
4.4	Recent reductions in costs for installed photovoltaic systems. This graph shows the cost of a standard system, not the least expensive available system. Costs need to continue to decline to \$ per Watt to compete with fossil fuel derived electricity production[57].	25
4.5	Chart showing necessary maximum installed PV costs (\$/MW) to compete with current grid prices for various geographic areas. The price depends on available daily insolation, linked to geography, in addition to current grid prices[6].	26
4.6	The most fundamental model of a solar cell is an absorber, which converts light energy into electrochemical energy, and contacts, which convert electrochemical energy into usable electrical energy (voltage and current).	27
4.7	Diagram showing where three fundamental photovoltaic processes occur in a Schottky barrier solar cell.	31
4.8	Equivalent circuit diagram for a solar cell.	31
4.9	Current-voltage characteristics of a solar cell.	33
4.10	A schematic of device structure. aSi:H is PECVD deposited on patterned ITO substrates. Either SiO ₂ or Al ₂ O ₃ is deposited on top, and a window is patterned and etched. A carbon film is deposited over the window.	36
4.11	Optical micrographs of devices. Both are taken at the same magnification. Side length of the square window is 500 μ m.	36
4.12	Approximate band diagram for a Schottky barrier aSi:H-carbon nanostructure solar cell.	37
4.13	Solar simulator setup used to measure solar cells in this thesis.	38
4.14	Conductance of plain graphene (above) and buckypaper (below) films.	39
4.15	Current-voltage curves for initial tests of crystalline silicon-graphene junctions. Top is n-type silicon, which makes a working junction. Bottom is p-type, which does not.	40
4.16	Current-Voltage curves for both buckypaper and graphene cells in the dark.	41

4.17	Current-Voltage curves for both buckypaper and graphene cells illuminated by $135\text{mW}/\text{cm}^2$	43
4.18	Current-Voltage curve for a buckypaper cell over a large voltage range.	44
4.19	Transmission electron micrograph of a single carbon nanotube coated with 30nm of amorphous silicon. The right-hand image is false colored based on elemental abundance in the material.	46
5.1	Graphene transferred onto bare copper foil and oxidized at room temperature and pressure for several weeks. Oxidation is more pronounced where graphene is present.	48
5.2	Raman spectrum of graphene transferred to copper foil indicating graphene is intact.	49
5.3	Sequence of oxidation of copper foil with graphene grown on it. Oxidation and reduction happen readily through the single as-grown layer, but transfer of a second layer of graphene protects from further oxidation.	51
5.4	Schematic of device to investigate aluminum oxidation rate underneath graphene.	52
5.5	Conductance degradation in aluminum contacts over timescales of many minutes.	53
5.6	Performance degrades over time with only one layer of graphene due to oxidation of the silicon surface.	55
5.7	Bi-sheet graphene offers more protection from oxidation, slowing degradation.	56
5.8	XPS results showing equal amounts of silicon dioxide on bare and graphene-coated silicon wafer substrates.	57
6.1	Diagram showing light trapping. Light is redirected horizontally so it spends more time in the solar cell. Figure a shows a strategy for use in relatively thick films of several microns or more. Micron-scale texturing reflects light at many angles. Figure b shows a strategy suited for thinner films. Metal nanoparticles scatter the light plasmonically with significant enhancement of the electric field near the nanoparticle film.	60
6.2	Diagram showing how surface plasmon resonance occurs in small metal nanoparticles. Incoming light has an oscillating electric field which forces free electrons in the particle to oscillate. If the frequency of the light matches the natural frequency for charge oscillation in the particle, resonance occurs.	62
6.3	Deposition process for tri-sheet graphene (TSG).	65
6.4	Raman spectrum of tri-sheet graphene (TSG). Some areas look like mono-layer graphene (c) while some look like few-layer graphene (b).	67

6.5	A schematic of device structure. 12 separate devices are fabricated in parallel by patterning 12 back contacts, then depositing aSi:H, graphene, and finally silver nanoparticles.	68
6.6	SEM micrographs of a device with silver nanoparticles deposited by thermal evaporation of 5nm thick silver film. (a) shows particle sizes. (b) and (c) show abrupt borders between domains of different particle sizes. (d) shows large-area variability and domain size.	69
6.7	Short circuit current and efficiency in cells with and without silver nanoparticles. Data points on the left-hand side represent individual control devices, while those on the right represent experimental devices with silver nanoparticles.	70
6.8	Comparison of open circuit voltage and fill factor performance for control and experimental devices.	71
6.9	External quantum efficiency (EQE) enhancements for devices with silver nanoparticles compared to average control device EQE.	72
6.10	Absorption enhancement in 30nm aSi:H coated with tri-sheet graphene and silver nanoparticles, compared to 30nm aSi:H with no top coating.	74
6.11	Calculated path length enhancement in arbitrarily thin aSi:H coated with tri-sheet graphene and silver nanoparticles, compared to aSi:H with only graphene.	75

List of Tables

2.1	aSi:H PECVD deposition parameters	6
4.1	Solar cell properties	34
4.2	Photolithography parameters	35
4.3	Table of respective properties of graphene- and buckypaper-aSi:H solar cells	42
5.1	Conditions used for RIE "descum" process before HF etch, reduction anneal, and graphene deposition.	54
5.2	Table comparing performance degradation for mono- and bi-sheet graphene devices with n-type crystalline silicon. All entries are efficiency in percent.	54
5.3	XPS results. Peak sizes can be compared between MSG and BSG, but comparisons between peak sizes for different elements in the same sample are not meaningful. Peak sizes are in arbitrary units and are calculated using an Excel model to iteratively find the best Gaussian fit to data with units of counts per binding energy interval.	57

Acknowledgments

I want to thank my advisor, Alex Zettl, and his entire research group. The environment of curiosity about physics and excitement to try numerous experiments that were clearly never going to work, except when one did, has been inspiring. Thanks to this environment, the group is interdisciplinary and I have benefited from discussing scientific issues from the perspectives of those in several different fields, which always deepens my understanding. In particular, my co-authors on publications Will Regan, Anna Zaniewski, and Matthias Loster have contributed to hours of enlightening conversation.

I further thank individuals who have supported me with data collection including Alex Luce for UV-vis absorption, Danny Hellebusch for XPS, Matthias Loster for TEM.

The qualifying exam process was instrumental to motivating me to actually learn the physics behind my project and I thank everyone who was part of it. My committee of Liwei Lin, Mike Crommie, Van Carey, and Catherine Wolfram. And my practice committee members Jessy Rivest, Benji Aleman, and Jay James. These students were chosen as part of my practice committee because they had been excellent sounding boards for research thoughts and always supportive of me.

The Photovoltaics Idealab was an important source of feedback for me early in my research process, and an opportunity to learn about other photovoltaics research and how my work fit. Thank you to all PV Idealab members, and especially its founder Cyrus Wadia and subsequent leadership teams including Jessy Rivest, Anna Goldstein, Andy Zheng, and Danny Hellebusch.

The SEED program has been an extraordinarily important part of my PhD process. My experiences with this program were a constant reminder of the greater world my research can serve as well as a source of perspective when I had a particularly frustrating experiment. I thank everyone who worked with me on SEED, especially Jay James, Danny Hellebusch, Anna Goldstein, Vince Romanin, and Jeff Crosby.

I thank each member of my thesis committee for their work on this thesis in reading and feedback. Lydia Sohn, Mike Crommie, Liwei Lin, and Alex Zettl, without whom I would not have finished this process. The actual writing of the thesis has been a process of cementing what I've learned over the last 5 years, and discovering how much I have, indeed learned.

Finally, I thank my parents for always making education a top priority. Not realizing that college attendance was a choice until after I matriculated was definitely part of my ultimate decision to attend graduate school and to finish, even when the end seemed too far away. The value of learning they instilled in me has served me throughout my education and will continue to guide how I use this degree.

Chapter 1

Introduction

Pollution caused by use of fossil fuels for energy threatens us in several ways. Climate change due carbon dioxide emissions is already leading to extreme weather events threatening our food supply, homes, and human lives. These consequences promise to multiply in frequency and magnitude over the coming decades. Mercury emissions from coal poison fish supplies and smog and particulate emissions from all kinds of combustion elevate levels of respiratory illnesses. As we exhaust the most accessible sources of oil, coal, and natural gas we extract these resources from new sources at even greater economic and environmental costs. Extraction of natural gas via fracking or of tar sands via destruction of pristine wilderness creates new threats to our personal and environmental health. Moreover, dependence on fossil fuels means dependence on countries where oil is plentiful regardless of the political consequences of those alliances. Clean, renewable alternatives to fossil fuels are an opportunity to mitigate these impacts. On a philosophical level, we can do better than burning up everything we can find underground to maintain our lifestyle.

Photovoltaics are one way to do better. A photovoltaic cell, or solar cell, is a device that converts light into electricity. The sun provides more energy in the form of light than humans use globally for electricity, transportation, and industry by a factor of ten thousand. Moreover using renewable resources like solar and wind energy enforces sustainability. There is no way to use tomorrow's sunlight today. Even if we create a world with ten thousand times the energy demand we have today, we will not be able to use up sunlight; we will be forced to conserve it by constraining our energy demand to meet the energy supplied each day. And then there will be more tomorrow.

Of course, photovoltaics are only one piece of the solution at the present time. The sun does not shine constantly. Not only is half of the earth shaded at any time, but passing clouds can cause order of magnitude changes in local sunlight intensity. In order to have electricity when we need it and use only the sun as a source, we would need to store energy in some form and currently commercially available storage strategies all have significant limitations in capacity, efficiency, or cost. However, we

currently produce less than 1% of global energy demand directly from the sun[5], and much more is possible before large-scale storage is necessary. Research into photovoltaic technologies that improve upon current solutions by being lower cost, easier to produce and install, or more scalable is a necessary investment to accelerate the expansion of this industry.

My research focuses on one photovoltaic absorber material, hydrogenated amorphous silicon (aSi:H). I focus on aSi:H because it has potential to offer high efficiency, low-cost solar cells. Thermodynamic limits allow aSi:H absorbers to convert a high fraction of incoming light to electricity compared to many other semiconductors. aSi:H has been used as a solar cell material for 4 decades and low-cost deposition and processing methods have been proven[10, 21, 54]. The limitation on the performance of these commercially available cells is the poor electronic transport in the material and the consequent inability to extract high energy electrons. My research addresses this problem specifically by outlining a strategy for development of thinner absorber layers that aid in charge extraction.

I developed a novel solar cell architecture which combines aSi:H with graphene, or single-layer graphite, to make a junction which converts incoming light to electrical power. I then investigated the performance of this device structure, the susceptibility of the interface to reaction with its external environment, strategies for protecting the interface from reaction and consequent degradation, and the potential for improvement via established strategies for light trapping. Light trapping refers to redirecting incoming light so it spends more time within the absorbing layer of the cell.

This thesis will first discuss the two materials used in my cells, aSi:H and graphene. I will then introduce solar cell physics and explain the aSi:H-graphene cell architecture and how it leverages this physics. Then I will investigate the reactivity of the interface and ways to protect it from degradation. Finally, I will present promising results for improving cell performance via light trapping with silver nanoparticles.

Further research is necessary to bring these strategies to a place where they can be implemented commercially. It is my hope that the results presented here inspires that research to happen and new solutions to be created.

Chapter 2

Amorphous Silicon Material

2.1 Background

2.1.1 Hydrogenated Amorphous Silicon as a Photovoltaic Material

Hydrogenated amorphous silicon (aSi:H) is silicon with no crystal structure. In crystalline silicon, each silicon atom is bonded tetragonally to exactly four nearest neighbors. In aSi:H, most individual silicon atoms are bonded to four other silicon atoms in an orientation that is close to tetragonal, but not quite. A good way to think about an amorphous material is that if you know the position of one atom, you can predict with good reliability the position of its nearest neighbors. For second nearest neighbors, uncertainties in bond angles and lengths add to each other, and it becomes more difficult to predict. For third nearest neighbors, you know little about their position. In contrast, a crystalline material allows you to predict with near certainty the position of an atom thousands of bond-lengths away from the one you know. A schematic of an amorphous material is shown in figure 2.1[41]. The amorphous silicon is hydrogenated when there is hydrogen present in the deposition process. It naturally bonds to some of the 3-fold bonded silicon atoms, resulting in an atomic percentage hydrogen content from 14-22%[76].

Hydrogenated amorphous silicon has promise as a photovoltaic material. When compared to crystalline silicon, which currently comprises 80-90% of the solar cell market[58], amorphous silicon is capable of absorbing most or all incident light with a much thinner absorber layer. This is due to its status as a direct band-gap semiconductor. Crystalline silicon is an indirect band gap semiconductor, meaning the top of the valence band and the bottom of the conduction band are at different momenta and a phonon is required to move an electron across this lowest energy transition. For

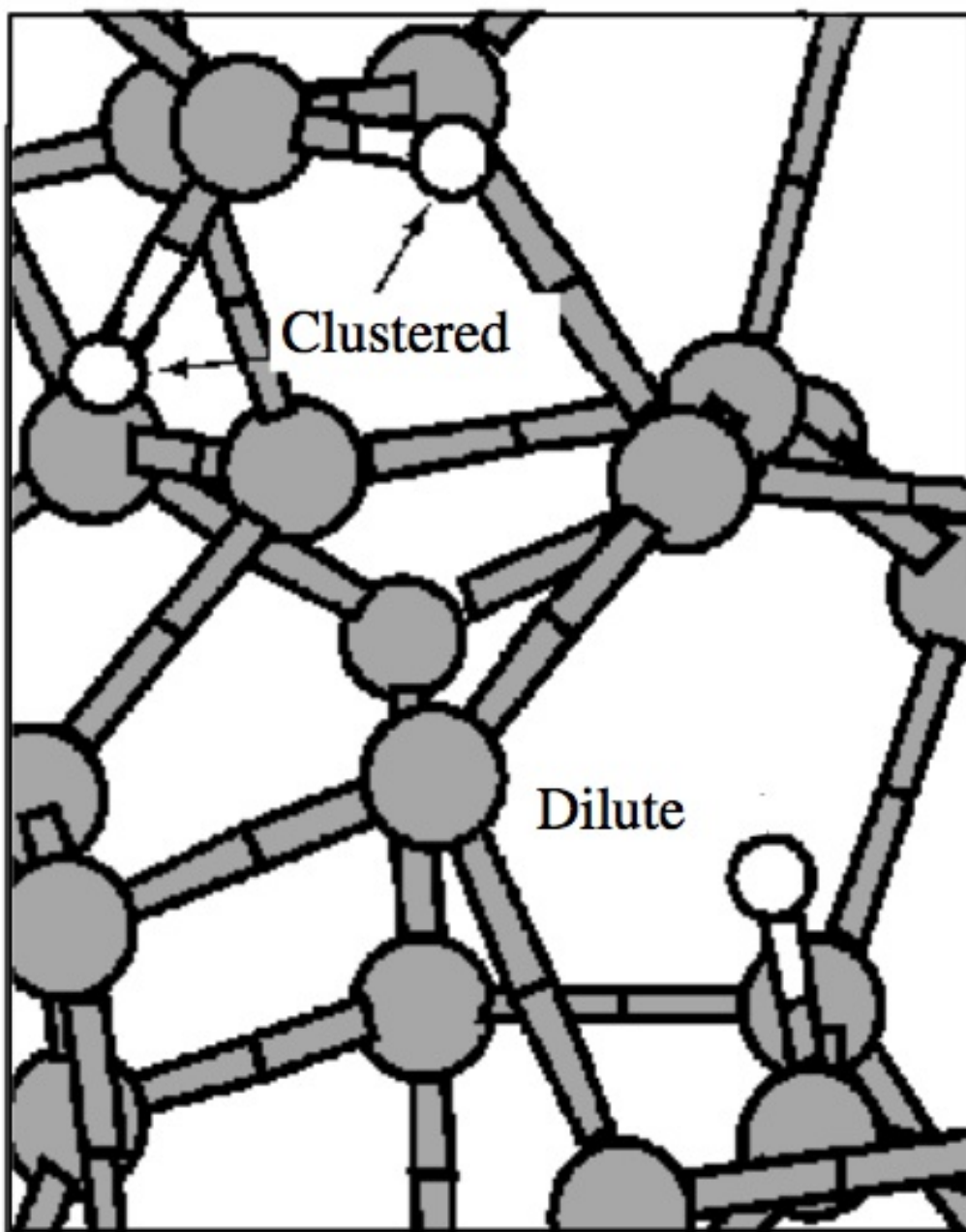


Figure 2.1: Hydrogenated amorphous silicon structure. Silicon atoms (gray) try to be tetrahedrally bonded, but lack of order strains bonds and leaves some atoms with 3 or 5 bonds instead of 4. Hydrogen atoms saturate some dangling bonds to reduce charge trapping[41].

crystalline silicon, the consequence is very weak absorption of photons with energies near the band gap, meaning that 10-100 microns, at minimum, of crystalline silicon are required for full incident light absorption. In contrast, less than one micron of aSi:H is used for full absorption[54].

In addition, the Shockley-Queissar maximum theoretical efficiency for aSi:H is nearly equal to that for crystalline silicon. The Shockley-Queissar limit is based on the matching of a semiconductor band gap to the solar spectrum[56]. Photons with energies below the band gap are not absorbed, while those with energies above create one electron-hole pair with the same energy as the band gap, but lose the rest of their energy to thermalization. A balance between these two processes predicts maximum possible efficiency for a single band-gap solar cell of around 31% at a band gap near 1.2eV. Crystalline silicon has a band gap at 1.1 eV, close to this ideal. With a band gap of 1.7eV, aSi:H is a little farther away, but this does not reduce its maximum possible efficiency significantly. Figure 2.2 shows crystalline and amorphous silicon solar cell band gaps and achieved efficiencies, along with a curve showing the theoretical efficiency for each band gap. This figure uses the theoretical limit adjusted for the real solar spectrum, rather than the blackbody solar spectrum the Shockley-Queissar limit is calculated for[54].

However aSi:H has significant weaknesses as a photovoltaic material that this thesis seeks to address. Charge carrier mobilities are up to three orders of magnitude smaller than in crystalline silicon [60]. In addition, the amorphous nature of the material means many silicon atoms are bonded to only 3 others or to 5. 3-fold bonded silicon atoms introduce dangling bonds, which trap charge. 5-fold bonded atoms introduce significant local strain, which can also trap charge. This means that while electrons and holes diffuse easily through hundreds of microns of crystalline silicon, the diffusion length in amorphous silicon is on the order of just 10nm[50]. If charges are not extracted in this short distance from where they are generated, they will be trapped and the photon energy used to generate them will be lost. This explains aSi:H solar cells' failure to come close to their theoretical maximum efficiency.

2.1.2 Deposition Methods

aSi:H is most often deposited by plasma-enhanced chemical vapor deposition (PECVD). In this process, silane (SiH_4) flows into a chamber and is ionized by a radio-frequency voltage. Small amounts of phosphine (PH_3) or diborane (B_2H_3) can be added to dope the material n-type or p-type, respectively[21].

The PECVD recipe used for films in this thesis is outlined in Table 2.1.

aSi:H solar cells are usually deposited using a p-i-n structure. This is because doped aSi:H performs poorly and this structure minimizes the volume occupied by

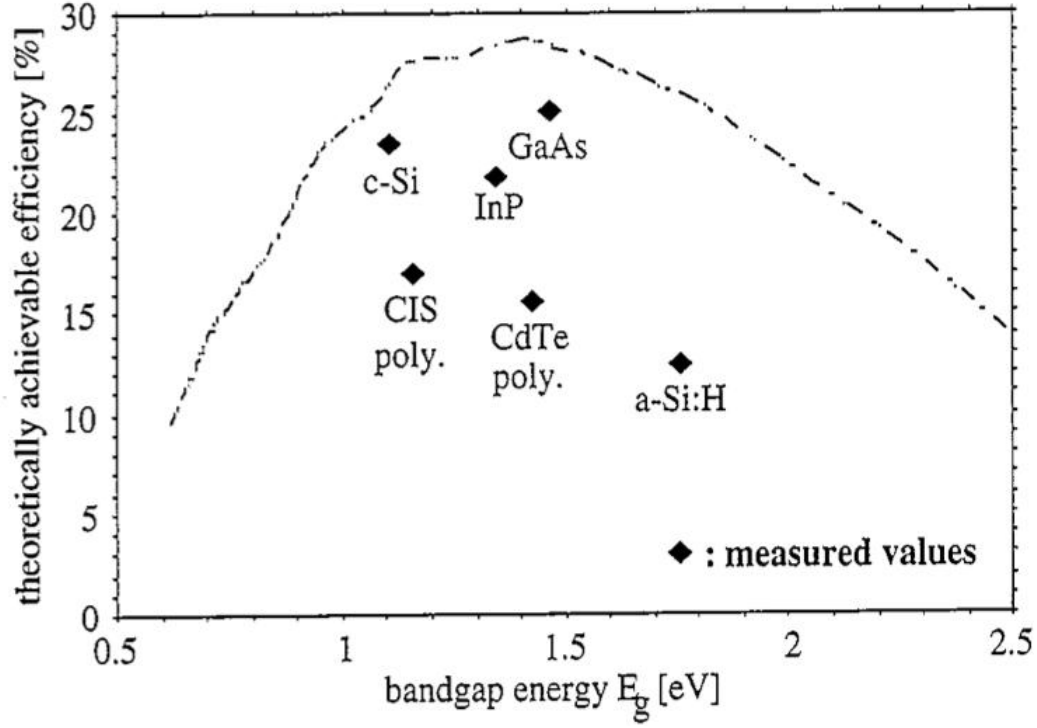


Figure 2.2: Curve showing theoretically achievable efficiencies (curve) and actual device efficiencies (points) for various materials. Although aSi:H performs poorly compared to cSi in devices, the potential efficiency just based on the band gap is nearly as high[54].

Table 2.1: aSi:H PECVD deposition parameters

Temperature	350°
Silane Flow	100 sccm
Argon Flow	400 sccm
Pressure	900 mTorr
Deposition Rate	38.71 nm/minute
Power	100W
Chamber Diameter	300mm
Chamber Height	600mm
Tool	Oxford Plasmalab 80plus at UC Berkeley Marvell Nanolab

doped regions. In addition, the p-i-n architecture introduces a weak but consistent field across the entire device[54, 21]. Charges generated in the intrinsic region feel a small pull towards one end or the other of the cell which reduces losses by recombination and increases the chances that a charge carrier will reach an interface where it can be extracted.

2.1.3 Staebler-Wronski Effect

The conductivity of aSi:H declines significantly with time when it is exposed to light. The photoconductivity can fall by orders of magnitude over a period of several hours before stabilizing. The consequent decline in photovoltaic efficiency is less dramatic, but still significant. In commercial aSi:H cells, the photon conversion efficiency drops from about 8-10% as-deposited to about 6-8% after light-soaking [21]. The effect can be reversed by relatively mild annealing process in the dark, usually 1-2 hours at 150-200°C[61].

This degradation is known as the Staebler-Wronski Effect, and its mechanism is unknown. Presumably, in the illuminated state more trap states are available to charge carriers and are deeper compared to the dark state. Heating in the dark allows the carriers to escape the traps. However, the specifics of what atomic placements or movements create the trap states is a matter of debate. Many researchers assume that dangling bonds, or silicon atoms that are bonded to only 3 other atoms, are responsible. This assumption is based on the fact that dangling bonds should carry a slight negative charge due to the extra electrons on the central silicon atom not used for bonding and are in general important hole trap sites in aSi:H. The fact that hydrogen saturation, using silane diluted with hydrogen gas as the PECVD precursor, mitigates the Staebler-Wronski Effect seems to support this hypothesis[76, 1]. Extra hydrogen in the precursor gas allows more hydrogen atoms to saturate dangling bonds by bonding to the fourth site on a 3-fold bonded silicon atom without disrupting the rest of the aSi:H matrix. However, new simulations propose a different mechanism linked to bond strain. Significant bond strain is most likely when a silicon atom is 3-fold or 5-fold-bonded, but can also occur with a 4-fold bonded silicon atom when the four bonded atoms cannot arrange themselves tetragonally. Bond strain can create deep hole traps[71]. Minor changes in the structure of the aSi:H upon illumination could lower the overall energy of the structure but create isolated, very deep, hole traps that inhibit conduction and photovoltaic performance. Experimental data shows that amorphous films deposited in conditions closer to those that produce nanocrystalline films are less susceptible to the Staebler-Wronski effect [55, 77]. This suggests that overall crystallinity improvements mitigate the effect, which supports the idea that bond strain is responsible.

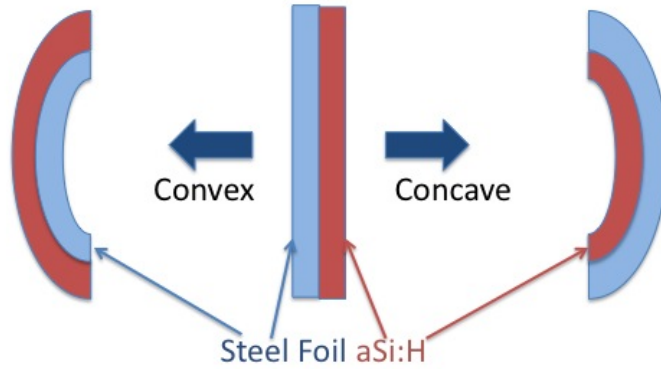


Figure 2.3: Schematic showing experimental process for applying monodirectional compressive or expansive stress to a thin aSi:H film.

2.2 Pressure Experiments

In order to investigate this theory, I tested one of its predictions. If bond strain is an important determiner of trap density and depth, and of conductivity, mechanical strain or induced pressure should affect the conductivity of the film.

I deposited thin amorphous silicon films on commercially available steel foil. The steel served as a back contact, and a lithographically patterned nickel pad served as a top contact. I measured the conductivity through the film with the steel foil flat. Then I carefully rolled the foil around a Bic pen to induce an expansion or compression of the film and measured the conductivity again. A simple schematic is shown in Figure 2.3.

The results indicate that compressive 1-dimensional pressure, accomplished by a concave rolling of the foil substrate, increases conductance. Expansive strain, conversely, decreases conductance.

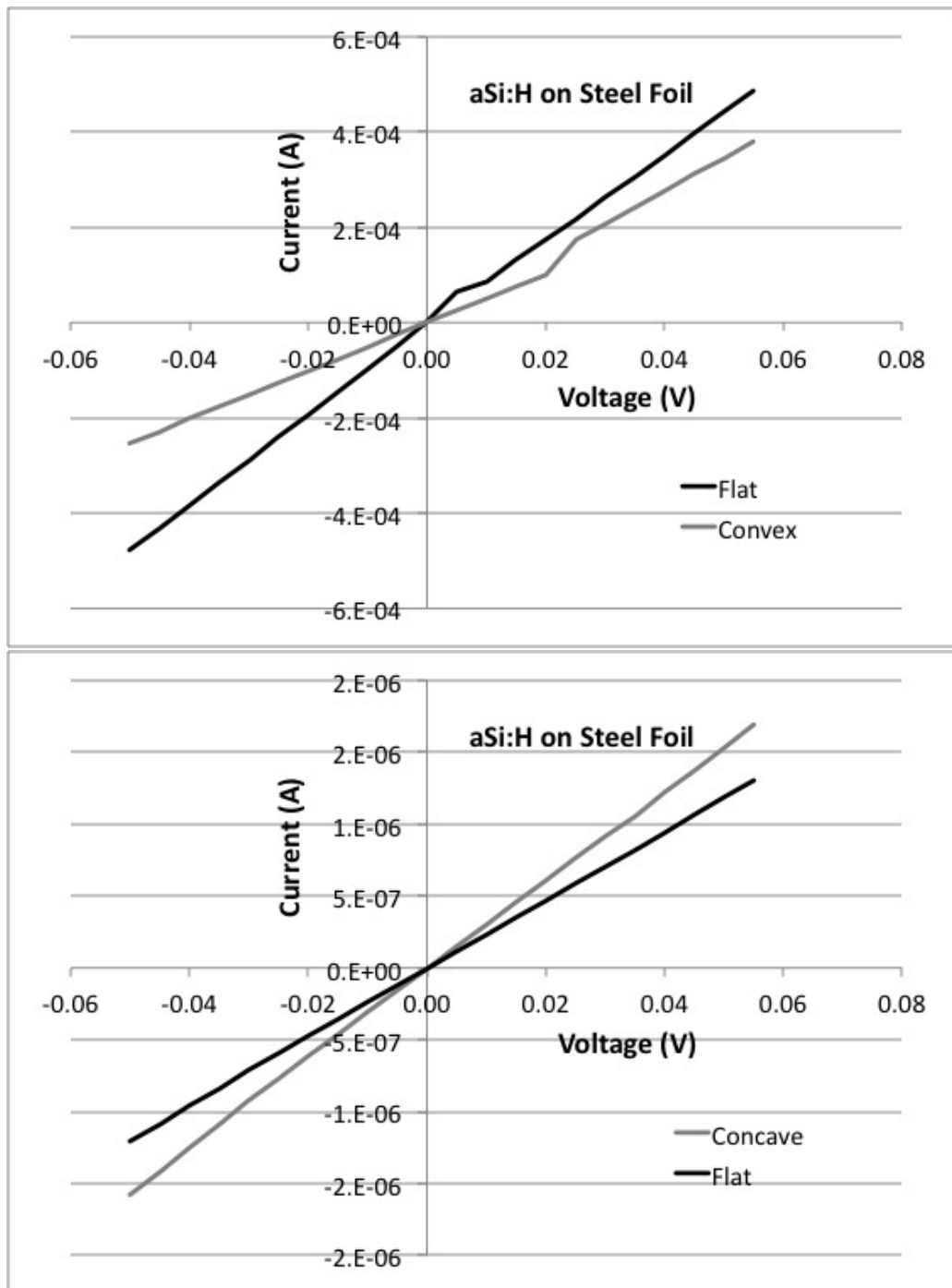


Figure 2.4: Results of pressure experiment. Compressive pressure, or rolling the foil with the active material to the inside, results in increased conductance. Expansive strain results in decreased conductance.

To estimate the total pressure created by these experiments, we consider the radius of the pen, approximately $R = 0.3cm$. We also assume that the foil is wrapped halfway around the pen hemispherically. Then the total distortion of the film in the direction of strain is:

$$L_{Curved} - L_{Flat} = \delta L \quad (2.1)$$

For the convex sample, the initial length, L_{Flat} is just $\pi * R$. The curved length is the hemispherical length around a circle with a radius that extends to the center of the film.

$$L_{Curved} = \pi * (R + t_{foil} + t_{aSi}/2) \quad (2.2)$$

where t_{foil} is the thickness of the foil and t_{aSi} is the thickness of the film. In this case the film is 600nm thick and the foil is 50 μm thick. Substituting into equation 2.1,

$$\delta L = \pi * (0.3cm + 50\mu m + 300nm) - \pi * 0.3cm = 158\mu m \quad (2.3)$$

Which is a strain of $\epsilon = \frac{\delta L}{L} = 0.0167$. Using a Young's Modulus for aSi:H of 146GPa, I calculate a stress of

$$\sigma = 0.0167 * 146GPa = 2.4GPa \quad (2.4)$$

This is a substantial pressure that would be difficult to sustain in a practical application of a solar cell. However, the experiment demonstrates that overall strain does affect the conductivity of aSi:H films and it is reasonable that strain of individual bonds may be responsible for degradation in conductivity.

Chapter 3

Carbon Nanomaterials: Buckypaper and Graphene

3.1 Graphene

3.1.1 Structure

Monolayer graphene is a single layer of carbon atoms in a honeycomb structure as shown in 3.1[75]. Tight binding calculations of the band structure reveal a dispersion relation with a band gap of zero electronvolts at zero momentum and linear band edges near the conduction band minimum/valence band maximum. The three dimensional band structure is shown in 3.2[53]. Electrons fill the band structure up to the top of the valence band. This is an uncommon band structure. Metals have an unfilled band, while semiconductors have a finite gap in energy between the valence and conduction bands. Because graphene has a finite band gap at non-zero momentum, electrons are inhibited from easily entering the conduction band, but because the gap is zero at zero momentum, it is possible to generate conduction electrons with infinitesimal energy input. Thus, the conductivity is higher than in a semiconductor, but lower than in a metal. Graphene is classified as a semimetal.

3.1.2 Properties

In addition to being somewhat conductive, around $500\text{-}1000\ \Omega/\square$, monolayer graphene is nearly transparent. Through the visible range, transmittance averages 93%[43]. This is a useful property for application in conducting films that go on top of solar cells or displays and need to allow light to pass through.

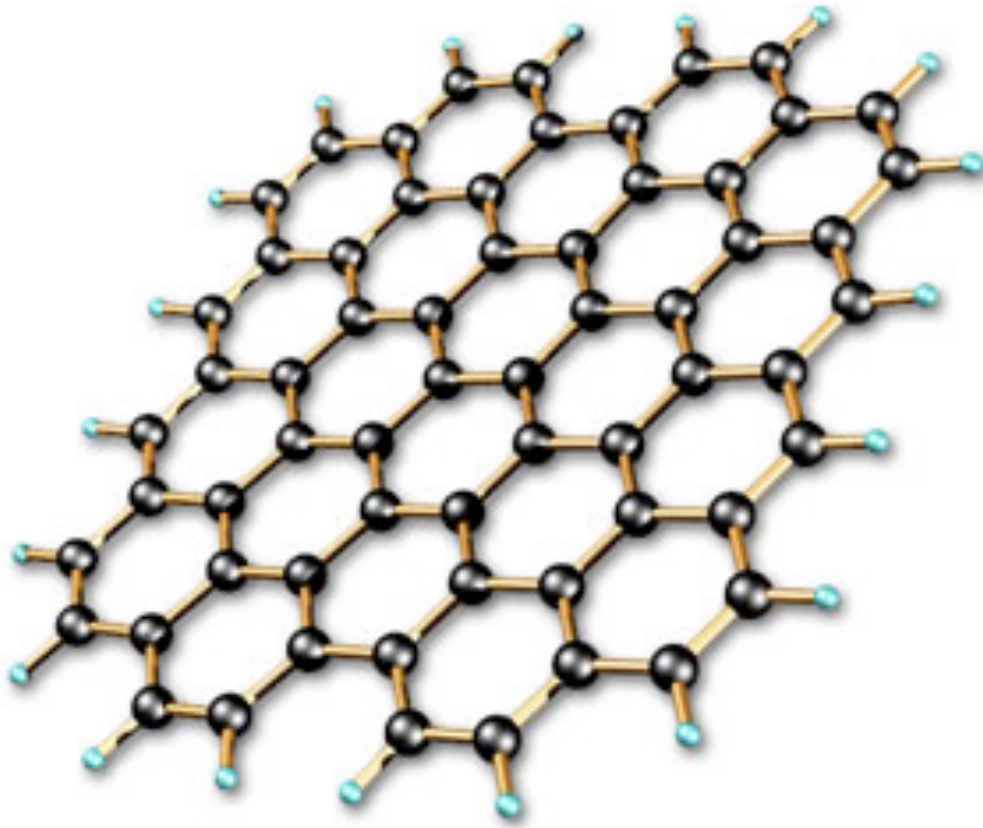


Figure 3.1: Monolayer graphene is a single layer of carbon atoms in a honeycomb structure. A few layers of this structure is called multilayer graphene, but tens or hundreds of layers behaves as bulk graphite[75].

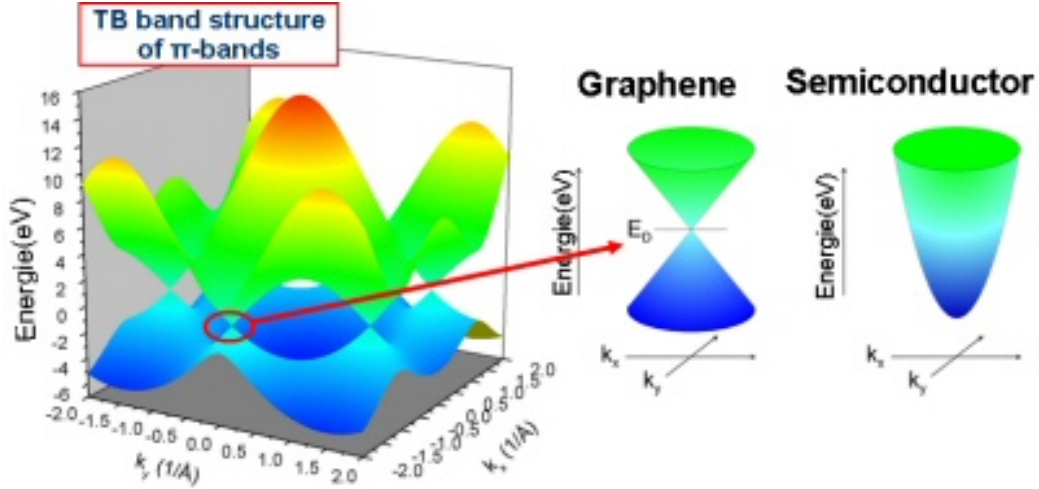


Figure 3.2: Monolayer graphene dispersion relation. The points where the conduction and valence band touch at one point are the K points and here the dispersion relation is linear near the intersection. This is in contrast to semiconductors, which have parabolic dispersion relations near the conduction band minima and valence band maxima[53].

Graphene can also be grown in multiple layers, and up to 10 layers is generally referred to as multilayer graphene. Bilayer graphene becomes semiconducting in the presence of an electric field. Imposing additional boundary conditions on the electron wavefunction within graphene by constraining it to few-nm strips, called graphene nanoribbons, can open a bandgap up to a few eV for very thin ribbons[7, 59, 51, 25].

Graphene is usually identified by its distinct Raman spectrum, shown in Figure 3.3. Mono- and multilayer graphene can be distinguished based on the Raman spectra[64].

3.1.3 Growth Methods

Early experiments on graphene focused on exfoliated graphene. In this process, transparent tape is used to peel single atomic layers from chunks of high quality graphite and then deposit them on silicon, silicon dioxide, or another substrate. Exfoliation can produce extremely high quality graphene flakes, but the size of a continuous sheet is limited, usually to less than a centimeter[47]. In 2008, a chemical vapor deposition (CVD) process for graphene growth was developed[35, 44]. A carbon-containing gas, usually methane but sometimes an alcohol, hexane, or other organic vapor, flows over a catalyst metal at high temperature. The carbon sticks to the catalyst and eventually forms grains of graphene. Temperatures around 1000°C

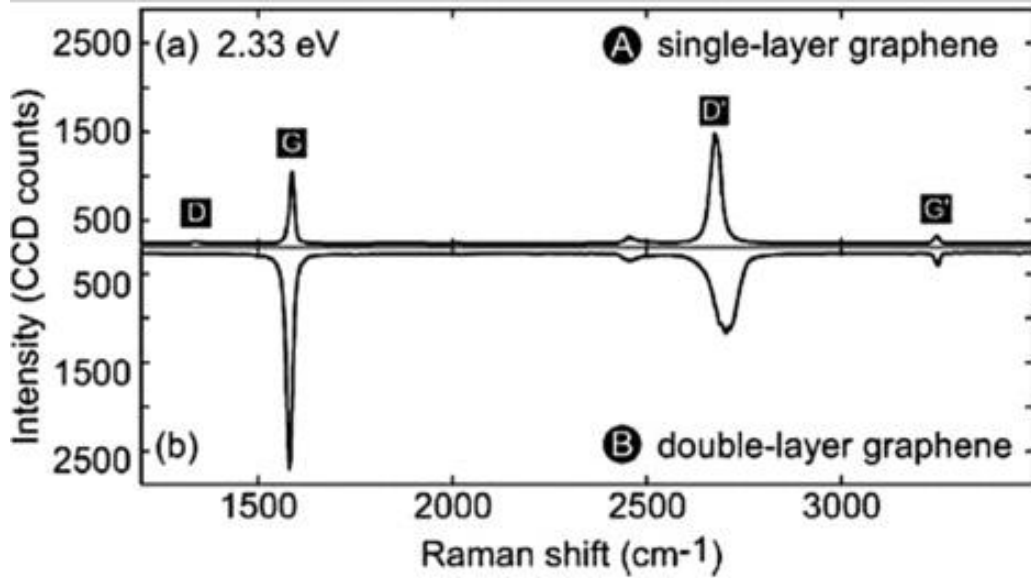


Figure 3.3: Raman spectrum of mono-layer and few layer graphene. Raman is an effective way to identify graphene and to differentiate between single and few layer films[64].

are necessary for this process. Usually copper is used for single layer graphene and nickel for multilayer films, but steel and other metals have also been used.

I used a two-stage process that improves on the original CVD growth for the graphene in this thesis. The two-stage process takes advantage of the fact that the nucleation rate to crystal growth rate ratio depends on the flow rate of methane. During the first stage, a low flow rate of methane nucleates a small number of grains and then they grow. Nucleation is very slow compared to crystal growth in this regime, so the result is few grains which can then grow to a relatively large size. However, this flow rate will not result in complete coverage of the copper film. In order to fill in the areas between the large grains, a high flow rate of methane is applied at the same temperature during the second part of the growth[36]. The details of the growth process used in this thesis are shown in Figure 3.4.

3.1.4 Applications

Graphene holds promise in many applications as an atomically thin transparent conductor. CVD-grown graphene was being used to make commercial-size LCD displays within a year after its discovery[62]. Graphene has been tested as a transparent top contact for solar cells, replacing relatively expensive indium tin oxide layers, in addition to being tested as an active component of the solar cell as in this thesis.

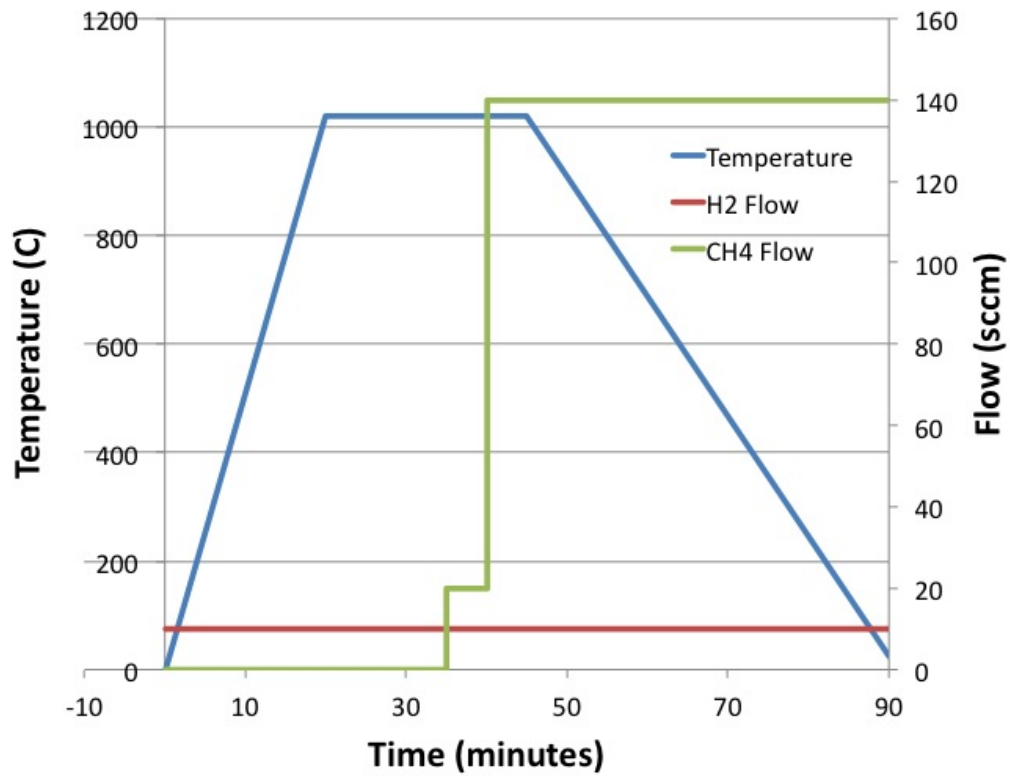


Figure 3.4: Growth process used for graphene films in this thesis. An initial hydrogen anneal cleans the copper surface and increases grain size in the substrate. A low methane flow stage causes slow nucleation relative to grain growth, leading to large grains but not a continuous film. The final high methane flow stage fills in any gaps between grains to create a continuous film.

Because graphene is a single atomic layer, it provides some screening and electronic modification to a surface. While it may not entirely prevent the surface from reacting with its environment and may catalyze corrosion in some cases, it may have applications in surface modification and corrosion control in harsh environments[48, 66, 9].

3.2 Buckypaper

A carbon nanotube (CNT) is a thin ribbon of graphene rolled up into a tube. Like carbon nanoribbons, nanotubes can be semiconducting because of the boundary condition imposed on the electron wavefunction by constraining it to a smaller ribbon. However, the boundary conditions on a tube are slightly different than on a ribbon. They are periodic and in some cases they do result in conducting nanotubes. One third of possible chiralities, or ways to roll up a nanoribbon into a nanotube, result in conducting nanotubes. CNT's can consist of rolled single layer graphene (single walled carbon nanotubes or SWCNTs) or multilayer graphene (MWCNT's). Because of the high probability of at least one of the walls being conducting, most MWCNT's are conducting[40].

Buckypaper is a thin film of intersecting CNT's. For this work, I used MWCNT's in order to maximize charge transport.

3.2.1 Fabrication

Carbon nanotubes are fabricated using metal catalyst particles, usually iron, and CVD growth for forests, or tight arrays of vertical tubes grown on a flat substrate[33]. The first CNT growth was done by an arc-discharge method in which opposing graphite rods were brought to a high enough relative voltage to create an arc between them[28]. This method also usually relies on metal catalyst particles.

I fabricated buckypaper by first preparing a solution of 1% sodium dodecyl sulfate (SDS) in deionized water. I added commercially available MWCNT's to this solution and sonicated briefly to suspend them. SDS is a surfactant and it solvates the MWCNT, allowing them to stay suspended in the solution. I then used a vacuum aspirator to draw this solution through a paper filter, and subsequently dissolved the paper in acetone, leaving a film of nanotubes. Figure 3.5 shows a photograph of filter paper with buckypaper on it before dissolution in acetone. The film can be picked up out of solution by a rigid substrate, in my case a prepared amorphous silicon thin film, and then will stick and make electrical contact to the substrate when it dries[14]. An SEM micrograph of a buckypaper film deposited this way is shown in Figure 3.6.

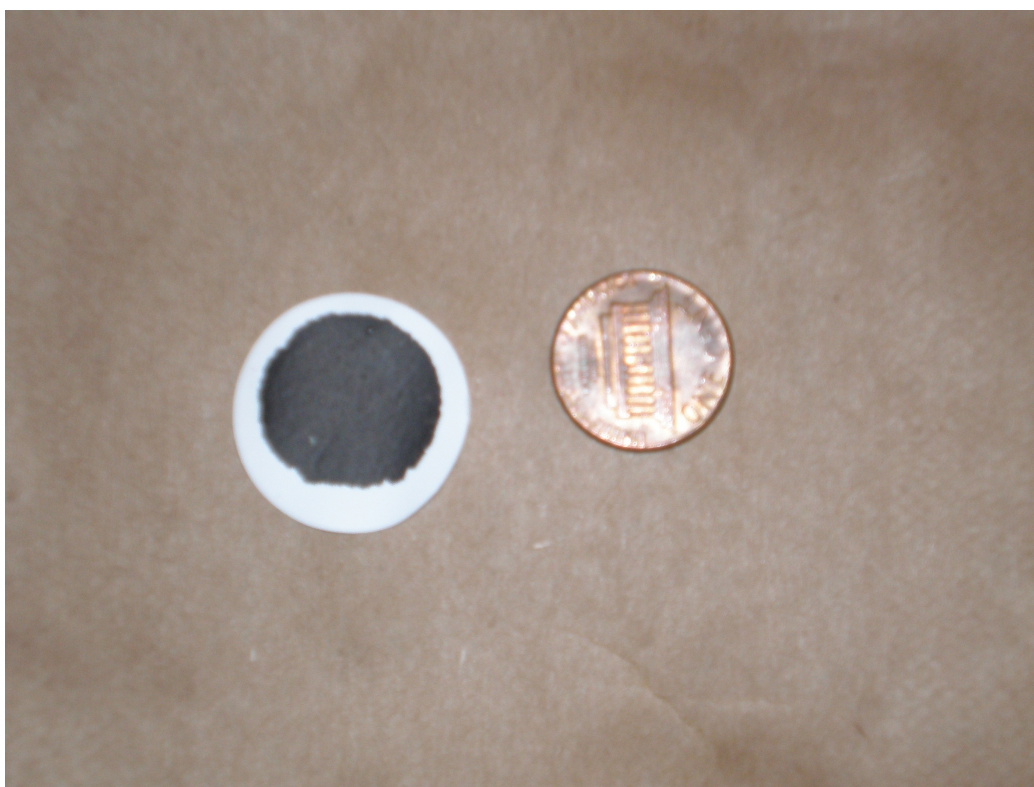


Figure 3.5: Photographic image of buckypaper on filter paper.

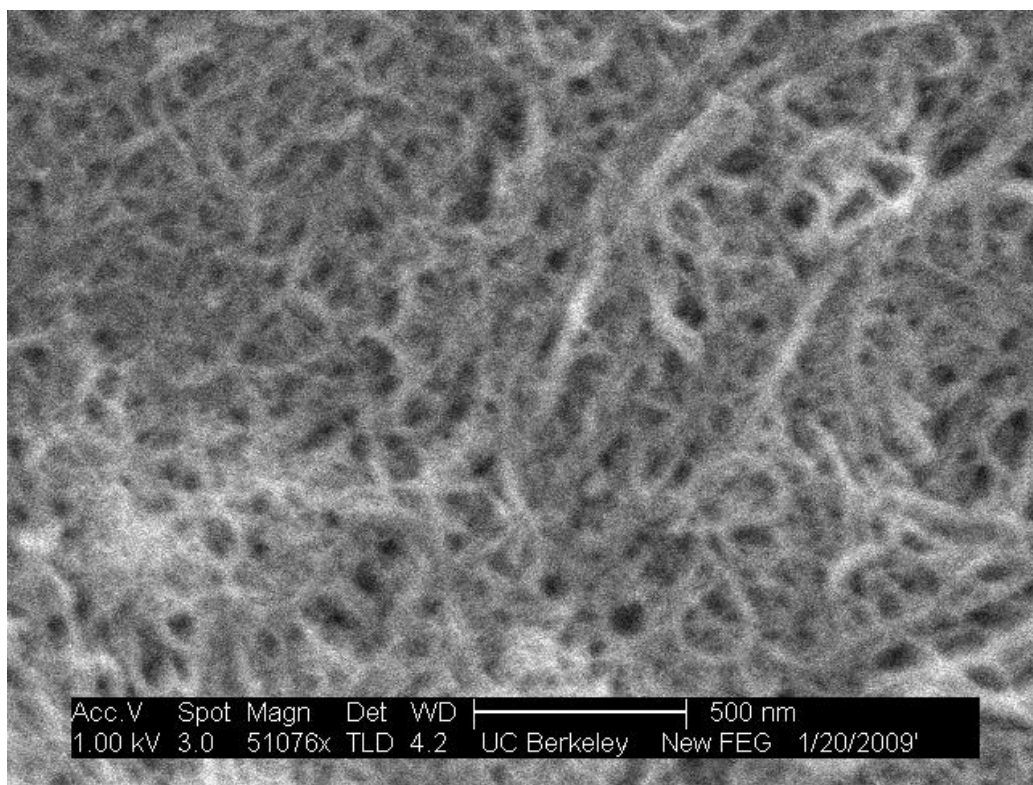


Figure 3.6: Scanning electron micrograph of buckypaper showing individual nanotubes.

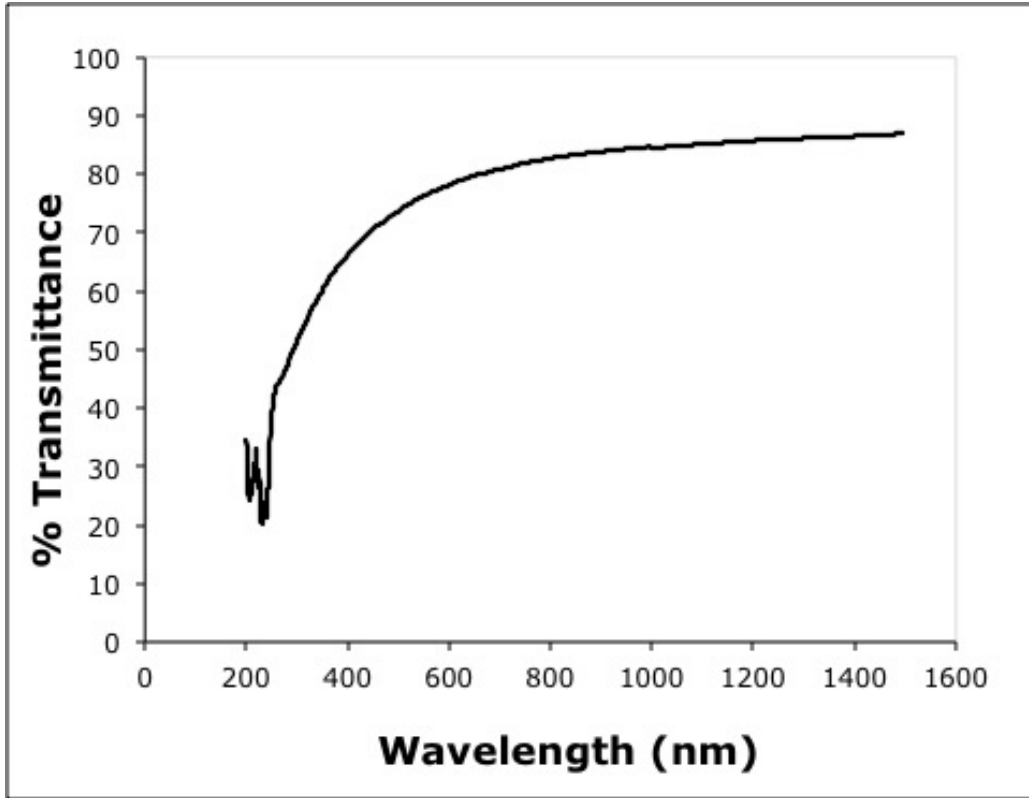


Figure 3.7: Ultraviolet and visible transmission spectrum of buckypaper prepared as described above and deposited on a glass slide.

3.2.2 Properties

Buckypaper is fairly transparent, but less so than graphene. A transmission (1-absorption) spectrum in the visible range is shown in Figure 3.7. My buckypaper films had a sheet resistance of about $1000 \Omega/\square$

The thickness of buckypaper can be modulated by adjusting the concentration of nanotubes in the precursor solution and the volume of precursor solution used. Changing the thickness adjusts the balance between transparency and conductance. A thicker film is more conductive but less transparent. Because a top contact for a solar cell needs to be both transparent and conductive, a material that allows some control over these characteristics allows individual performance optimization for different solar cell materials. My results on buckypaper properties are similar to literature results on graphene-nanotube hybrid films designed for use as transparent electrodes[20].

Chapter 4

Photovoltaics

4.1 Motivation and Material Choice

Several different semiconductors are currently being used to fabricate commercially available photovoltaic modules. They include crystalline silicon, amorphous silicon, gallium arsenide, and cadmium telluride. Many more materials, including lead sulfide, copper zinc tin blends, and copper oxide are being researched for future commercialization. All of these materials offer various advantages and disadvantages. In addition to the advantageous physical properties of amorphous silicon discussed in Chapter 2, the cells described in this thesis offer the advantages of being low-cost and constructed from earth-abundant materials using well-established, scalable production methods.

These solar cells use silicon and carbon as their active material. Figure 4.1 shows the relative abundance of all the elements in the earth's crust on a logarithmic scale[69]. Solar cells made from non-abundant materials will likely see materials costs rise as production grows.

It's especially important to focus on earth abundant, non-toxic materials given the size of the energy industry and the growth rate of the photovoltaics industry. Figure 4.2 shows historical data and future predictions by the European Photovoltaics Industry Association for annual photovoltaics installations globally[5]. The industry continues to grow significantly every year and will quickly outpace supply of rare materials. Moreover, the quick growth rate of demand will discourage careful consideration of end-of-life strategies for toxic materials and use of these materials in solar modules presents the possibility of a significant environmental burden when they are retired several decades in the future.

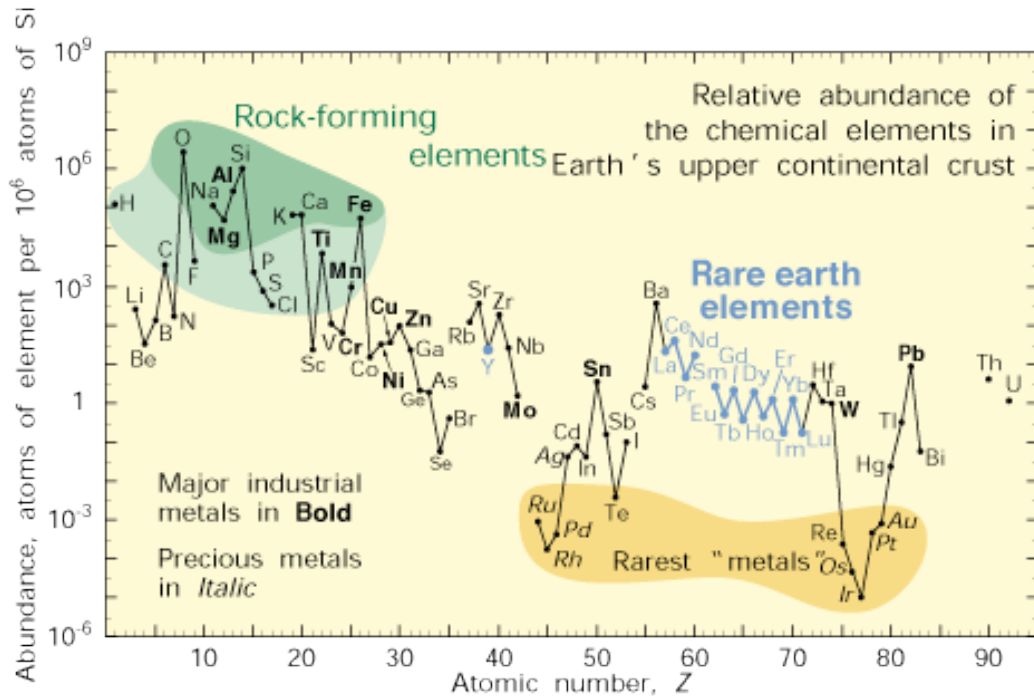


Figure 4.1: Chart showing the most, and least, abundant elements in the earth's crust as a fraction of the abundance of silicon[69].

Figure 4.3 shows the total global energy use and predictions for future use from the Energy Information Administration[2]. The 2008 value of 505 Quadrillion BTU per year converts to 16.9 Terawatts. If we were to consider only electricity use the total today would be much smaller because a large percentage of this 16.9 TW currently comes from the burning of biomass for heat and cooking in impoverished areas. However, as these areas develop, they also electrify. Moreover much of the 16.9 TW is consumed as transportation fuel and land-based vehicles are increasingly powered by electricity as well. Through both of these processes electricity use will grow as a percentage of total energy use and possibly approach total energy use in the coming decades. Any future prediction of the size of the global energy industry, and the opportunity for photovoltaics, must consider the rapidly increasing penetration of electricity as an energy source. Thus considerations of needed abundance of solar cell starting materials should also consider this expansion

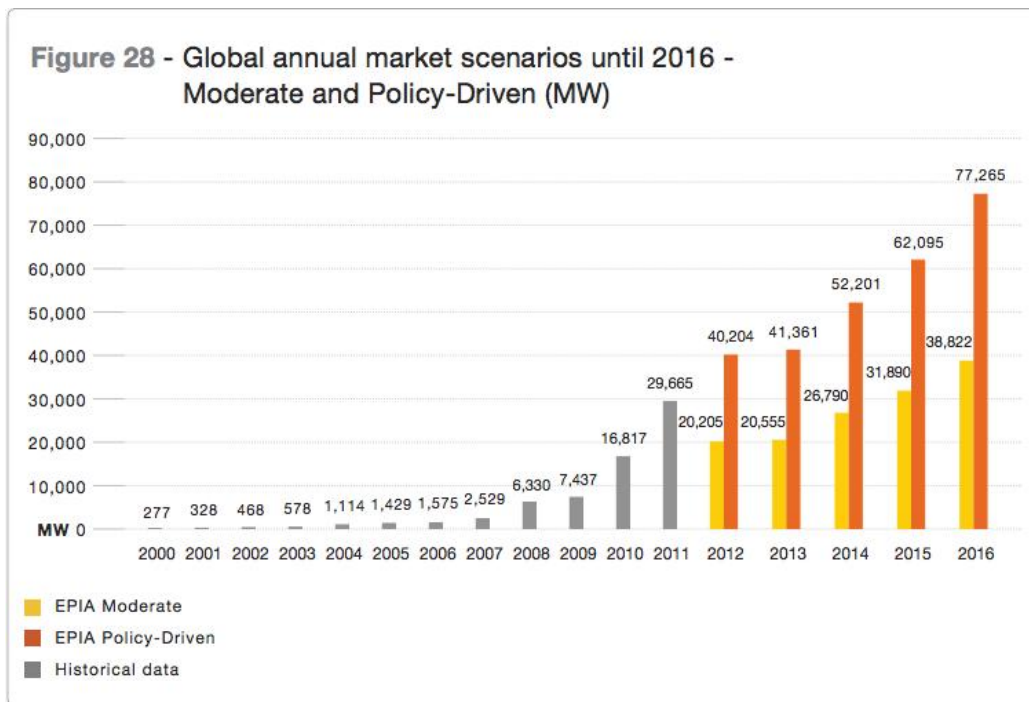


Figure 4.2: Historical data and future predictions by the European Photovoltaics Industry Association for annual photovoltaics installations globally[5].

Figure 1. World energy consumption, 1990-2035
(quadrillion Btu)

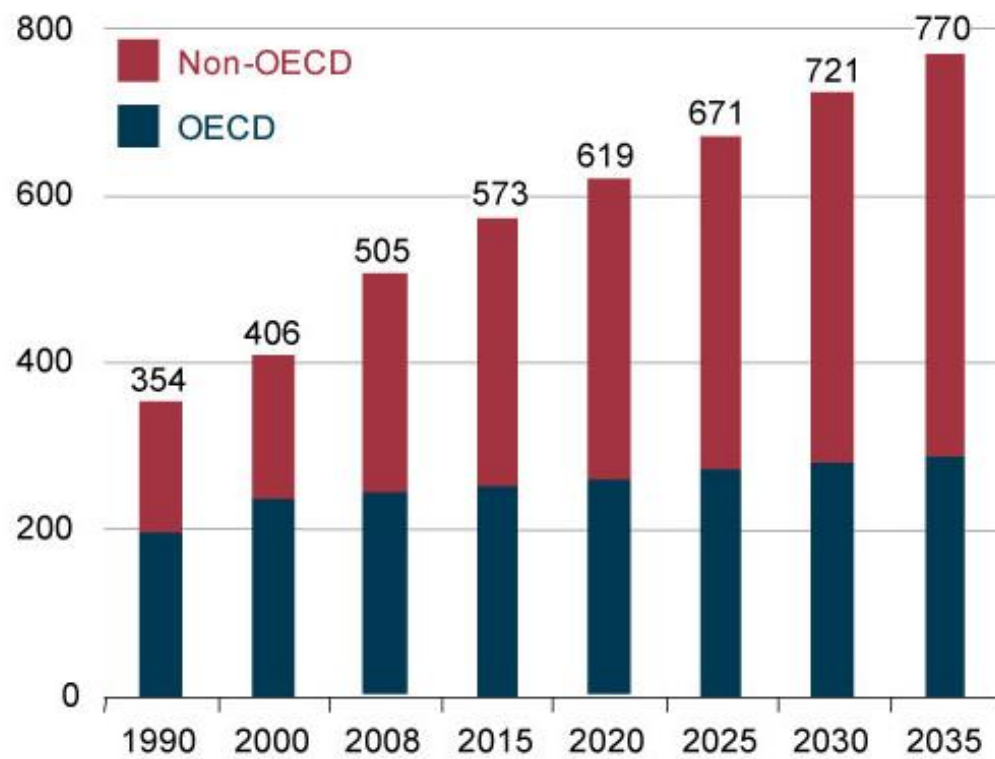


Figure 4.3: Total global energy use using past data and predicted future needs. From the Energy Information Administration[2].

4.2 Economics

Solar cells are expensive, but the price is coming down. Figure 4.4 shows a 50% reduction in installed costs over a 6-year period[57]. The Sunshot Initiative of the Department of Energy has set a goal to further reduce prices to \$1/Watt installed in order to ensure competitive pricing compared to fossil fuel generated electricity[49]. Reducing the cost of the active materials in solar cells is obviously key to reducing their overall costs. However balance of system costs account for up to half of the total installed cost, so the money spent on things like glass and metal frames has to come down too. Since these are commodity materials with relatively stable prices, we need designs that demand less of them. Thin films, including aSi:H, are one opportunity for reduction in balance of system costs because they can be deposited on less brittle substrates that need less protection and can be lighter. In addition to reduced active material costs and balance of system demands, high efficiency is a key attribute of low-cost solar cells to keep land use and installation labor costs, which rise with area installed, down.

In order for solar cells to achieve wide distribution and use, they will have to compete on a cost-per-kilowatt-hour(kWh)-delivered basis with electricity from fossil fuel sources. Because operations and maintenance costs for solar power are minimal, this cost requirement predominantly constrains the installed cost per megawatt. The relationship between a per-MW installed price and a per-kWh delivered price depends on the insolation available, which depends strongly on geography. Figure 4.5 shows at what per-MW installed price photovoltaics compete with current grid market per-kWh delivered prices in different areas of the world[6].

4.3 Physics of Photovoltaics

Photovoltaics are studied and taught in several fields of engineering and physical sciences. As such, there are a few independent frameworks for analyzing solar cell function and performance. Because each one is most useful and effective for understanding certain components of solar cells, I will briefly introduce three different frameworks here. The thermodynamic approach, often taken by physicists, the process-based approach, taken by materials scientists, mechanical engineers, and chemists, and the equivalent circuit approach, taken by electrical engineers.

As a starting point, all solar cells can be modeled as a device composed of an absorbing material that converts light energy into electrochemical energy, and charge-selective contacts that convert electrochemical energy into energy available for elec-

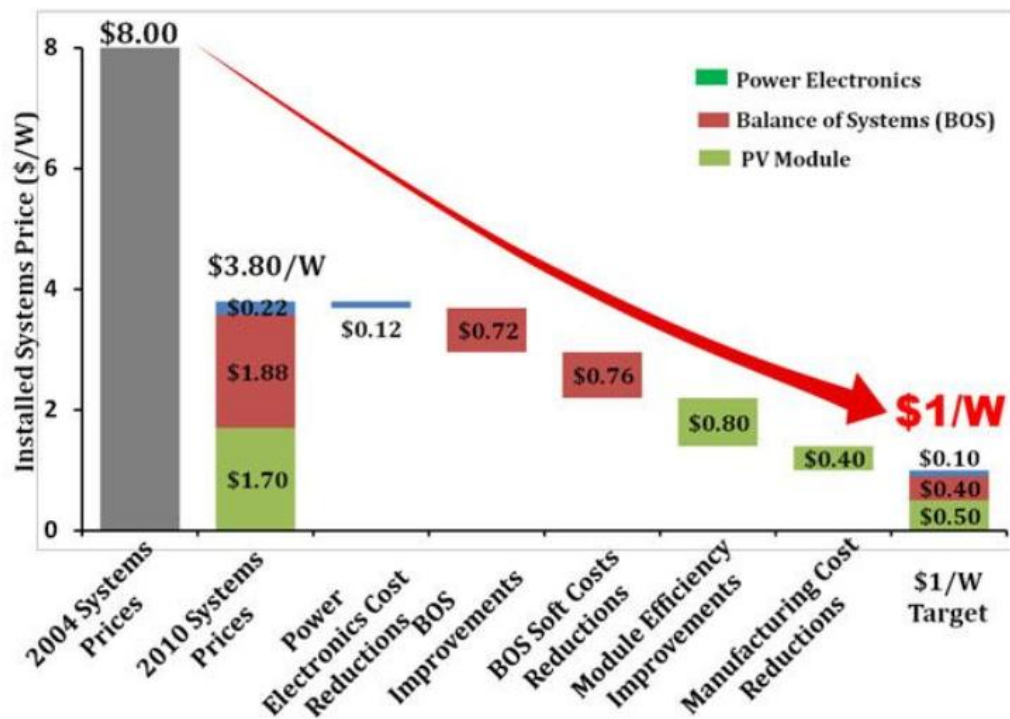


Figure 4.4: Recent reductions in costs for installed photovoltaic systems. This graph shows the cost of a standard system, not the least expensive available system. Costs need to continue to decline to \$ per Watt to compete with fossil fuel derived electricity production[57].

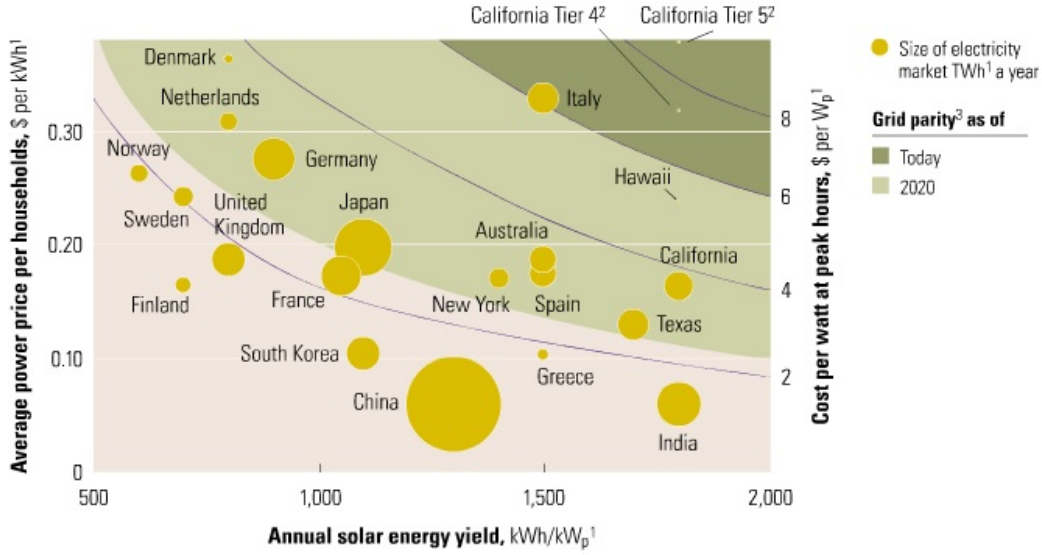


Figure 4.5: Chart showing necessary maximum installed PV costs (\$/MW) to compete with current grid prices for various geographic areas. The price depends on available daily insolation, linked to geography, in addition to current grid prices[6].

trical work in an external load. A basic schematic of this idea is shown in Figure 4.6

4.3.1 Thermodynamic Approach

A solar cell absorbs and emits photons. The energy available for electrical work is the difference between absorbed and emitted energy. The absorbed energy depends only on the incident sunlight, assuming the absorption coefficient is 1. The emitted light energy depends on the populations of excited electrons and holes. When there are more electrons and holes than in the intrinsic semiconductor, more are available for radiative recombination, so more photons are emitted. If none of these excited charges are extracted as electrical current, the populations of excited electrons and holes will rise until the emitted energy current matches the absorbed energy current.

$$\frac{1}{4\pi^3 h^3 c^2} \frac{\varepsilon_G^2 d\hbar\omega}{\exp\left(\frac{\varepsilon_G - (\mu_e + \mu_h)}{kT_0}\right) - 1} = \frac{1}{4\pi^3 h^3 c^2} \frac{\varepsilon_G^2 d\hbar\omega}{\exp\left(\frac{\varepsilon_G}{kT_S}\right) - 1} \quad (4.1)$$

applies for a semiconductor that absorbs and emits only at a single wavelength equal to $\omega = \frac{\varepsilon_G}{\hbar}$ and shows the balance between emitted and absorbed energy for monochromatic light. This follows directly from Planck's law of radiation, with the left-hand side of equation 4.1 being the light emitted by the semiconductor and the

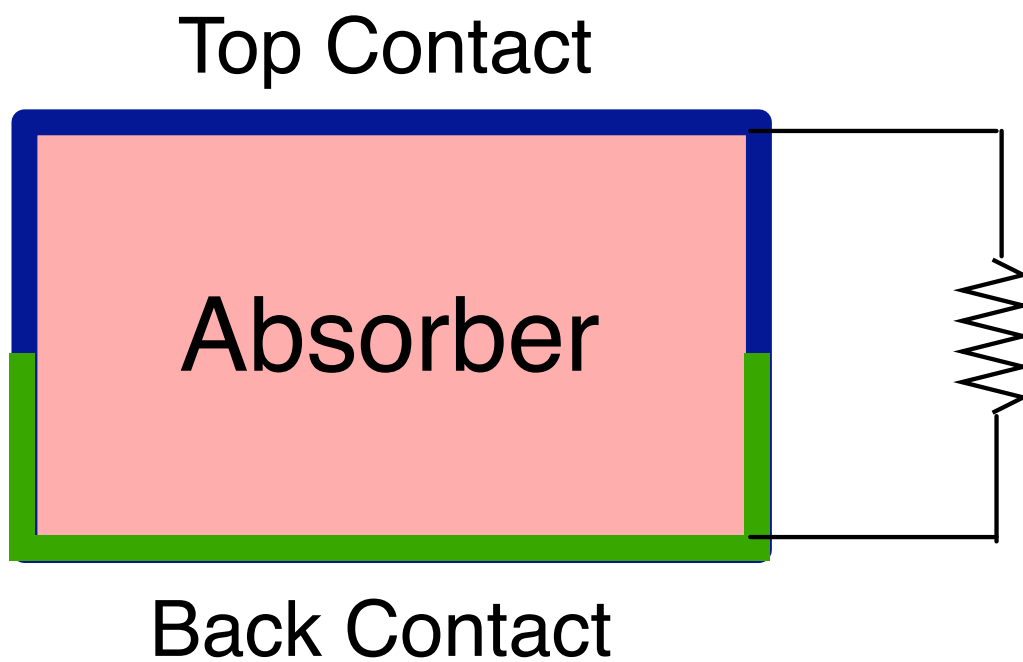


Figure 4.6: The most fundamental model of a solar cell is an absorber, which converts light energy into electrochemical energy, and contacts, which convert electrochemical energy into usable electrical energy (voltage and current).

right hand side being the light emitted by the sun and incident on the cell. μ_e and μ_h are the chemical potentials of electrons and holes, respectively, which are expressions of concentration gradients as potentials. μ_e and μ_h rise as the concentrations of the charge carriers rise with excitation by incident light. Solving equation 4.1 for $\mu_e + \mu_h$ gives us the chemical potential inside a cell in radiative balance with the sun without electric energy being extracted.

$$\mu_e + \mu_h = \varepsilon_G * (1 - \frac{T_a}{T_S}) \quad (4.2)$$

The efficiency of energy conversion, then, is

$$\eta = \frac{\mu_e + \mu_h}{\varepsilon_G} = (1 - \frac{T_a}{T_S}) \quad (4.3)$$

with a indicating absorber and S indicating sun. Which is equivalent to the Carnot efficiency.

$$\eta_{carnot} = 1 - \frac{T_C}{T_H} \quad (4.4)$$

For a cell absorbing sunlight and in thermal equilibrium with the earth,

$$T_C = 300K \quad (4.5)$$

$$T_H = 6000K \quad (4.6)$$

$$\eta_{carnot} = 1 - 300/6000 = 95\% \quad (4.7)$$

However, in order to use the cell to do work, we must extract charges, which means reducing $\mu_e + \mu_h$ by reducing the concentrations of charge carriers. If we extract no charges, we do no work. If we extract all the charge we can, we reduce the chemical potential driving the circuit to zero. We now face an optimization problem wherein we need to extract some charge carriers at some finite potential to maximize the possible work. The energy available to do work is the difference between the absorbed and emitted light currents at some finite $\mu_e + \mu_h$ multiplied by $\mu_e + \mu_h$

$$(\frac{1}{4\pi^3 h^3 c^2} \frac{\varepsilon_G^2 d\hbar\omega}{\exp(\frac{\varepsilon_G - (\mu_e + \mu_h)}{kT_0}) - 1} - \frac{1}{4\pi^3 h^3 c^2} \frac{\varepsilon_G^2 d\hbar\omega}{\exp(\frac{\varepsilon_G}{kT_S}) - 1}) * (\mu_e + \mu_h) \quad (4.8)$$

which can be maximized in $\mu_e + \mu_h$. The maximum energy output is divided by the incoming radiation to give an ideal monochromatic efficiency, η_{mc} . η_{mc} depends on our choice of ε_G , but ranges from 60-90%.

This basic treatment only considers a theoretical semiconductor that absorbs and emits only one frequency of light and optimizes the efficiency at that frequency. However, we can get much more total work out by absorbing a wider range of light energies. Averaged over the solar spectrum, η_{mc} is 86%. That means that a photovoltaic

absorber which could absorb photons of all wavelengths and generate from each photon an electron-hole pair with the same energy as the photon would have a limiting efficiency of 86% [73].

However, it is practically impossible to design an absorber like this. The most common kind of photovoltaic absorber is a single band gap semiconductor. It absorbs only photons with energies above its band gap, and generates from each one an electron-hole pair with the energy of its band gap, no more, regardless of the energy of the incoming photon. This single-band gap efficiency limit clearly depends on the band gap of the cell. Because the cell only absorbs photons with energies above ε_G , a lower band gap allows more absorption. However, when a single photon delivers energy beyond the band gap, the generated electron and hole quickly lose the extra energy to collisions within the material. These two processes impose an upper limit for the photon conversion efficiency for a solar cell with a single band-gap absorber of about 38%, known as the Shockley-Queissar limit[56].

Achievement even of this 38% efficiency requires several other conditions to be met that are essentially impossible for a real solar cell. First, the cell must be accepting sunlight from all angles. if it is not, the ideal efficiency falls as

$$\eta = \eta_{ideal} * (1 - \frac{\Omega_{emit}}{\Omega_{abs}} * \frac{T_A^4}{T_S^4}) \quad (4.9)$$

where Ω_{emit} is the solid angle through which the cell emits radiation, and Ω_{abs} is the solid angle from which sunlight is incident. For unconcentrated light, Ω_{emit} is much larger than Ω_{abs} . T_A is necessarily much smaller than T_S . Because the sun is the major source of energy for all earth-based devices, it would be thermodynamically impossible for T_A to increase to T_S if Ω_{abs} were not smaller than Ω_{emit} , and impossible for T_A to rise above T_S . This constraint keeps $\frac{\Omega_{emit}}{\Omega_{abs}} * \frac{T_A^4}{T_S^4}$ under 1 and η positive.

Many strategies involving mirrors and lenses have been installed to concentrate light on solar cells and increase the effective solid angle of sunlight they intercept. However, none of these strategies are ideal and they involve increasingly precise engineering and expensive, high quality optics as they approach full concentration.

Second the cell must not reflect any sunlight. all photons must be absorbed. it must also not transmit any photons, so it must be thick enough to absorb all incident light. Solar cell manufacturers invest in anti-reflection coatings, but it is difficult to make a coating that minimizes reflection of light incoming at all angles. Since diffuse light is a large component of insolation due to scattering by particles in the atmosphere and multiple reflections off the ground and any nearby buildings or structures, it is important to collect light from all angles and broad-angle anti-reflection coatings are an active area of research [27, 67, 32].

4.3.2 Processes

Any solar cell architecture must provide for 3 essential photovoltaic processes to occur. These are:

- Light Absorption and Charge Pair Formation
- Electron-Hole Separation
- Charge Extraction

In a standard p-n junction cell, the entire cell absorbs light. For each photon absorbed, an electron and a hole are created. Then electrons move to the n-type material and holes to the p-type due to the electrochemical potential field between the two materials in contact with each other. The charges are separated from each other at creation and remain separated because they are attracted to opposite ends of the device. Ohmic contacts extract the charges from each material.

In a Schottky barrier solar cell, a metal-semiconductor junction separates the charges. All of the absorption happens on the same side of the separation interface, in the semiconductor. A metal contact is needed for extraction from the semiconductor, but from the metal charges are easily extracted as they are already in a metallic material. The cells described in this thesis are Schottky barrier cells and an image identifying where each of these processes take place is shown in Figure 4.7.

In an excitonic cell, the processes occur differently, but the same processes occur. Absorption and electron-hole pair creation may occur in one or both of two materials. Usually one material is considered n-type and one is considered p-type. When an electron-hole pair is created, the Bohr radius of the pair is smaller than the screening length of the material and the two charged particles are bound together in a particle known as an exciton. They diffuse together to an interface where they are separated by the different electrochemical potentials in the two materials. In this device some voltage is sacrificed to provide the necessary potential to split the exciton. Most organic solar cells are excitonic, and the delineation between an excitonic and non-excitonic cell depends entirely on the ratio of the Bohr radius to the screening length in the absorber material[45].

4.3.3 Equivalent Circuit

A circuit diagram of a solar cell is shown in Figure 4.8.

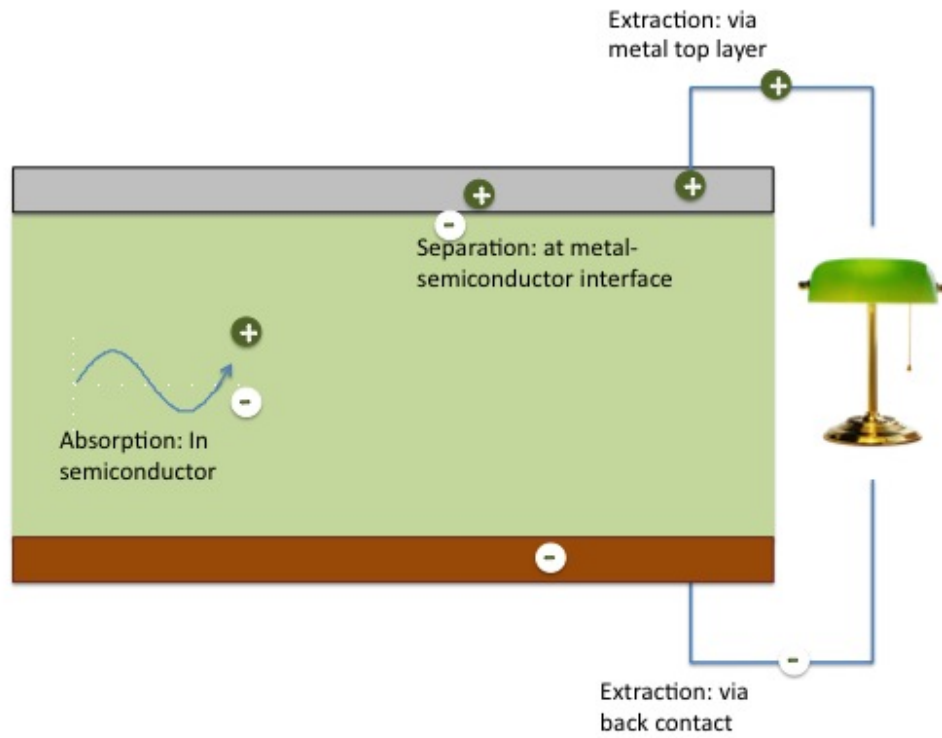


Figure 4.7: Diagram showing where three fundamental photovoltaic processes occur in a Schottky barrier solar cell.

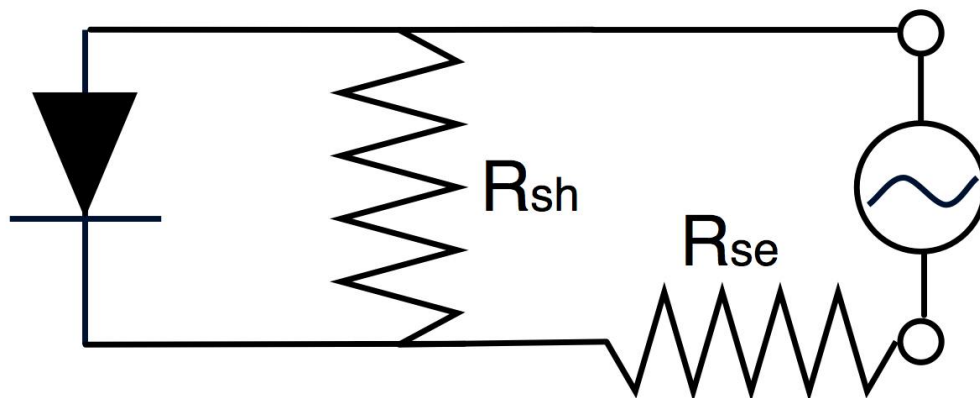


Figure 4.8: Equivalent circuit diagram for a solar cell.

Two resistances in the circuit are key to the performance of the cell. The shunt resistance, in parallel with the diode, provides a path for generated high energy charge carriers to travel through the cell rather than through the external circuit. This is an energy loss mechanism-the charge carriers' energy thermalizes within the cell rather than being delivered to the external load-and thus a lower shunt resistance sacrifices efficiency in the solar cell. High quality cells maximize shunt resistance. Practical shunt mechanisms include short paths through the cell, imperfect dielectrics separating the two contact metals, or unoptimized wiring that allows electrons to move from the front to the back contact within the solar cell.

The series resistance, conversely, is minimized in a well-engineered solar cell. Series resistance is any resistance electrons or holes must overcome to get from the charge separation interface into the external load. It includes contact resistance, resistance of the contact material, especially top contacts which must sacrifice some conductivity for transparency, and resistance in the active material itself. aSi:H, for example, has a very low conductivity and resistance encountered by majority carriers in their journey out of the absorber layer after separation at a p-n interface or Schottky junction can be included in R_S for analysis.

With near-ideal series and shunt resistances, this circuit shows a similar relationship between current and voltage as a diode. However, an extra term, j_{SC} is subtracted from a standard diode curve to account for the carriers generated by incoming light.

$$j = -j_{SC} + \exp \frac{eV}{kT} \quad (4.10)$$

When $V = 0$, j_{SC} is the current that flows, the short-circuit current. When j is zero, the open circuit voltage, V_{OC} is $\frac{kT}{e} * \ln(j_{SC})$. e is the elementary charge. The fill factor is the ratio of the maximum power to the product of V_{OC} and j_{SC}

$$FF = \frac{j_{mpp} * V_{mpp}}{j_{SC} * V_{OC}} = \frac{I * \eta}{j_{SC} * V_{OC}} \quad (4.11)$$

so that

$$\eta = \frac{FF * j_{SC} * V_{OC}}{I} \quad (4.12)$$

where I is the incoming radiation energy intensity in milliwatts per square centimeter and j is in milliamps per square centimeter. In the sample solar cell current voltage curve shown in Figure 4.9, the fill factor is the ratio of the blue rectangle, the largest rectangle that can be drawn inside the curve, to the pink rectangle formed by drawing a vertical line through V_{OC} and a horizontal one through j_{SC} .

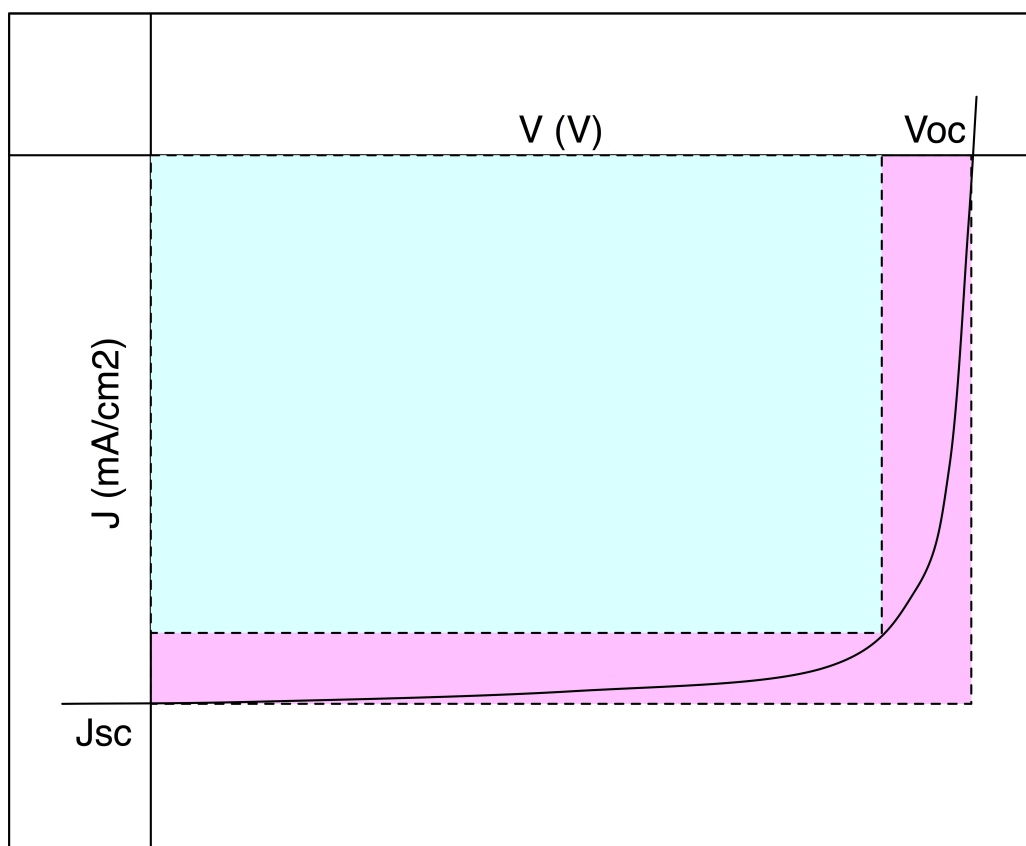


Figure 4.9: Current-voltage characteristics of a solar cell.

Table 4.1: Solar cell properties

V_{OC}	Open circuit voltage
j_{SC}	Short circuit current
FF	Fill factor
η	efficiency $\eta = \frac{V_{OC} * j_{SC}}{I}$

4.4 Amorphous Silicon-Carbon Nanostructure Solar Cells

For this thesis, I made photovoltaic cells using a Schottky barrier structure between hydrogenated amorphous silicon and either graphene or buckypaper. This work was previously published with Matthias Loster, Will Regan, and Alex Zettl in the journal Solid State Communications in December, 2009 and is reprinted here with the permission of the original publisher[52]. Similar cells have been made using crystalline silicon [34, 29, 15] and experiments on these cells have shown that, in addition to holding promise as a transparent top contact material[37, 72, 68], graphene is a promising active junction material. Either graphene or buckypaper can be doped [16, 38, 12, 11, 39] for better performance. Experiments from the literature also include photovoltaic devices made only from carbon nanotubes and metal contacts of different fermi levels [8].

4.4.1 Fabrication

Graphene and buckypaper were fabricated as explained in the previous chapter. Hydrogenated amorphous silicon (aSi:H) was deposited using an Oxford plasma-enhanced chemical vapor deposition (PECVD) chamber with silane and argon flow at 350°C.

I deposited aSi:H on patterned indium tin oxide (ITO) on glass substrates purchased from Thin Film Devices. ITO is used as a back contact because its Fermi level is appropriate for an ohmic contact with aSi:H. It is not important that this layer be transparent, and the ITO could easily be replaced by a less expensive metal as shown in Chapter 6.

On top of the aSi:H, I deposited an insulating layer. On some devices, this was a 1- μm thick SiO_2 film deposited in the same PECVD chamber as the aSi:H active layer. In some devices, it was a much thinner (50nm) thick layer of alumina (Al_2O_3) deposited via electron beam evaporation. The purpose of this layer was to separate

Table 4.2: Photolithography parameters

Resist	I-line
Spincoat speed	3000 rpm
Spincoat time	1 minute
Soft bake	2 minutes at 110 °C
Exposure	UV lamp for 2.5 minutes
Post-exposure bake	2 minutes at 110 °C
Development	1-minute, stop in water
Hard bake	30 minutes at 120°C

the contacts to the carbon nanostructure from the aSi:H and prevent shunting of the cell. I etched a window either 5cm^2 or $500\mu\text{m}^2$ in the insulating layer which became the active area of the cell. The etching process was done with photolithography using laser-printed transparency masks, I-line resist with a hard bake, and hydrofluoric acid (HF) to remove the SiO_2 or Al_2O_3 . Table 4.2 details the photolithography process parameters.

Subsequent to the window etching I deposited either buckypaper or graphene as described in the previous chapter. Graphene is transferred from the copper catalyst foil used for deposition to a substrate using poly methyl methacrylate (PMMA) as a support. We spincoat PMMA on top of the graphene, then etch the copper using a 10% by mass solution of iron chloride (FeCl_3) in water. The PMMA-supported graphene can be picked up from the top of a volume of water by any substrate[37]. The carbon nanostructure completely covered the window and some area around it on all sides. I used silver paint to make a top contact to the carbon nanostructure over the insulating layer (not over the window), and a back contact to the ITO. A schematic of the final device is shown in Figure 4.10 and optical photos of the fabricated devices are shown in Figure 4.11

Crystalline silicon cells were made with a similar process using commercially available doped silicon wafers with several hundred nm of SiO_2 grown by the manufacturer. These wafers were used in place of aSi:H- SiO_2 films on ITO and the back contact was made to a cleaved edge of the wafer about 1-2cm from the device area.

4.4.2 Photovoltaic Model

This structure performs as a Schottky barrier solar cell. Photons are absorbed in the aSi:H layer and converted to electron-hole pairs. When charge carriers approach the aSi:H-carbon nanostructure interface, holes preferentially enter the graphene or

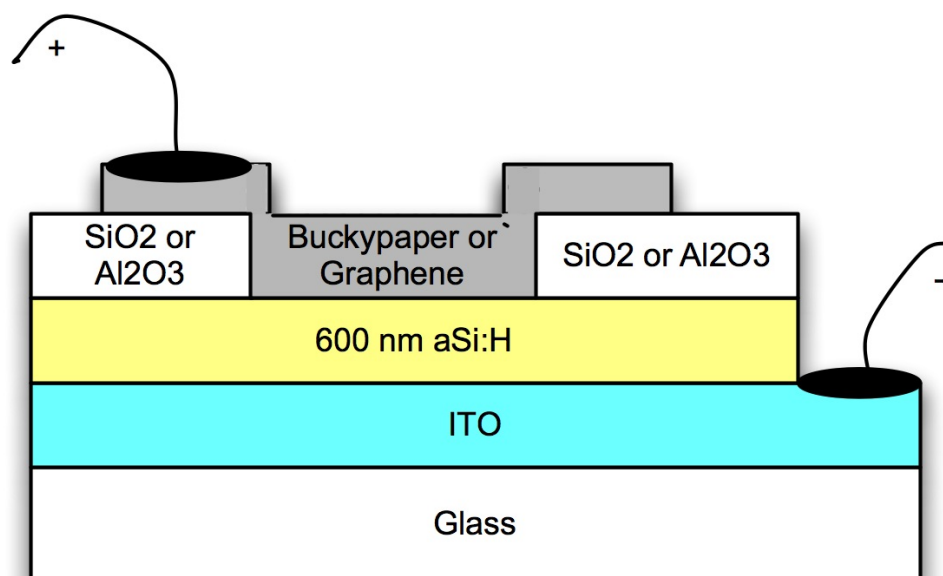


Figure 4.10: A schematic of device structure. aSi:H is PECVD deposited on patterned ITO substrates. Either SiO₂ or Al₂O₃ is deposited on top, and a window is patterned and etched. A carbon film is deposited over the window.

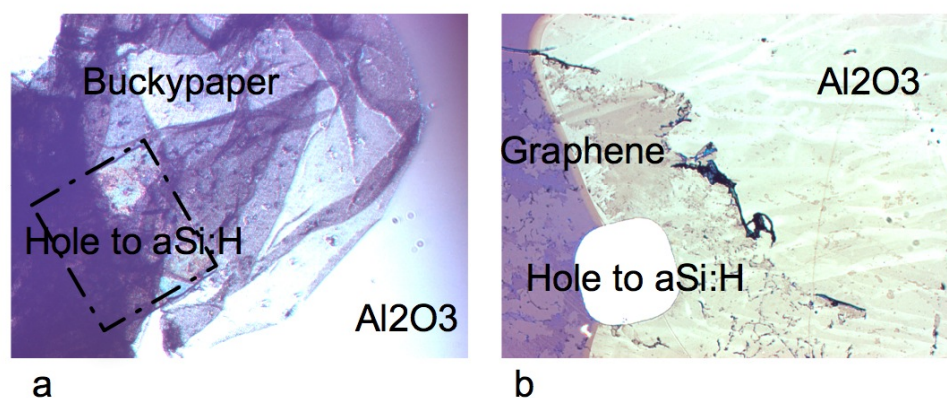


Figure 4.11: Optical micrographs of devices. Both are taken at the same magnification. Side length of the square window is 500 μm .

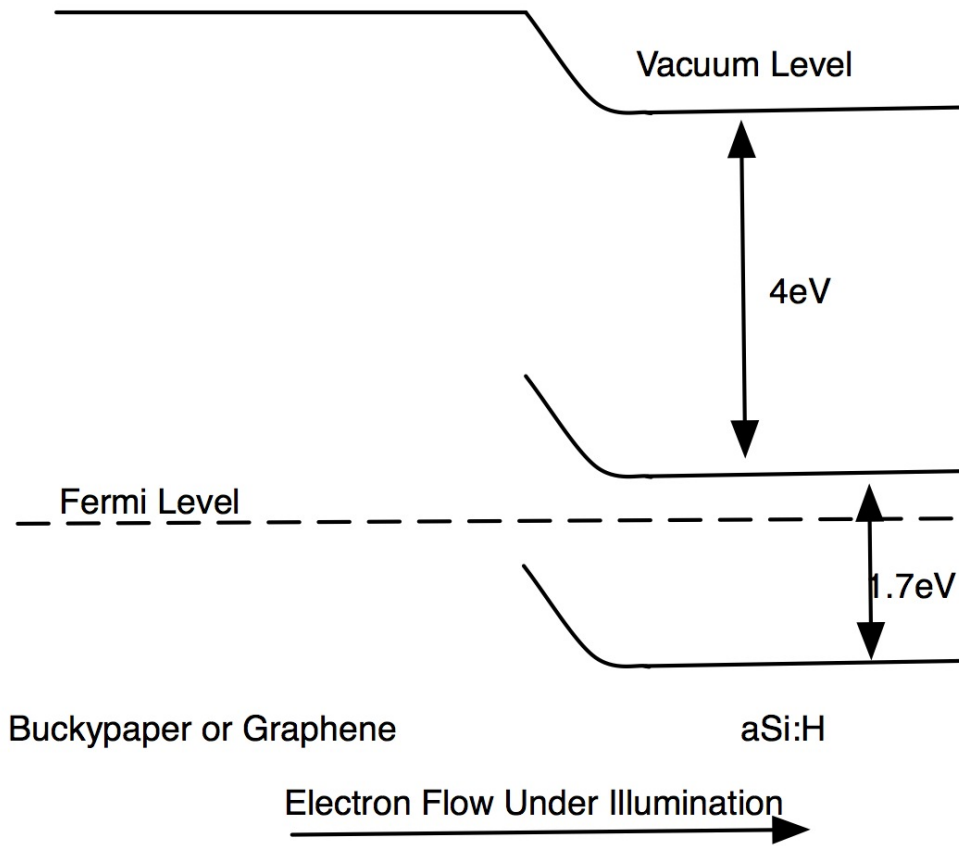


Figure 4.12: Approximate band diagram for a Schottky barrier aSi:H-carbon nanostructure solar cell.

buckypaper due to the alignment of the fermi level of the carbon nanostructure with the valence and conduction bands of the semiconductor. Figure 4.12 shows the band alignment of an aSi:H-carbon nanostructure junction based on these experiments.

4.4.3 Performance

I tested all devices in this thesis using a Newport xenon lamp with a filter. The illumination has an intensity, measured by a calibrated silicon diode, of 135 mW/cm². Figure 4.13 shows a schematic of the device testing setup.

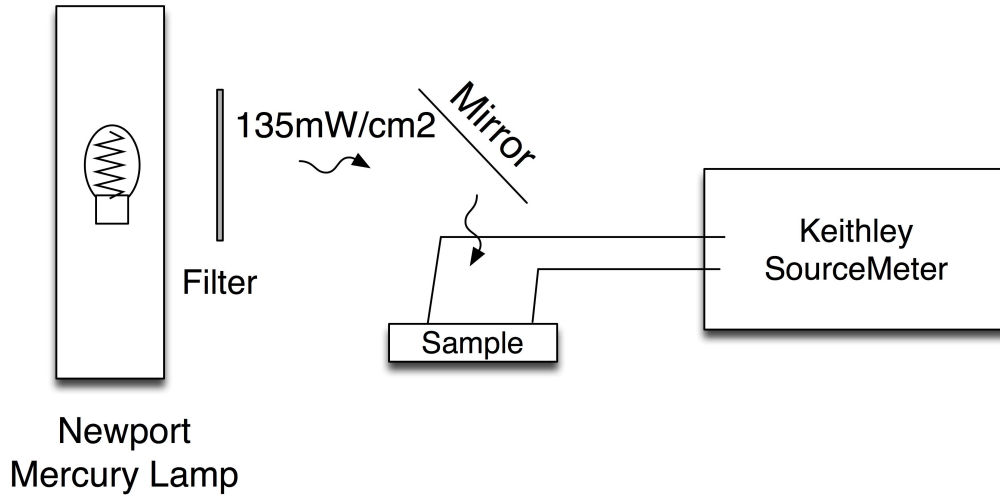


Figure 4.13: Solar simulator setup used to measure solar cells in this thesis.

To determine the contribution of the carbon nanostructure to the series resistance, I tested the conductance of both the graphene and the buckypaper, shown in Figure 4.14. Results show that conductances are about as expected and high enough that the carbon nanostructures will not present significant series resistance in the cell when compared to the aSi:H absorber.

In order to approximate the relative fermi level of the graphene and understand the nature of the junction, I first made devices with both p-type and n-type silicon and tested their relative performance, shown in Figure 4.15. The results indicate that the graphene behaves as if it were p-type, with almost no open circuit voltage in a junction with p-type silicon, but with decent performance in a junction with n-type silicon.

Next, I fabricated aSi:H-based cells and measured their conductivity in the dark. The results are shown in Figure 4.16. While the buckypaper cell has a low dark current, due to the high resistance of the aSi:H and the diode junction, the graphene cell has a much higher conductance, which indicates possible shunting either from the silver paint contact to the aSi:H or from the graphene to the ITO back contact, allowing charge carriers to travel through the cell without crossing the aSi:H-carbon nanostructure interface.

I took dark current measurements inside an electrically shielded box, approximately 25cm x 35cm x 45cm high lined with black paper and closed on all sides to prevent room light from entering.

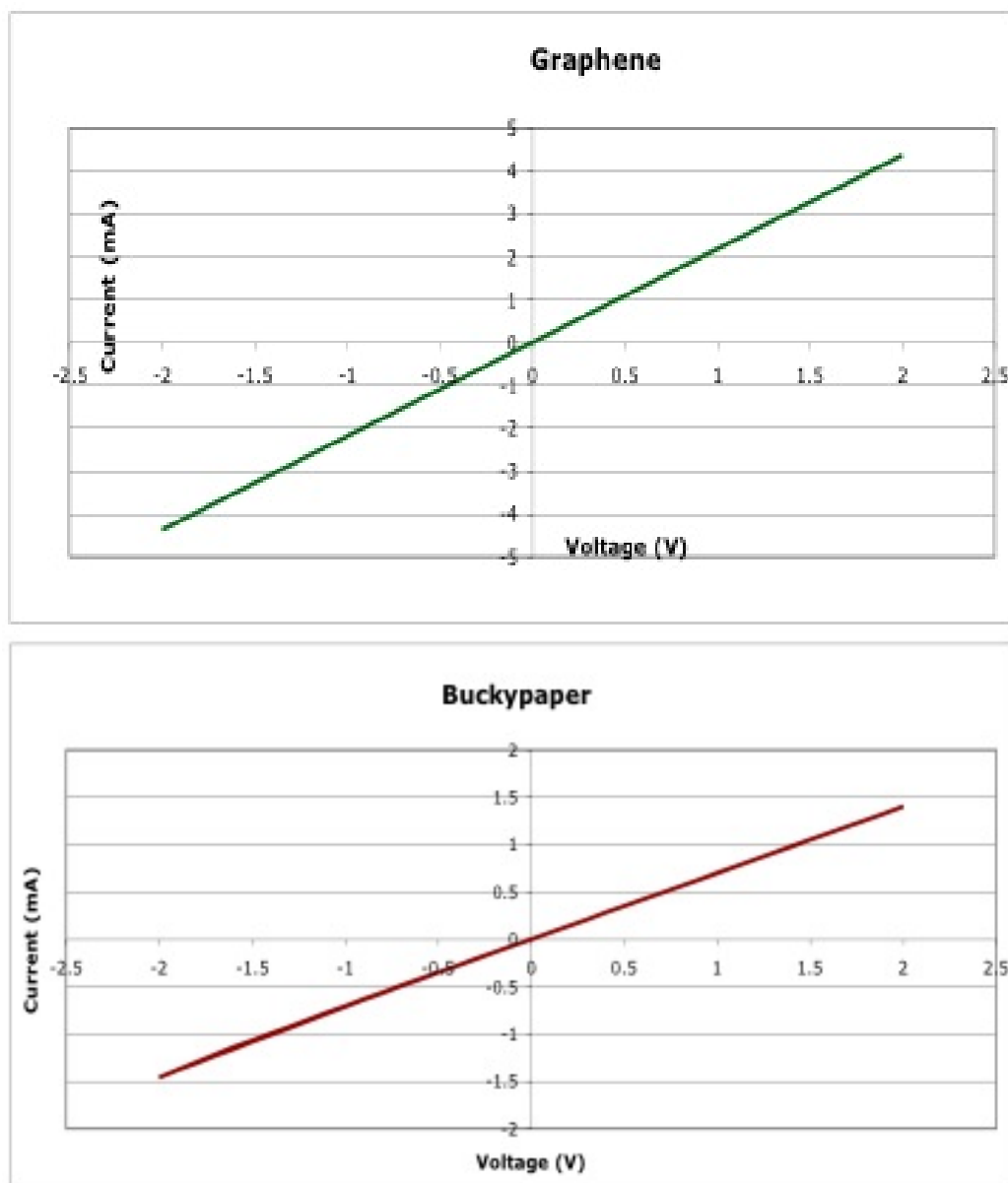


Figure 4.14: Conductance of plain graphene (above) and buckypaper (below) films.

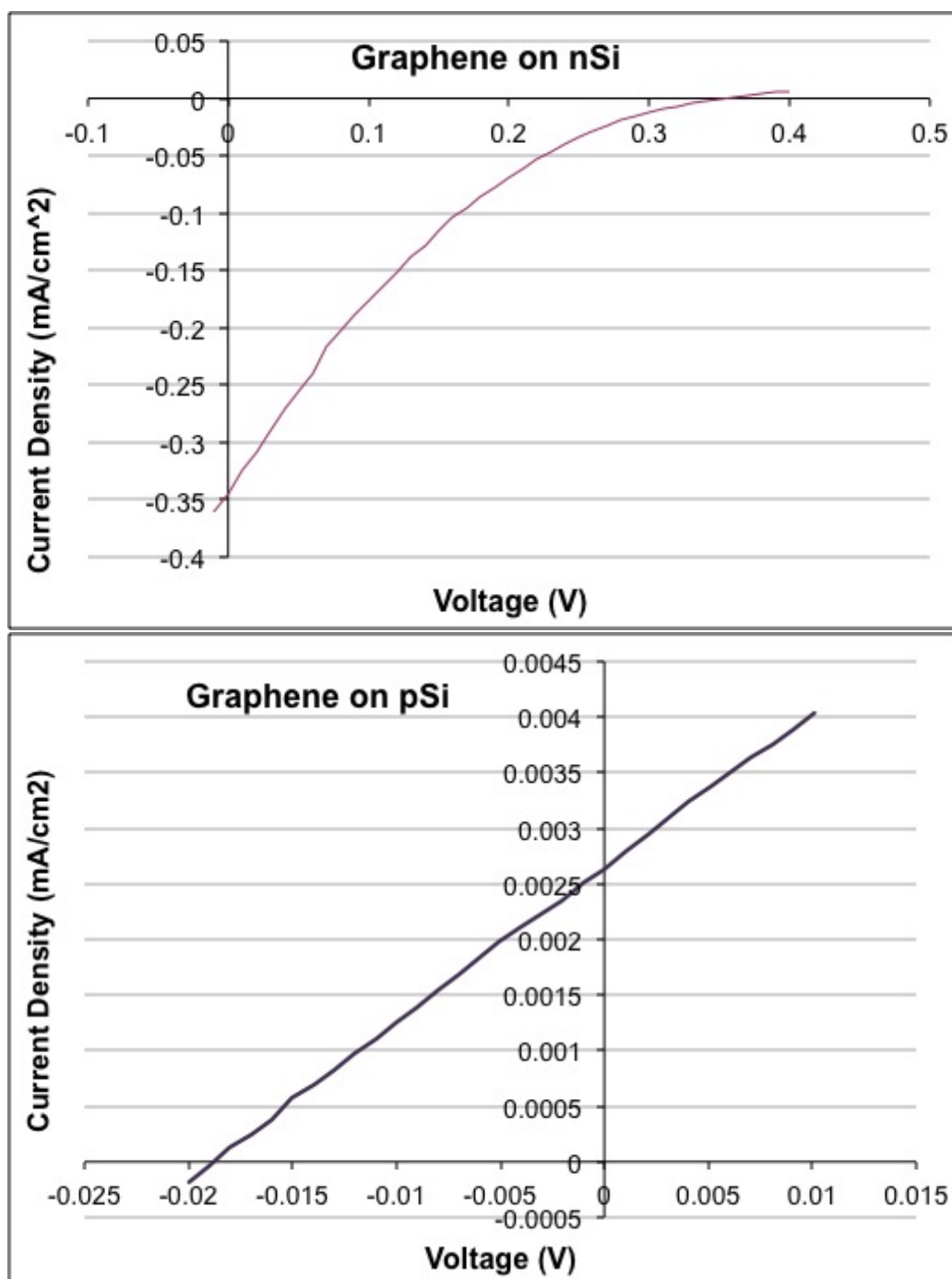


Figure 4.15: Current-voltage curves for initial tests of crystalline silicon-graphene junctions. Top is n-type silicon, which makes a working junction. Bottom is p-type, which does not.

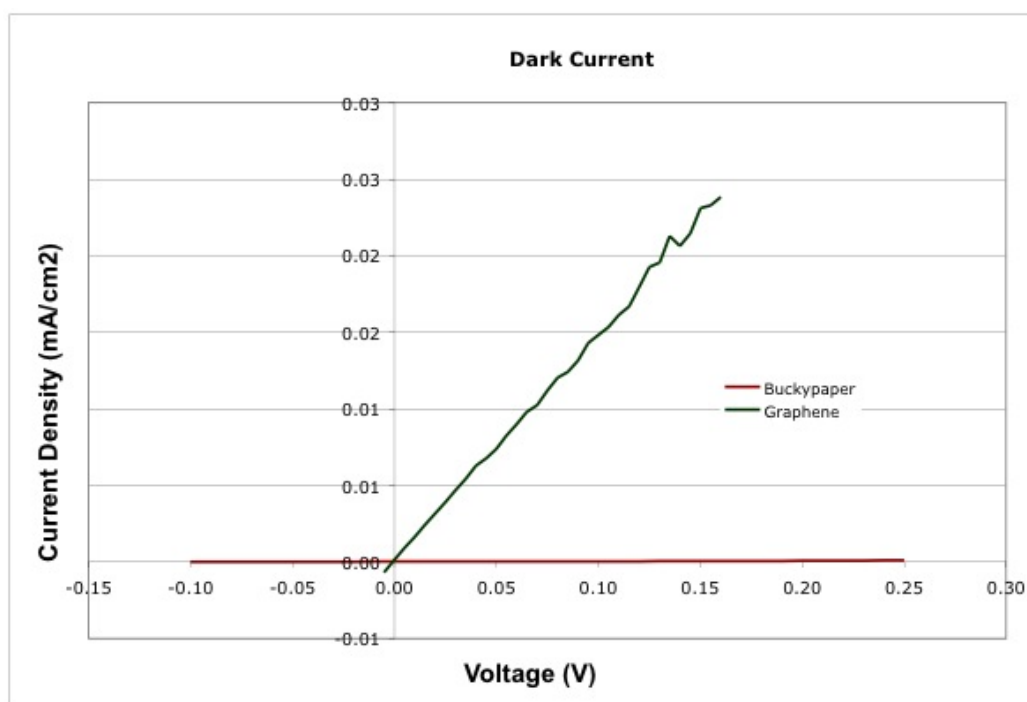


Figure 4.16: Current-Voltage curves for both buckypaper and graphene cells in the dark.

Table 4.3: Table of respective properties of graphene- and buckypaper-aSi:H solar cells

Cell Type	η (%)	J_{SC} (mA/cm ²)	V_{OC} (V)	Fill Factor
Buckypaper	0.00992	0.216	.390	0.16
Graphene	0.00167	0.0748	0.15	0.2

Figure 4.17 shows the current-voltage characteristics of a typical graphene and buckypaper on aSi:H solar cells. The open-circuit voltage (V_{OC}) is encouragingly high in both cells, 390mV for the buckypaper cell and 150mV for the graphene cell, and no degradation is seen when cells are stored in air at room temperature for several weeks. This is an indication that the band alignment between undoped aSi:H and carbon nanostructures is appropriate for solar cell applications. As-deposited aSi:H is generally lightly n-type due to oxygen impurities. In our testing apparatus, the buckypaper or graphene acts as an electron donor and hole transporter, while the aSi:H acts as an electron acceptor. Because MWCNTs and graphene both act as metals, we can analyze the system as a Schottky barrier as shown in figure 4.12. We have attempted to approximately characterize the fermi level of the graphene by constructing cells using devices built on silicon wafers with the same geometry as in figure 4.10. The open circuit voltage in a graphene-nSi device is 350mV, while V_{OC} for a graphene-pSi device is -20mV. Based on the fermi level and band gap of crystalline silicon, we can estimate that the graphene fermi level lies between 4 and 4.5 eV.

The illuminated j-V curves generally have fill factors smaller than 0.2. Fill factors this low are rarely seen in photovoltaics literature, and could indicate interesting interface physics. At this point, we do not fully understand the reason for the low fill factors, but we hypothesize that low energy trap states at the interface may be drastically reducing currents at voltages close to V_{OC} .

One clue to understanding the low fill factors may be the j-V behavior of the cells on a larger voltage range. The current through a buckypaper cell between $V = -5V$ to $+5V$ is shown in Figure 4.18. The curve does not show rectification. i. e. it does not have the exponential shape expected based on equation 4.10. It's also hard to see the shape seen in Figures 4.17 and 4.15. The relationship is approximately linear. This indicates that significant shunting is occurring in both cells. Importantly, it does not show evidence of a two-diode configuration that would indicate a non-ohmic back contact. The anomalous behavior seen in Figures 4.17 and 4.15 is clearly limited to voltages between 0V and V_{OC} . One way to think about this phenomenon is that

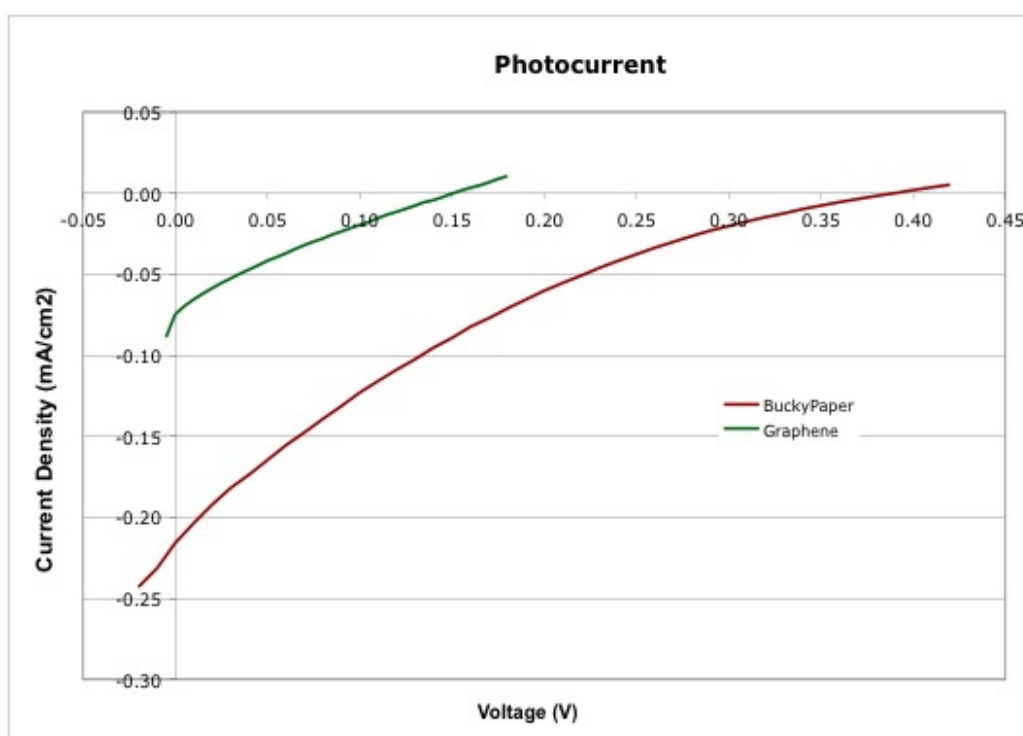


Figure 4.17: Current-Voltage curves for both buckypaper and graphene cells illuminated by $135\text{mW}/\text{cm}^2$

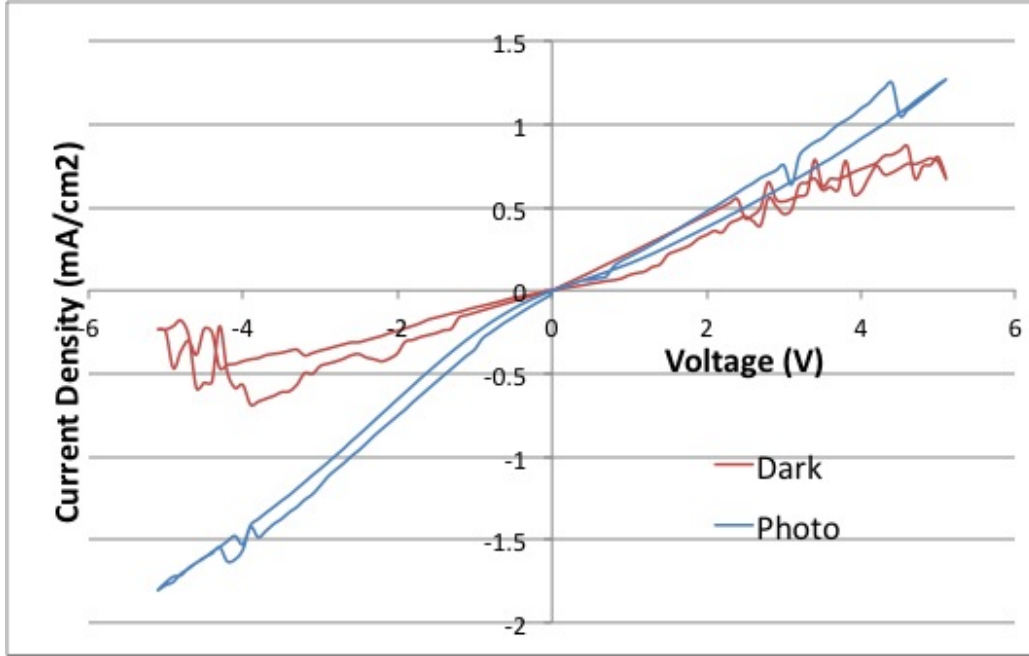


Figure 4.18: Current-Voltage curve for a buckypaper cell over a large voltage range.

any charges not being extracted, or any current below the ideal diode curve shown in Figure 4.9 is likely a consequence of nonradiative recombination. Nonradiative recombination refers to any combination of electrons and holes that does not emit a photon, often a consequence of a mid-gap state or other energetically isolated trap state. Usually, the rate of nonradiative recombination is higher when the voltage is higher because the higher voltage is associated with a higher concentration of electrons and holes available for recombination. In a normal cell, as the voltage drops this recombination also drops so the magnitude of the current grows more than linearly with $|V - V_{OC}|$. If nonradiative recombination actually grew as the voltage fell from V_{OC} , we would expect an effect like the one we see here. This could be a consequence of the available trap states, especially those at the surface, depending on the voltage. Because the density of states in graphene is so small due to it consisting of a single atomic layer, it is possible for significant changes in available states to occur as an electric field is applied.

In addition to poor fill factors, the cells also show low current densities. The resistivities according to Figure 4.16 are on the order of hundreds of Ω/\square for graphene and $k\Omega/\square$ for buckypaper. These layers do not add series resistances higher than $k\Omega$ to the cell, and cannot explain the low currents. Both the low current and the low fill factor may be a result of geometrical issues associated with the buckypaper and

graphene deposition methods. The carbon films are picked up out of a water bath by the substrate. It is impossible to ensure that they are flat on a microscopic scale, and the quality of the electrical contact between the films and the silicon is unknown. However, changes in geometry such as varying the window size and oxide layer did not have a significant effect on the efficiency of the cells.

Transmittance of the films is good. Graphene grown with this method has a transmittance above 80%[4], and the buckypaper has transmittance between 60-85% in the 400nm-1000nm wavelength range (spectrum shown in Figure 3.7. Optical micrographs of both devices are shown in figure 4.11, which give a sense of how much light is able to penetrate the films. The transmittance measurement was done on very flat buckypaper, but it is difficult to deposit very flat films on our cells, so they are not as transparent.

4.4.4 Future Direction

We have produced working, air-stable solar cells with active layers made entirely from carbon, silicon, and hydrogen that do not require expensive transparent top conducting layers. This is an important step in the quest to directly convert sunlight into usable energy using abundant materials and scalable processes. Geometrical and interface characteristics currently limit the capability of these cells to supply large currents, but high open circuit voltages indicate that the basic cell design has promise and may be a simple, practical structure for solar cells in the future.

The performance is similar for two different types of carbon nanostructures, graphene and buckypaper, and the basic structure could be adapted to other carbon nanostructures as well as other semiconductors.

This basic structure has the distinct advantages of avoiding toxic, expensive dopants and relying on earth-abundant materials. Different geometries could improve light management and absorption, or improve the quality of the electrical contact between the silicon and carbon. In an improved geometry, this amorphous silicon-nanostructured carbon interface could be the basis for highly efficient solar cells made with an inexpensive, scalable production process.

One way forward in this experiment is to investigate the behavior of a single carbon nanotube in a junction with aSi:H. I successfully deposited 30nm of aSi:H on a single carbon nanotube, shown in Figure 4.19. The aSi:H appears to conformally coat the nanotube, but pinholes through such a thin film would make contacting the device a challenge.

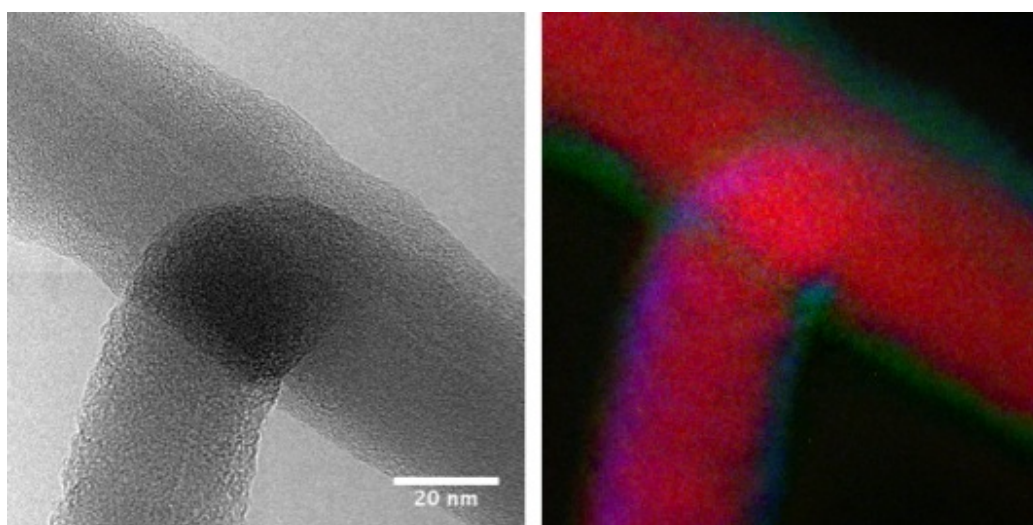


Figure 4.19: Transmission electron micrograph of a single carbon nanotube coated with 30nm of amorphous silicon. The right-hand image is false colored based on elemental abundance in the material.

Chapter 5

Oxidation and Reduction Reactions and the Graphene-Substrate Interface

This work is in the process of submission for publication with Will Regan, Will Gannett, Anna Zaniewski, Michael Crommie, and Alex Zettl.

5.1 Introduction

One particular property of graphene that has gained attention is its ability to protect an underlying substrate from oxidation or corrosion with a single or few layer[48, 66, 9]. Preliminary results on this property have generated excitement because many products would benefit from a protective coating that does not interfere with their operation. Being atomically thin and nearly transparent, graphene is a good candidate for many applications. However, previous studies have only exposed metals to very harsh oxidation conditions and measured large amounts of oxidation. Smaller levels of oxidation at room temperature and pressure through CVD-grown graphene have not been investigated. This work shows that in these conditions and on a variety of substrates, CVD-grown graphene is no longer effective at protecting from interaction with the outside environment and may catalyze corrosion.

5.2 Copper Foil Oxidation

A set of experiments investigating oxidation and reduction of copper foil under one or two layers of graphene indicates that oxidation occurs underneath a single sheet of graphene, but is inhibited by a bi-sheet graphene layer.

In order to compare the behavior of bare copper to copper with a single layer of graphene, we transferred CVD-grown graphene to part of a piece of bare copper foil

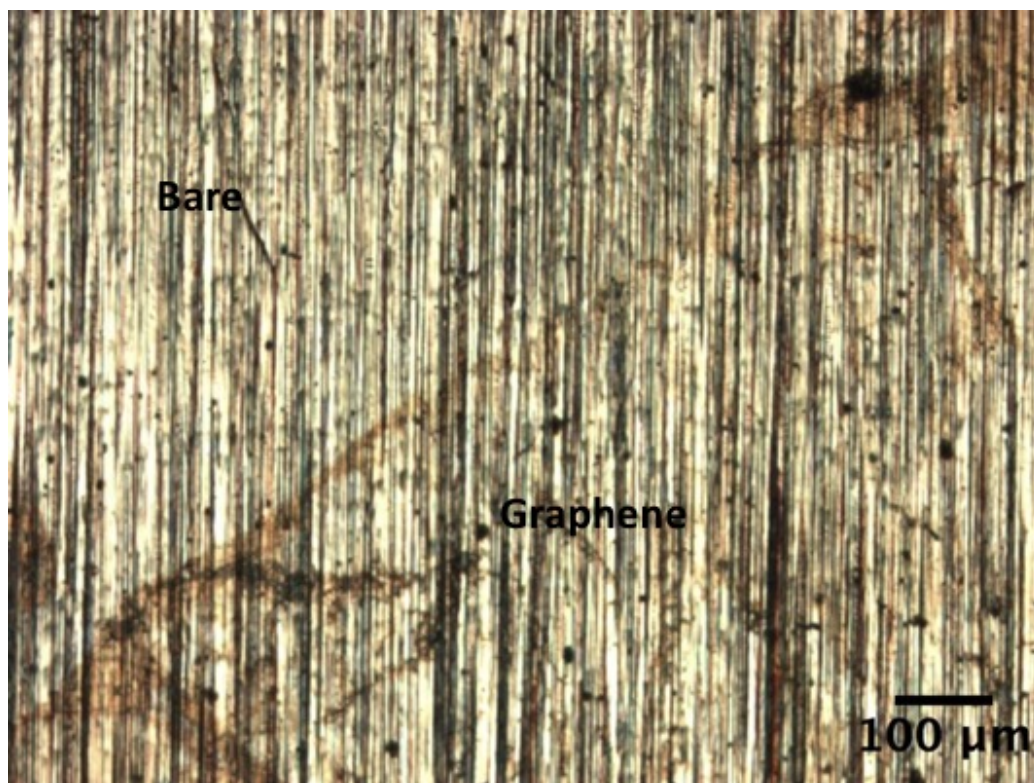


Figure 5.1: Graphene transferred onto bare copper foil and oxidized at room temperature and pressure for several weeks. Oxidation is more pronounced where graphene is present.

using a PMMA transfer. At elevated temperatures under oxygen flow, the graphene does effectively protect the copper surface, as has been observed [48]. However, a second sample was left at room temperature and ambient pressure for several weeks. In this environment, there is more oxidation under the graphene surface than where the copper is bare. Figure 5.1 shows the optical photo under a microscope of an edge area where both the bare and graphene-coated copper foil can be seen and compared. Copper oxide has a distinctly darker orange color compared to the pale orange of bare copper, so optical photos are effective at identifying oxidation. Figure 5.2 shows the Raman spectrum of this same sample, indicating that the transferred graphene is intact. Taken together, these data indicate that graphene may actually be promoting copper oxide growth through a catalysis process.

Further experiments were conducted by oxidizing and reducing copper foil with graphene grown on it by chemical vapor deposition (CVD), then taking optical photos

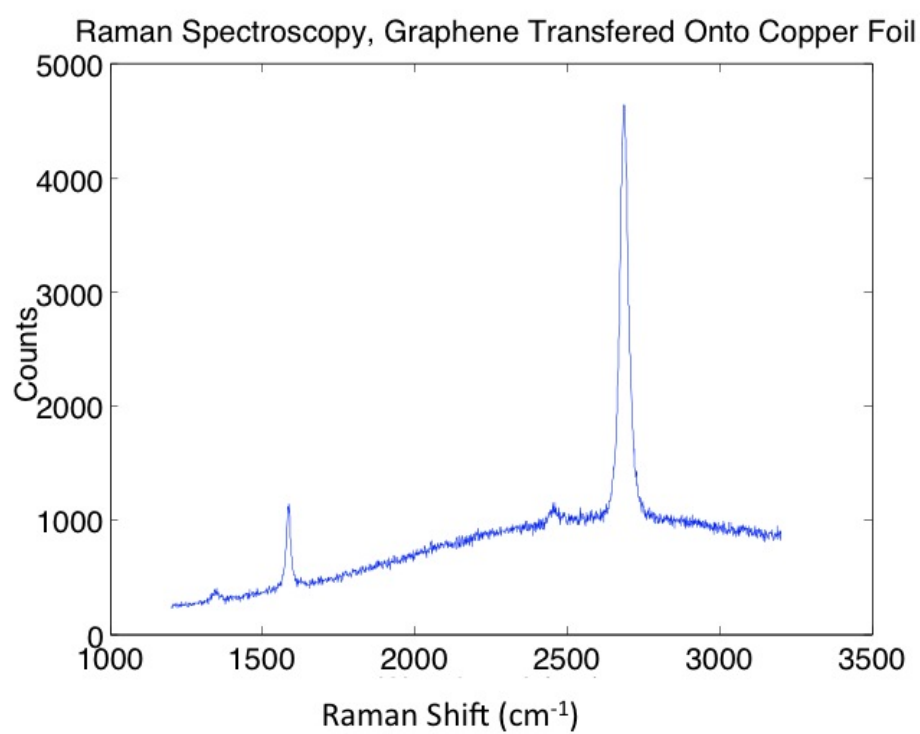


Figure 5.2: Raman spectrum of graphene transferred to copper foil indicating graphene is intact.

through a microscope to identify oxidized regions. In these experiments, oxidation and reduction were accelerated by gas flow and elevated temperature in a tube furnace system.

Figure 5.3 shows the sequence of photos taken on one piece of copper foil. The top left-hand photo is of the as-grown graphene. Some oxidation is present due to air exposure for several days between growth and measurement. Subsequently, the foil was annealed in a hydrogen environment, and reduction happened effectively through the graphene, decreasing the amount of copper oxide seen in the upper right-hand photo. Next, the foil was exposed to oxygen at elevated temperature, and a significant amount of new copper oxide can be seen in the lower right-hand photo. These first three photos are of the same place on the copper foil, identified by the shape of the copper grain boundaries, the dark lines seen on the photos. Finally a second layer of graphene was transferred on top of some parts of the as-grown graphene. When the foil was reduced by hydrogen anneal after this transfer, only the areas with only one layer of graphene were reduced. This is evidence that a second graphene layer transferred on top of the first offers significant protection to the substrate from reaction with the external environment.

We hypothesize that oxygen enters and leaves the graphene-substrate interface area through the many cracks present in CVD-grown graphene and is able to move along the interface effectively in some circumstances. In the pictures in figure 5.3, we see more effective oxidation and reduction in some copper grains when compared to others. The copper grains can be identified by the dark lines which are their boundaries. Apparently, the alignment between the substrate and graphene grain directions may significantly influence the ability of oxygen atoms or molecules to move along the surface and interact with the substrate on copper foil. Because the second layer of graphene has cracks that do not align with those of the first layer, it is effective in limiting the introduction of oxygen to the interface. Graphene grown as a bilayer would likely have cracks in the same places in both layers and would not be an effective oxidation barrier.

5.3 Electronic and Photovoltaic Performance

We also probed oxide growth through electronic performance measurements. Two parallel strips of graphene were transferred onto opposite ends of an aluminum contact. Gold contacts on the opposite ends of the graphene strips allowed us to measure the conductance of a path that necessarily required charge carriers to be transferred across a graphene-aluminum interface at both ends of the aluminum strip (Figure 5.4). Because we completed the graphene transfer in air and aluminum forms a native oxide on a very fast timescale [70], the initial conductance was extremeley

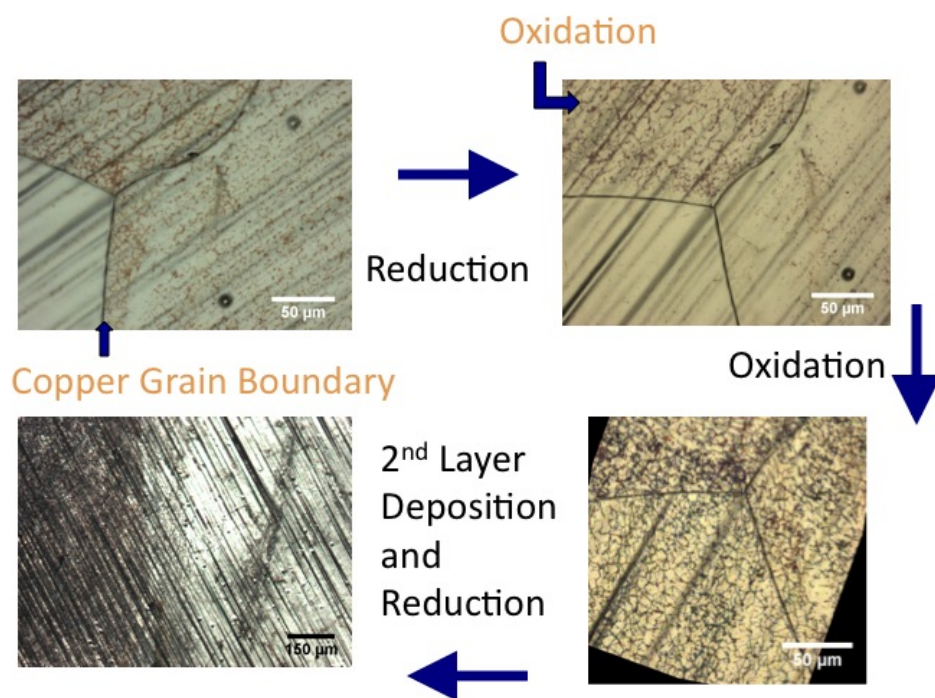


Figure 5.3: Sequence of oxidation of copper foil with graphene grown on it. Oxidation and reduction happen readily through the single as-grown layer, but transfer of a second layer of graphene protects from further oxidation.

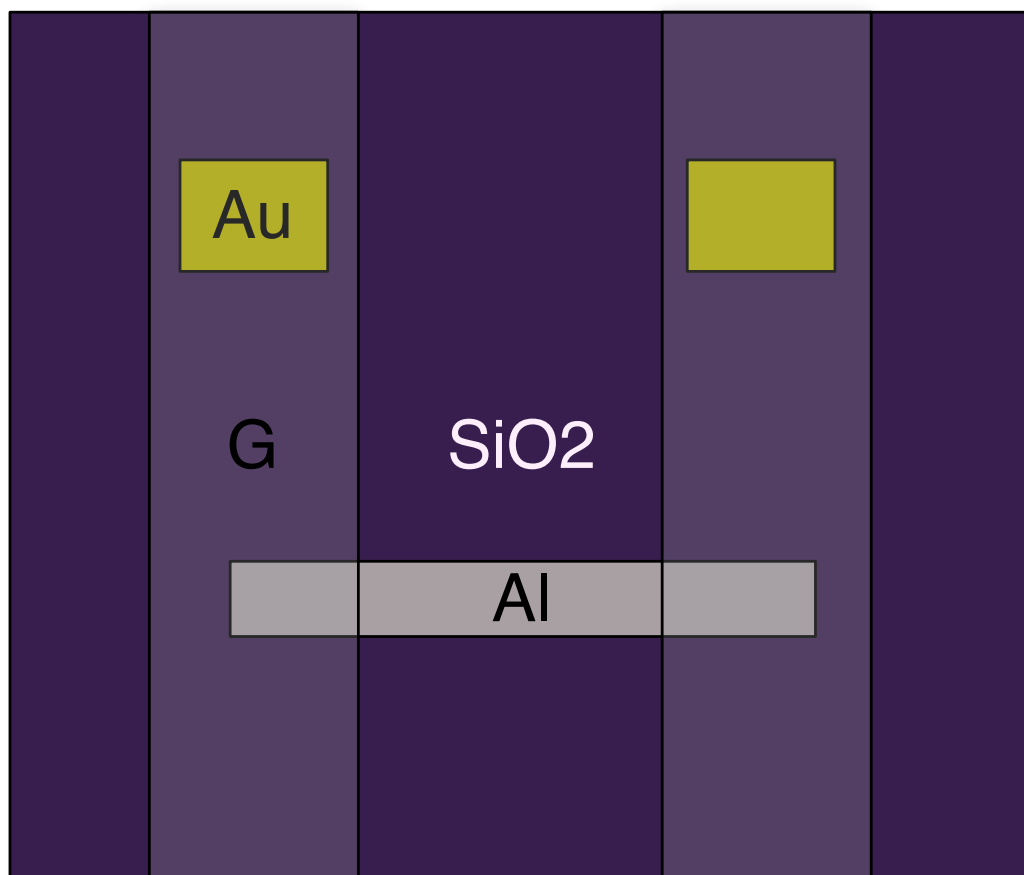


Figure 5.4: Schematic of device to investigate aluminum oxidation rate underneath graphene.

low. We annealed the entire device in hydrogen to reduce the aluminum through the graphene and immediately began measuring the conductance as a function of time. Figure 5.5 shows the rate of decay of the conductance as the aluminum forms an oxide through the graphene. The timescale for oxide formation seen here is tens of minutes, much longer than for aluminum directly exposed to air. On an aluminum substrate, graphene protects from oxidation at room temperature and ambient pressure, but is still allowing the process to happen at a slower rate.

One proposed application for large area graphene is in photovoltaics, including on silicon devices. We made silicon-graphene Schottky barrier solar cells using previously

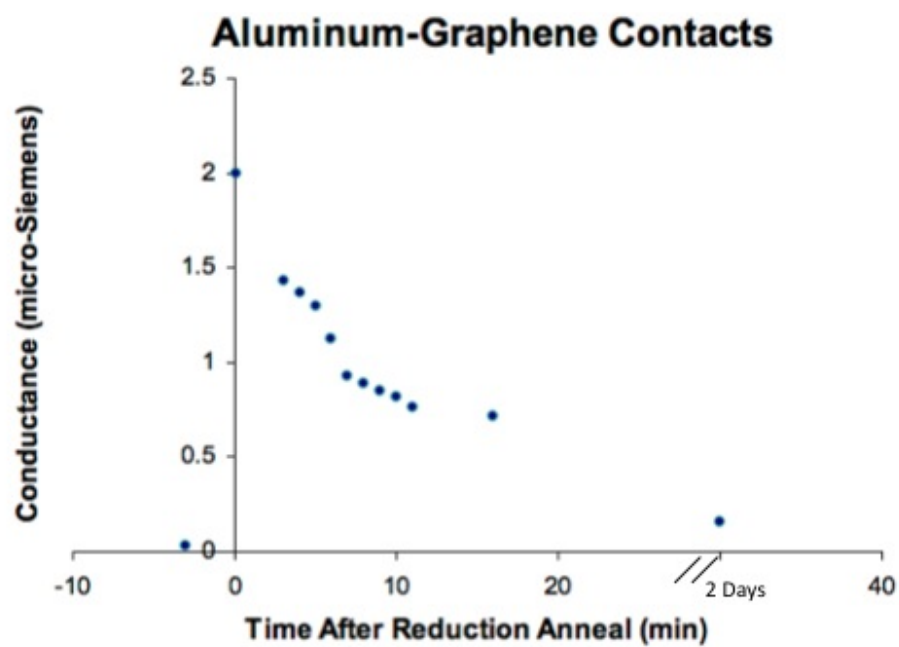


Figure 5.5: Conductance degradation in aluminum contacts over timescales of many minutes.

Table 5.1: Conditions used for RIE "descum" process before HF etch, reduction anneal, and graphene deposition.

Parameter	Value
Power	50 Watts
Chamber Size	(0.3m) ³
O ₂ Flow	60 sccm
time	60 seconds

Table 5.2: Table comparing performance degradation for mono- and bi-sheet graphene devices with n-type crystalline silicon. All entries are efficiency in percent.

Property	MSG	BSG
Initial	2.41	0.40
2 weeks	1.71	0.031
1-2 months	1.44	0.012

published methods [52]. Silicon dioxide formed at the graphene-silicon interface in these devices should hinder performance due to increased series resistance. We ensured no silicon dioxide was present initially by hydrofluoric acid-etching the silicon surface before deposition of the first layer of graphene and conducting a reduction anneal after. We compared a device with a single layer of graphene to one with a second layer deposited immediately after the reduction anneal. We additionally ensured the surface was clean by performing an RIE plasma etch clean prior to HF etching. The RIE parameters used are shown in Table 5.1. Experiments indicated that significant organic contamination is often present after photolithography and this process removes it. Figures 5.6 and 5.7 show the vastly different performance of the two devices over a period of 1-2 months. The mono-sheet graphene (MSG) device degrades quickly, while the bi-sheet graphene (BSG) device maintains most of its initial power output for many weeks.

In order to confirm that oxidation occurs at the silicon-graphene interface, we measured both bare and graphene-coated silicon wafer pieces using x-ray photoelectron spectroscopy (xps). Measurements were conducted approximately one week after a hydrofluoric acid etch of both pieces, followed by graphene transfer on one piece and a reduction anneal of both to ensure that no oxide was present. Figure 5.8 shows that the size of the oxygen and Si⁴⁺ peaks are similar in both bare and graphene-coated silicon. The graphene has provided no protection from oxidation at all. The Si⁰ peak

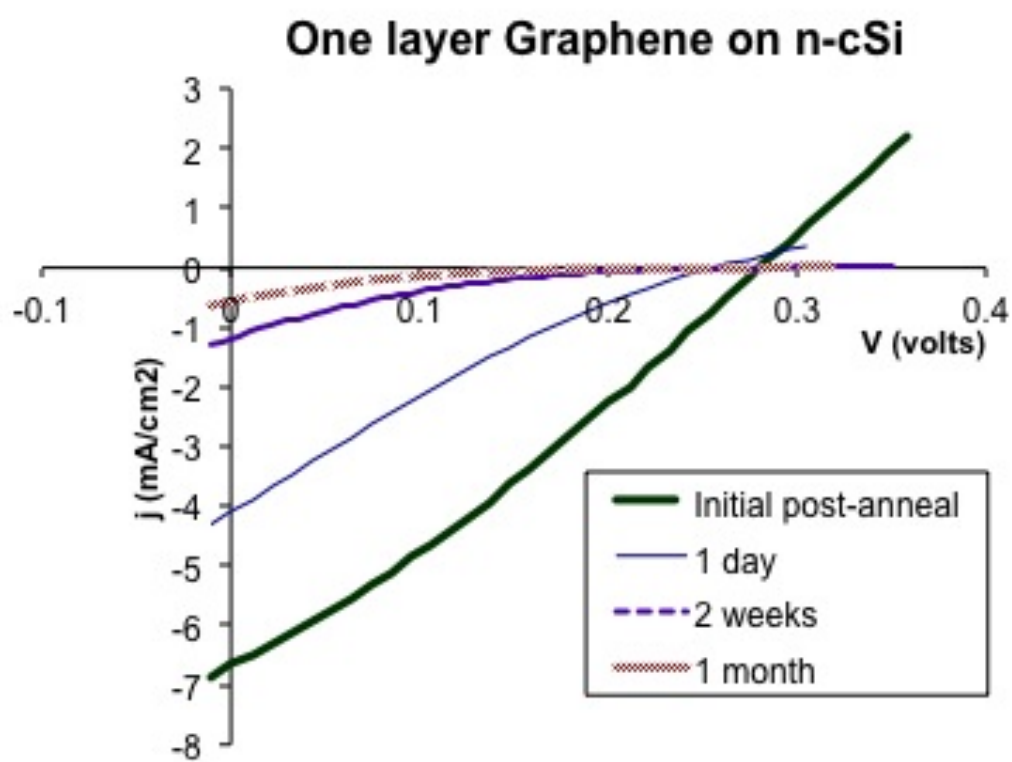


Figure 5.6: Performance degrades over time with only one layer of graphene due to oxidation of the silicon surface.

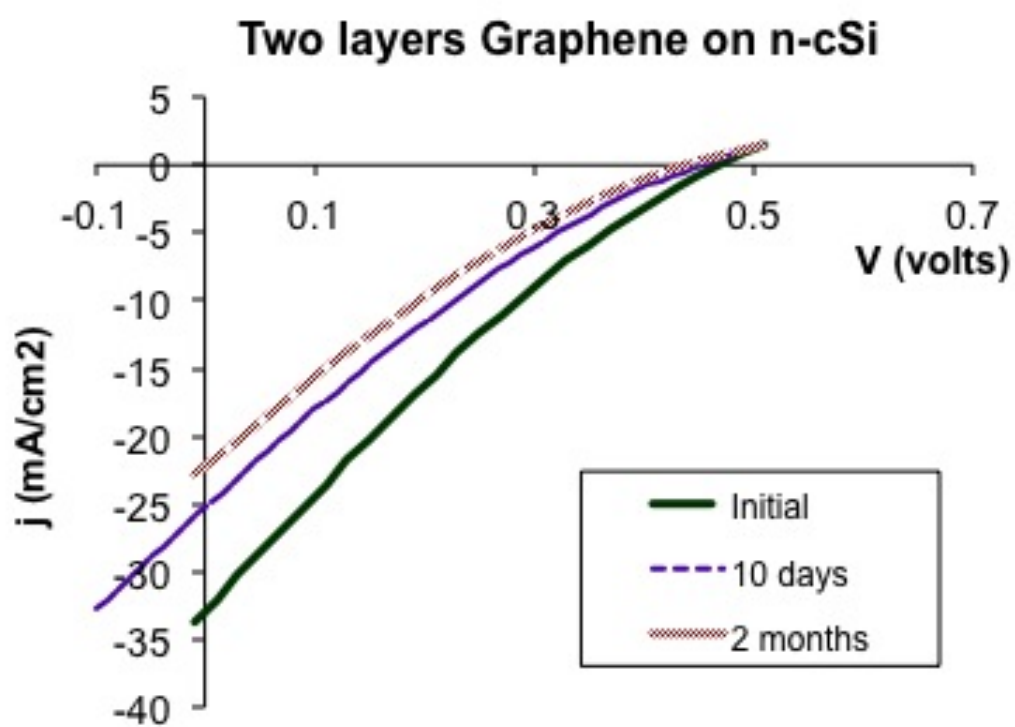


Figure 5.7: Bi-sheet graphene offers more protection from oxidation, slowing degradation.

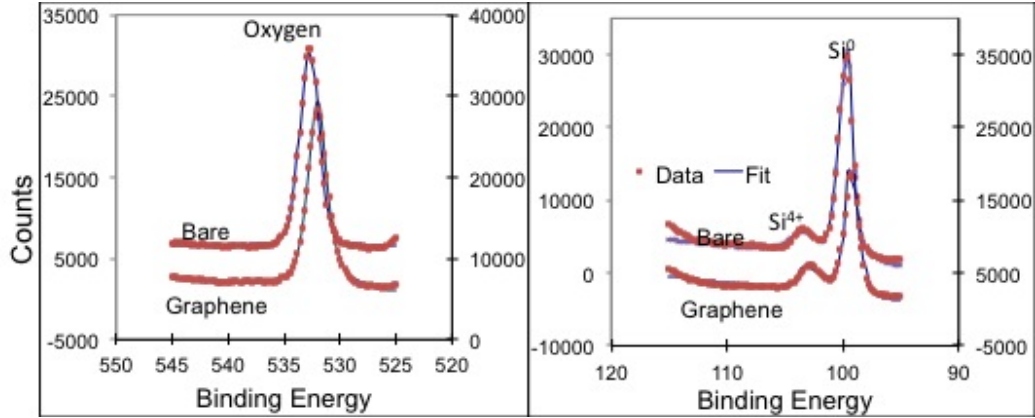


Figure 5.8: XPS results showing equal amounts of silicon dioxide on bare and graphene-coated silicon wafer substrates.

Table 5.3: XPS results. Peak sizes can be compared between MSG and BSG, but comparisons between peak sizes for different elements in the same sample are not meaningful. Peak sizes are in arbitrary units and are calculated using an Excel model to iteratively find the best Gaussian fit to data with units of counts per binding energy interval.

	Binding Energy (eV)	Bare	Graphene
Carbon	285	14337	31367
Oxygen	532	54874	61878
Si ⁴⁺	103.4	11142	12800
Si ⁰	99.53	51122	28157

is smaller in the graphene-coated device, making the Si⁴⁺/Si⁰ ratio larger, but this may be a result of the small penetration depth of the xps system, which would detect more of the silicon wafer in the device without a top coating.

5.4 Experimental Details

All graphene was grown via chemical vapor deposition (CVD) on copper foil using methane as a precursor gas. Transfer was accomplished using poly(methyl methacrylate) hardened at 165°C to mechanically stabilize the graphene and etching the copper with iron chloride (FeCl₃). Raman was conducted with a 514nm laser. Oxidation and reduction anneals were conducted in the same CVD furnace at 225°C for 60 minutes

and 450°C for 90 minutes and under oxygen and hydrogen flow, respectively. Aluminum contacts were deposited via electron beam evaporation and reduced with a standard reduction anneal immediately prior to testing. Solar cells were fabricated on commercially available degenerately phosphorous-doped silicon wafers with 300nm of silicon dioxide grown by the manufacturer. A window was etched in the oxide to access bare silicon via hydrofluoric acid immediately before graphene transfer and a reduction anneal was conducted immediately before the initial measurement for mono-sheet devices and immediately before the second graphene deposition transfer for bi-sheet devices. XPS data was collected using copper k- α radiation in a home-built system.

5.5 Conclusion

We have demonstrated that while CVD-grown graphene is effective at limiting oxidation at elevated temperatures and oxygen pressures, it does not perform this way in ambient conditions, and in all cases bisheet graphene outperforms monosheet graphene. Research aimed at developing protective layers for industrial processes must take into account this different behavior in different temperature and pressure regimes, and the possibility for graphene to catalyze oxide growth on some surfaces in some conditions.

However, this oxidation process is not only destructive, it is also an opportunity. If it can be well understood, it can be utilized to grow metal or other oxides epitaxially at accelerated rates without high temperatures.

Chapter 6

Photon Management

6.1 Light Trapping Theory

For many materials, aSi:H included, the depth of material needed to absorb virtually all incoming light is much greater than the depth from which charges can effectively be extracted. This dynamic introduces a difficult tradeoff into device design. Too thick, and most generated charges get trapped or non-radiatively recombined. Too thin, and a lot of light passes right through without being absorbed.

The goal of any light trapping device structure is to increase the amount of time photons spend in a thin layer of such an absorbing material. In turn, this allows us to use a film thin enough for extraction, while still absorbing most incoming photons. In general, this involves decoupling the direction of photon travel from the direction of charge carrier travel. In a standard solar cell design, both the photons and the charge carriers travel vertically through the cell. Many light trapping strategies, including the one presented here, function by redirecting light horizontally through the cell so it sees a longer path length along the macroscopic horizontal direction than if it continued vertically through a very thin film. In addition to providing a longer path for each pass through the cell, horizontally traveling light will intersect the top and bottom contact interfaces of the cell at oblique angles and be more likely to experience total internal reflection, allowing it to pass again through the cell and doubling its time inside. Figure 6.1 illustrates this basic idea.

Light can be redirected to a more horizontal path by two common strategies. Large scale (micron length scale) texturing of the back contact causes reflection at many angles. This strategy is very effective at increasing the time each photon spends in the absorbing material, effectively increasing the concentration of light inside the solar cell by a factor of $4n^2$ where n is the index of refraction of the material[74]. However, texturing only makes geometric sense with films that are microns thick or

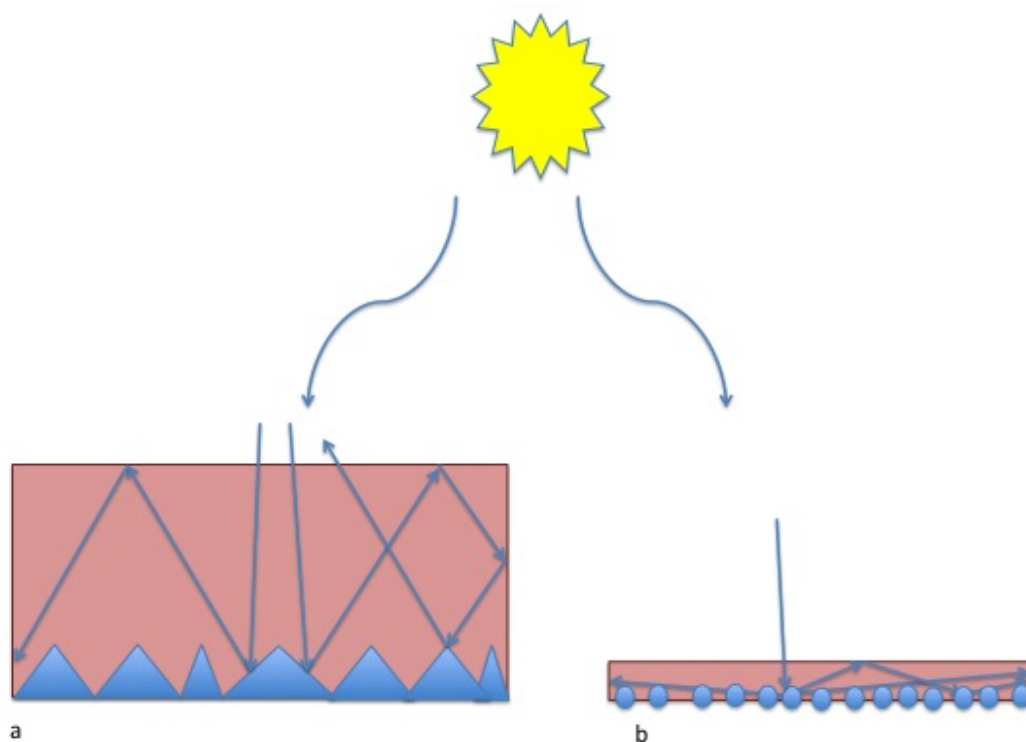


Figure 6.1: Diagram showing light trapping. Light is redirected horizontally so it spends more time in the solar cell. Figure a shows a strategy for use in relatively thick films of several microns or more. Micron-scale texturing reflects light at many angles. Figure b shows a strategy suited for thinner films. Metal nanoparticles scatter the light plasmonically with significant enhancement of the electric field near the nanoparticle film.

more. For very thin films, those thinner than the wavelength of a visible photon, features made by common texturing process such as acid etching are large compared to the film thickness[23] and the model for light concentration breaks down. For solar cells made of these materials, we turn to plasmonic scattering by metal nanoparticles.

Small metal particles are able to absorb and re-emit, or scatter, light by converting an incoming photon to a surface plasmon. A plasmon is a coherent oscillation of the electron density in a material. A surface plasmon is essentially a sloshing back and forth of the electrons along the surface of a small metal nanoparticle. Because the electrons in a metal are free, they respond quickly to electric forcing from a photon and the electric field is unable to penetrate into the bulk of the particle, restricting the plasmon to the surface.

Figure 6.2 shows a simple illustration of how a surface plasmon resonance occurs in a small metal nanoparticle. An applied electric field polarizes the nanoparticle moving electrons to one end to balance the field inside. If the applied field is removed the field induced by the displaced charges remains and forces the charge carriers to move back. They gain momentum, moving past the equilibrium field until they again create an induced field strong enough to provide a restoring force and continue oscillating at a frequency that is natural to the nanoparticle, based on its size and polarizability.

When light is incident on an array of metal nanoparticles, they experience an oscillating electric field rather than a momentary field in one direction. If the oscillation is at or near the natural frequency of charge oscillation in the particle, they respond with a resonance like a forced harmonic oscillator. This leads to a peak in extinction near the resonant frequency. Extinction is defined as $1 - \text{transmission}$, or the sum of scattering and absorption when reflection is negligible[46]. Depending on the index of refraction of the surrounding material, some of this scattered energy can be reabsorbed by nearby nanoparticles. This means that the enhanced electric field created by plasmonic scattering is significantly stronger within a few nm of the particles than further away. This super-enhancement is more than any expected attenuation of the field as a function of distance and is known as the evanescent wave or the near-field effect.

Plasmonic light trapping offers an exciting possibility for overcoming these difficulties and taking advantage of the low materials requirements and cheap, abundant starting materials used in aSi:H-graphene Schottky barrier solar cells such as the ones presented in Chapter 4. We have demonstrated significant performance improvements including a spectrally-resolved EQE enhancement peaking at 200 in these cells resulting from the addition of a film of silver nanoparticles on the top surface. In addition to modest improvements in overall absorption, the silver nanoparticles are thought to increase charge carrier generation in the top few nanometers of the cell

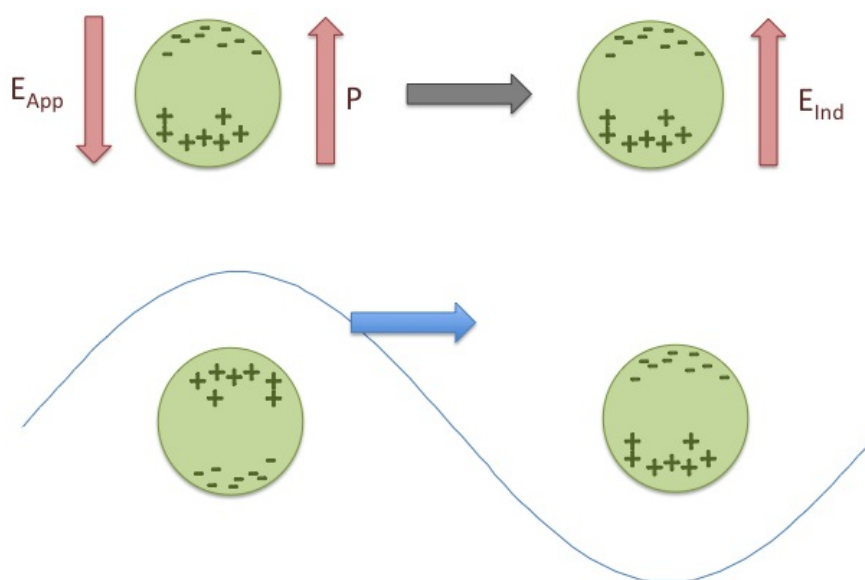


Figure 6.2: Diagram showing how surface plasmon resonance occurs in small metal nanoparticles. Incoming light has an oscillating electric field which forces free electrons in the particle to oscillate. If the frequency of the light matches the natural frequency for charge oscillation in the particle, resonance occurs.

very significantly, allowing large improvements in charge extraction. Moreover, we use a new material, tri-sheet graphene (TSG), to separate the active aSi:H material from the plasmonic silver nanoparticles, preventing shorting which occurs when silver is allowed to directly contact aSi:H. This effectively protects the active material while keeping the nanoparticles close enough to take full advantage of the near-field plasmonic effects.

6.2 Light Trapping in aSi:H

This work is in the process of submission for publication with co-authors Anna Zaniewski and Alex Zettl.

Hydrogenated amorphous silicon (aSi:H)-graphene Schottky junction cells as described in Chapter 4 promise a solution for clean electricity generation. They involve only carbon and silicon and are grown with scalable processes. However, the amorphous nature of the active material leads to significant charge trapping and extremely low charge carrier mobilities and lifetimes. The poor electrical transport characteristics mean that charge extraction is slow and ineffective and cell performance is very limited.

Researchers have established methods for fabricating working solar cells by transferring CVD-grown graphene to commercial silicon wafers[34, 15, 8]. This method can be applied to PECVD-grown aSi:H thin films to produce working photovoltaic devices[52]. However, these aSi:H devices have conversion efficiencies below 0.01%, which is far too low for any possibility of commercial application. In order to fulfill the promise of these devices, we must improve the performance by overcoming transport limitations in the aSi:H active material. Most commercial aSi:H solar cells are made with 600nm to 1 μ m of aSi:H as an absorber layer. This thickness is necessary for full absorption of perpendicularly incident light, but the average charge diffusion length in aSi:H is 2-3 orders of magnitude smaller than this thickness, preventing most charges from exiting the material[31, 21].

New investigations into plasmonic light trapping in solar cells offer a solution[22, 18, 17, 3, 19, 30, 42]. Light can be plasmonically scattered by small metal particles on the surface of the solar cell. Once scattered, light moves horizontally and can spend more time in a thinner layer of active material. For aSi:H, this means we can use much thinner absorber layers, which will improve charge extraction significantly. In addition, thinner aSi:H absorber layers are less susceptible to Staebler-Wronski degradation[10]. Recent theoretical work shows that aSi:H solar cells built with absorber layers as thin as 20nm have the potential to reach efficiencies as high as 18%, higher than standard cells commercially produced today, if light trapping is optimized[24]. While many different metal nanoparticles can be effective at light trapping[65], silver is the most investigated and has been investigated specifically for amorphous silicon cells in previously published experiments[13, 18, 26, 63].

We have used a new strategy for light trapping using silver nanoparticles in close proximity to an aSi:H-graphene Schottky barrier solar cell to drastically improve the performance of these cells.

6.3 Device Fabrication

Devices are produced by first patterning 12 nickel back contacts and one front contact on a silicon wafer coated in SiO_2 using the geometry shown in Figure 6.5. 200nm of aSi:H is deposited by PECVD on the back contacts, followed by tri-sheet graphene (TSG) on top of the aSi:H.

TSG deposition is accomplished as follows. Graphene is grown by the CVD growth method using methane as a precursor gas on copper foil[35]. The PMMA method[37] is used to transfer one layer of graphene onto another, with the lower layer of graphene still adhered on the copper foil. The PMMA coating of the top layer is not removed at this point. After drying at 60°C overnight, the two graphene layers are well-adhered and now constitute bisheet graphene (BSG). The underlying foil is etched away leaving the BSG adhered to the original PMMA coating. The BSG is transferred onto a third layer of graphene on copper foil, resulting in tri-sheet graphene (TSG). The copper foil is then etched away and the TSG is transferred onto the aSi:H substrate. This method could in principle be used to transfer TSG onto any substrate, and has the advantage of not introducing PMMA contamination between graphene layers. In addition, this is a more efficient fabrication process than using a PMMA deposition-liftoff process for each layer.

A schematic of the TSG deposition process is shown in Figure 6.3.

Because the copper is a thin foil, it is difficult to use it to "pick up" graphene out of solution in the same way we do with a rigid substrate. To work around this issue, I laid the copper to be deposited on along the bottom of a foil petri dish. The foil dishes are better than glass ones because the bottoms are flat, whereas glass petri dishes have a geometric peak in the middle. With a foil dish, I can even make the bottom a little bit concave to match the shape of the foil. Because graphene-coated copper is hydrophobic, it's important not to get any water underneath the foil or it will immediately move to the top of the water. It's important for the foil to lay as close as possible to the bottom of the dish along its whole area. I pipette deionized water on top of the foil until it is submerged, then use a teflon spoon to transfer the PMMA-coated MSG or BSG onto the top of the water. Finally, I remove the water with a pipette until the MSG or BSG rests on top of the underlying foil. I pipette as much water as possible out of the drop that inevitably forms along the copper surface. If there is too much, it will strain the just-transferred graphene as it dries.

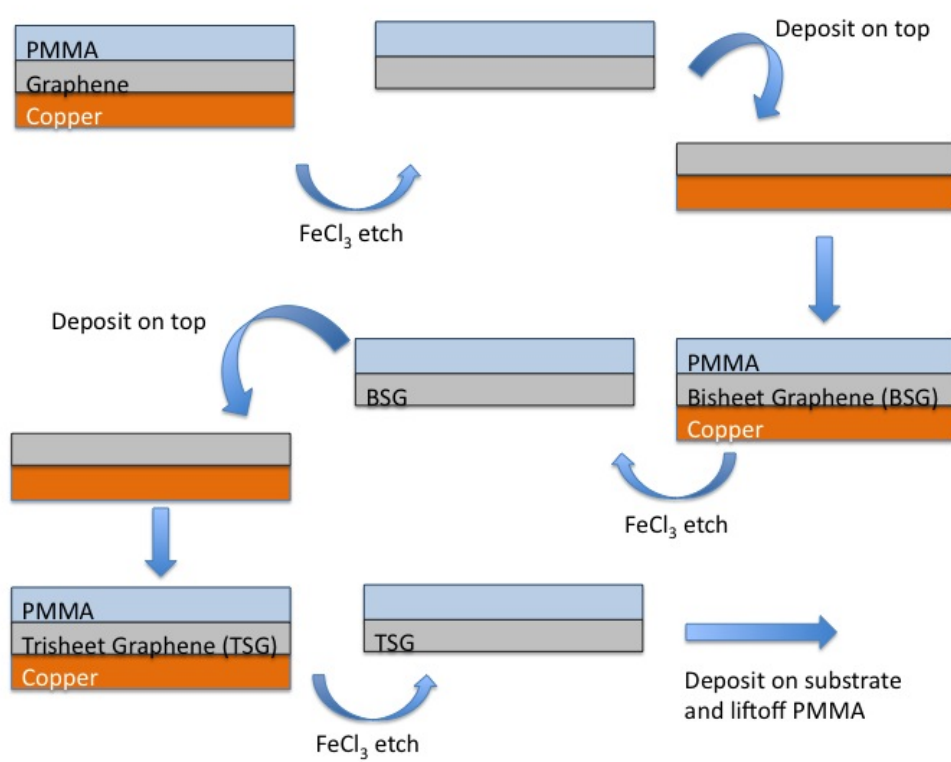


Figure 6.3: Deposition process for tri-sheet graphene (TSG).

We tested TSG using Raman spectroscopy to determine whether it behaved similarly to mono- or to multi-layer graphene. The results are inconclusive as measurements in 15 different places on a small 1cm^2 TSG sample deposited on quartz show multiple examples of both behaviors. Figure 6.4 shows the results.

After TSG deposition, the devices are working solar cells and are tested using a Newport xenon lamp with a filter installed to produce a spectrum similar to AM1.5 illumination. Subsequently, 5nm of silver is thermally evaporated on 6 of the 12 devices, leaving the remainder as controls. Control devices are protected from silver deposition by an aluminum foil shadow mask, but they are on the same substrate as the experimental devices and undergo the same pressure, temperature, and other environmental changes during the thermal evaporation process. Liquid nitrogen is used to cool the sample stage during silver deposition and prevent heat-induced shunting. Silver films deposited this way naturally de-wet and form 50-200nm nanoparticles as shown in Figure 6.6. The particles are not monodisperse and take on a variety of morphologies. They form domains with different densities and average particle size, which can be seen in the series of micrographs in Figure 6.6. The devices are tested again and the performance of the silver nanoparticle enhanced devices is compared to the bare ones.

This dewetting process leads to particles with a variety of sizes, which is expected given the uncontrolled nature of the process. The particles naturally organize themselves into domains with dimensions of tens of microns with abrupt borders between domains (Figure 6.6, (b,c,d)). The relationship between domains of nanoparticle size and crystal domains of the substrate materials is unknown. However we expect that they are related to the substrate surface chemistry in some way, and notice that domain edges often occur at the edge of the nickel contacts, although they also occur in places with no obvious change in substrate composition.

6.4 Results and Discussion

6.4.1 Performance

Figure 6.7 shows the short circuit current and efficiency for devices with silver nanoparticles (experimental cells) compared to control devices.

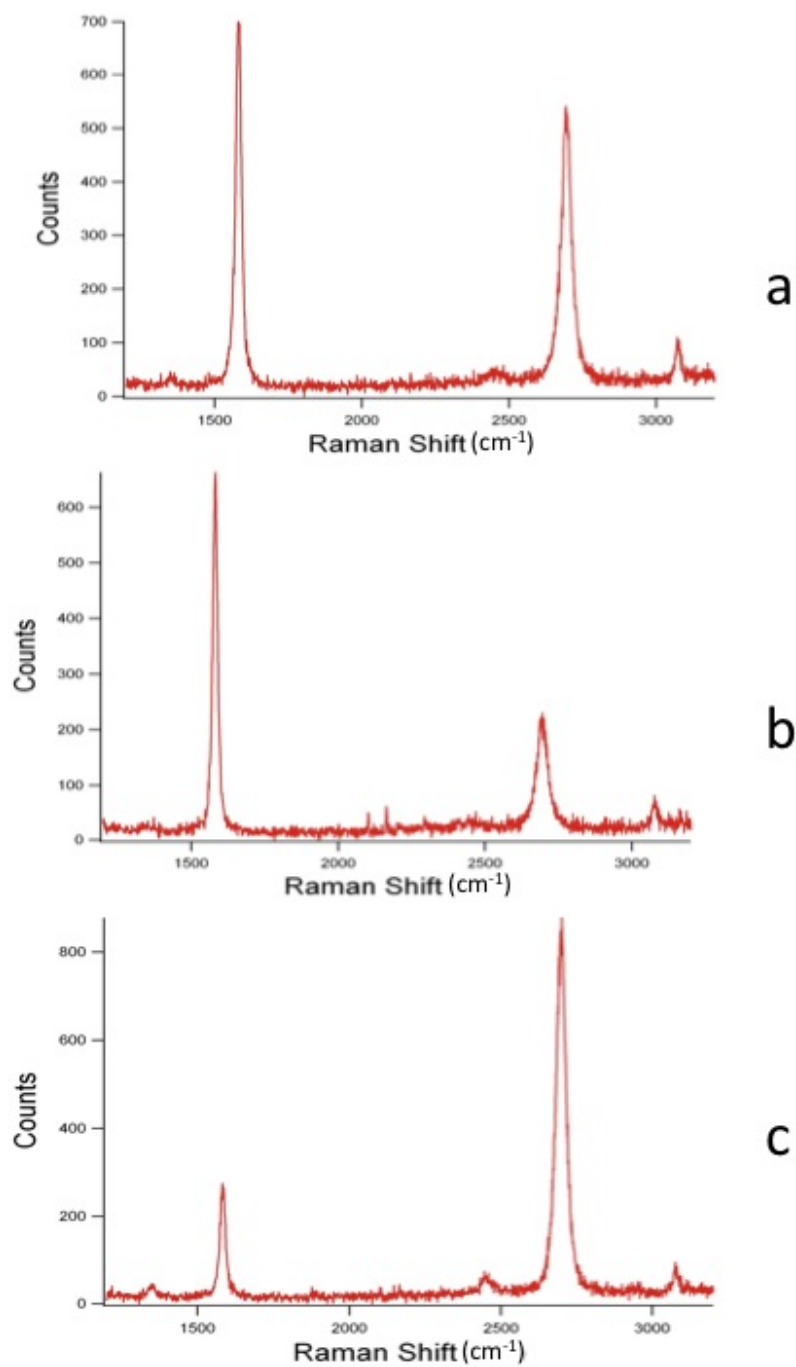


Figure 6.4: Raman spectrum of tri-sheet graphene (TSG). Some areas look like mono-layer graphene (c) while some look like few-layer graphene (b).

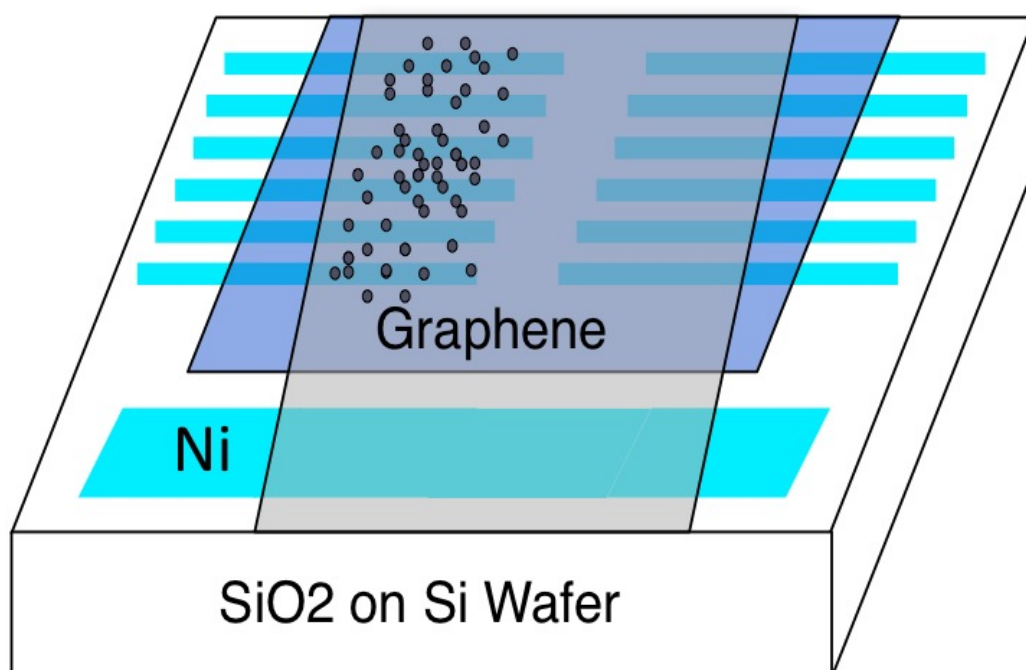


Figure 6.5: A schematic of device structure. 12 separate devices are fabricated in parallel by patterning 12 back contacts, then depositing aSi:H, graphene, and finally silver nanoparticles.

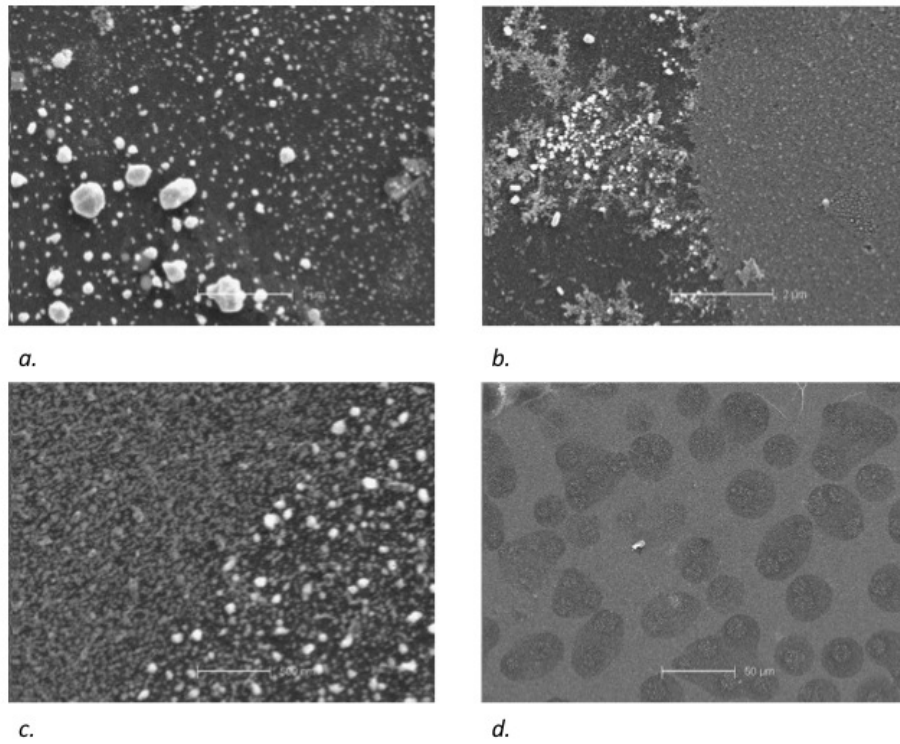


Figure 6.6: SEM micrographs of a device with silver nanoparticles deposited by thermal evaporation of 5nm thick silver film. (a) shows particle sizes. (b) and (c) show abrupt borders between domains of different particle sizes. (d) shows large-area variability and domain size.

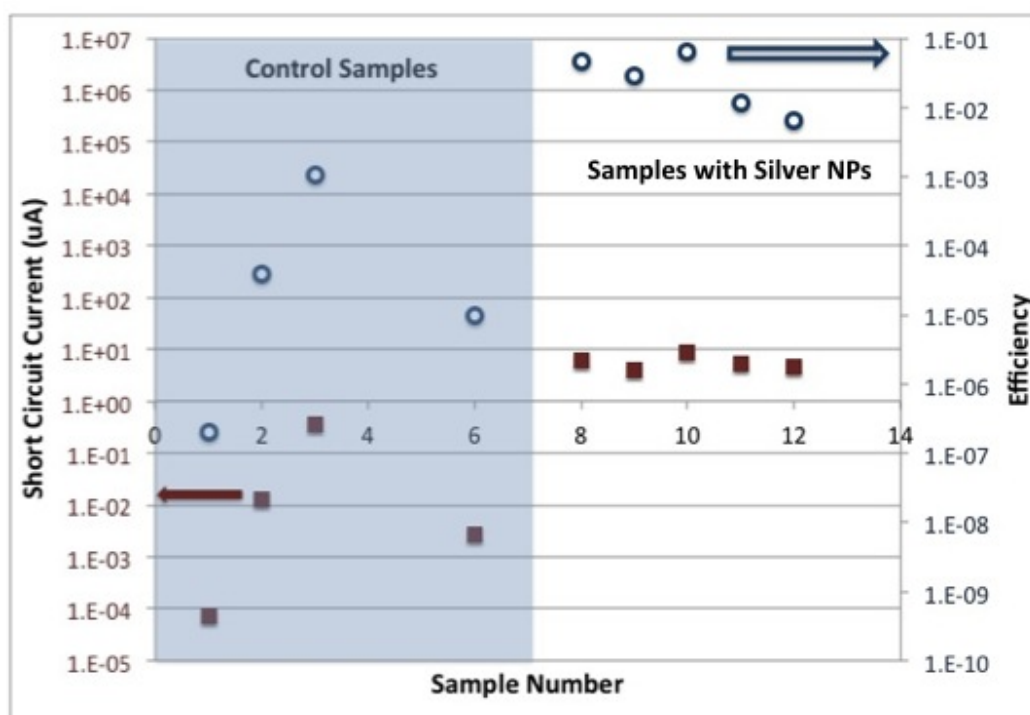


Figure 6.7: Short circuit current and efficiency in cells with and without silver nanoparticles. Data points on the left-hand side represent individual control devices, while those on the right represent experimental devices with silver nanoparticles.

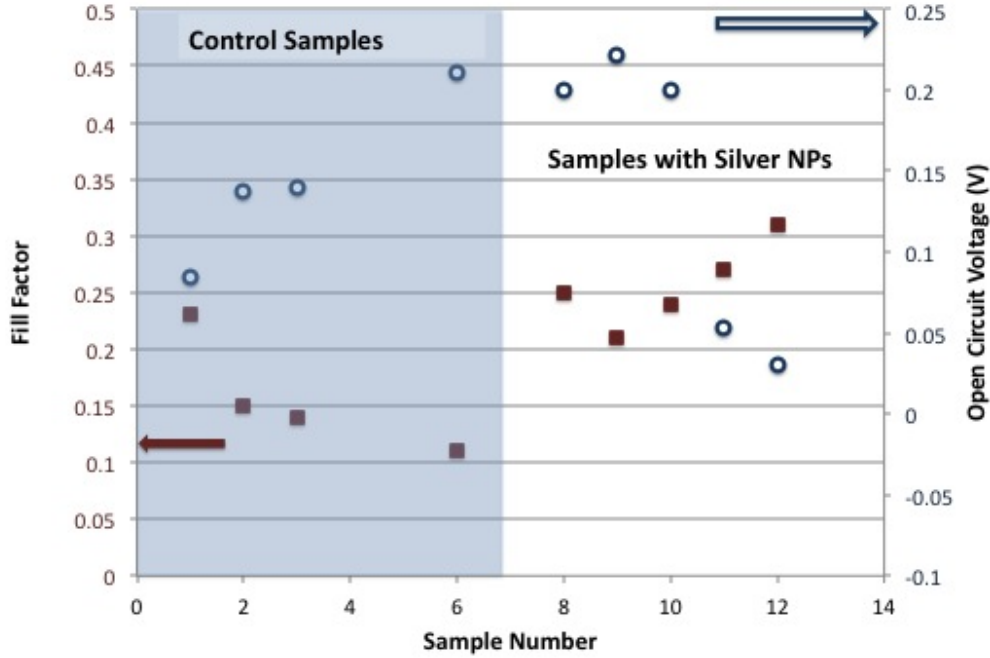


Figure 6.8: Comparison of open circuit voltage and fill factor performance for control and experimental devices.

We see a significant performance improvement in cells with silver nanoparticles. Because our films are 200nm thick to prevent shorting, we believe most of this enhancement comes from concentrating absorption in a smaller region at the top surface of the aSi:H film. Because transport in these films is hole-limited[60] and holes are extracted by the top graphene film[52], carriers generated closer to the top of the film are extracted with much higher efficiency than ones generated deeper in the film. 200nm of aSi:H should absorb a high fraction of incident light so overall absorption is only enhanced a small amount.

Figure 6.8 shows the open circuit voltages (V_{oc}) and fill factors for experimental and control devices. V_{oc} in these devices is highly influenced by shunt paths through the aSi:H layer, so we don't see a clear relationship with silver nanoparticle presence. Fill factor, a measure of the ideality of the diode, is generally very small in previously reported Schottky barrier devices between graphene and both aSi:H and crystalline silicon. Previous publications have reported fill factors less than 0.25 although no coherent theory explains these results. In the devices presented here, we see a moderate improvement in fill factor with silver nanoparticle deposition. We also attribute this to enhanced carrier generation very near the graphene-aSi:H interface, which results in a higher fraction of carriers with enough energy to overcome low-energy traps and be extracted at voltages close to V_{oc} .

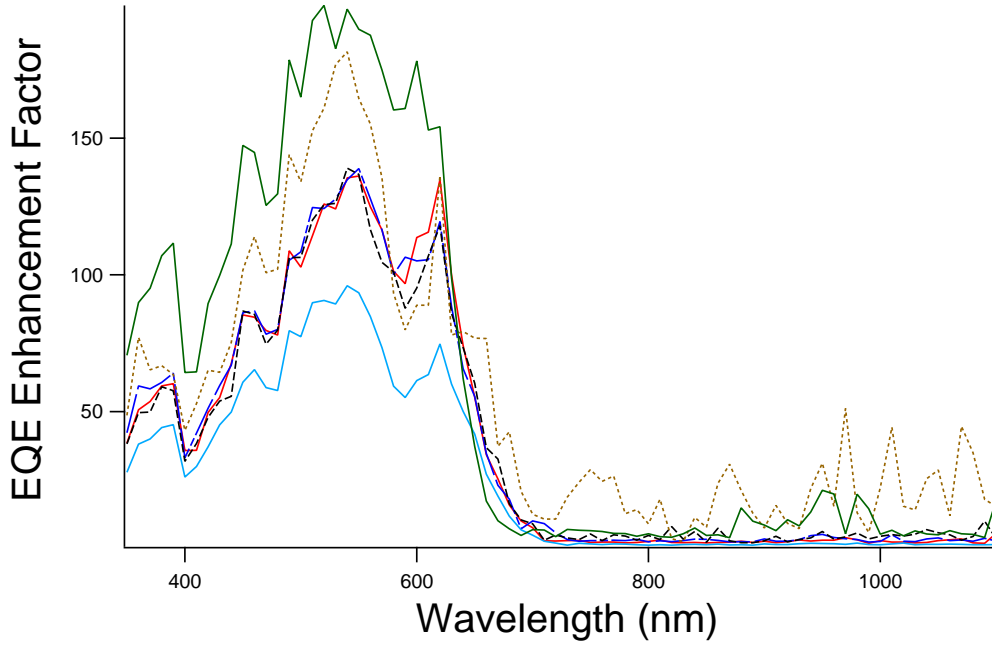


Figure 6.9: External quantum efficiency (EQE) enhancements for devices with silver nanoparticles compared to average control device EQE.

6.4.2 Spectral Performance

External quantum efficiency (EQE) measurements were taken for each device shown in Figures 6.8 and 6.7. For each experimental device, the EQE spectrum was divided by the average EQE spectrum for all control devices to calculate an enhancement factor. The results are shown in Figure 6.9. We see two distinct peaks in the enhancement factor spectra. One is at about 375 nm and one is at about 550 nm. Mie theory modeling conducted by A Zaniewski supports the existence of plasmon resonance peaks in these regions, and we expect that that slight variation in peak placement among devices results from the lack of monodispersity and large domains of nanoparticles of different sizes discussed above and shown in Figure 6.6.

To investigate the extent to which EQE enhancement is due to overall absorption enhancement, we measured absorption spectra in the ultraviolet and visible ranges of 30nm aSi:H films with and without a TSG-AgNP top coating fabricated as described above. We divided the absorption of the treated films by the absorption of the bare films to obtain an enhancement factor as a function of wavelength of incident light.

The results are shown in Figure 6.10. We now see a peak at 475 nm, but it is much smaller than the peaks seen in the EQE spectra. This is a further indication that the performance enhancements we see in the photovoltaic devices result not primarily from enhanced overall absorption, but from enhanced absorption near the TSG-aSi:H interface leading to enhanced charge extraction.

In considering the absorption spectra of the films with and without nanoparticles, we determine that the enhancement must be a result of the near-field electric field enhancement discussed above. We start with a simple model involving a constant wavelength-dependent absorption coefficient throughout the material, and an enhancement of the path length with nanoparticle deposition. In this case, absorption is:

$$A(\omega) = 1 - T = 1 - \frac{I(\omega)}{I_0} = 1 - e^{-\alpha(\omega)*l} \quad (6.1)$$

Then the absorption enhancement at a given ω is

$$\frac{A_{np}}{A} = \frac{1 - e^{-\alpha * l_{np}}}{1 - e^{-\alpha * l}} \quad (6.2)$$

where T is transmission, reflection is assumed to be negligible, I and I_0 are transmitted and initial light intensities, α is the absorption coefficient and l and l_{np} are the path length without and with nanoparticles.

For thick materials, l approaches ∞ , and expression 6.2 trends towards 1. This means that for thick aSi:H layers, most of the light will be absorbed with or without nanoparticles, and the enhancement will be negligible. For small values of l , the top and bottom of 6.2 both approach zero, so we use l'Hopital's rule to find

$$\frac{A_{np}}{A} \Rightarrow \frac{\alpha * l_{np} * e^{-\alpha * l_{np}}}{\alpha * l * e^{-\alpha * l}} \quad (6.3)$$

which reduces to

$$\frac{A_{np}}{A} \Rightarrow \frac{l_{np}}{l} \quad (6.4)$$

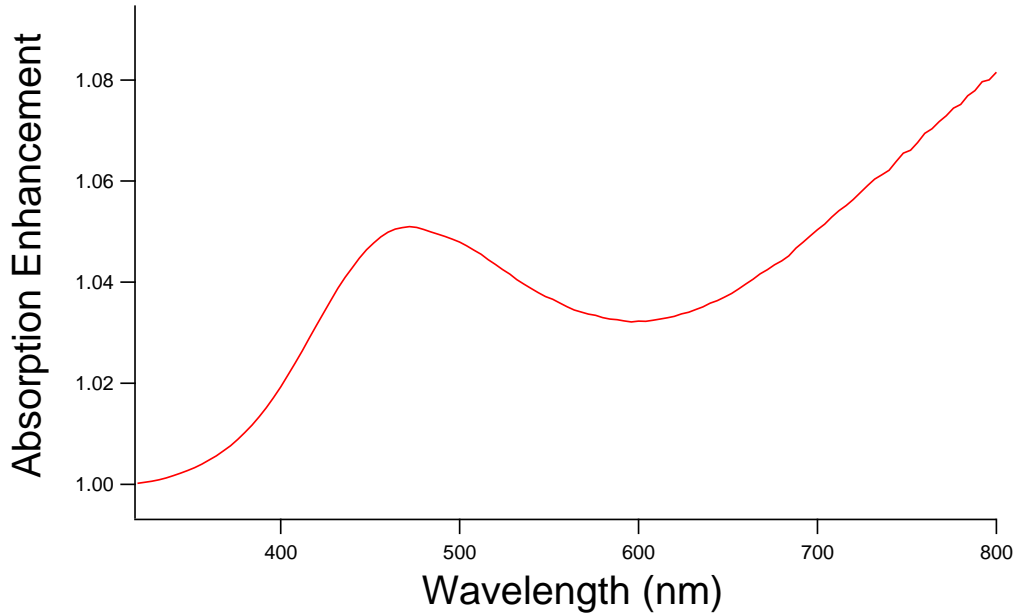


Figure 6.10: Absorption enhancement in 30nm aSi:H coated with tri-sheet graphene and silver nanoparticles, compared to 30nm aSi:H with no top coating.

Meaning that the absorption enhancement, even for very thin films, would not rise above the path length enhancement if this model were comprehensive. Using the original data and equation 6.1, we extract the path length enhancement as a function of wavelength shown in Figure 6.11. At visible wavelengths, the enhancement is larger than in Figure 6.10 for sure, but cannot account for the enhancement seen in Figure 6.9. We conclude that additional enhancement represents very significant near-field effects.

6.5 Conclusion

The addition of a silver nanoparticle layer to the top of aSi:H-graphene Schottky barrier solar cells significantly enhances their performance. Using three sheets of graphene prevents silver ion motion through the aSi:H active layer, which would short the devices. The significant performance enhancement cannot be explained simply by increased light absorption, implying a very substantial increase in absorption in the very thin layer near the top graphene contact of the cell. When most charge carriers are generated in this area, extraction improves greatly as easily trapped holes have a much shorter distance to travel before being extracted into the graphene.

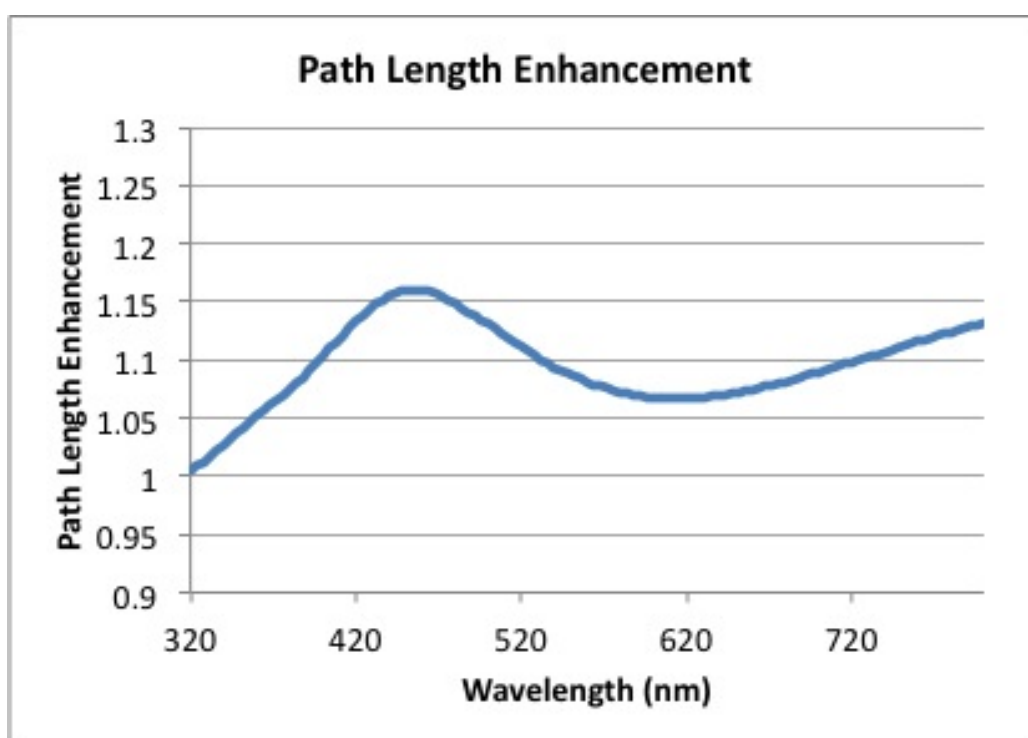


Figure 6.11: Calculated path length enhancement in arbitrarily thin aSi:H coated with tri-sheet graphene and silver nanoparticles, compared to aSi:H with only graphene.

Chapter 7

Conclusion

I have developed a novel solar cell architecture to address the growing problems associated with energy generation via combustion of fossil fuels. The photovoltaic design presented in this thesis takes advantage of abundant, non-toxic materials to produce electricity. Although initial measurements showed weak performance, treatments including oxidation protection and light trapping enhanced power conversion efficiency.

In addition to the potential for broad application within the energy industry, the experiments in this thesis present fascinating questions and answers about our physical world. The interaction of a carbon nanostructure with a thin amorphous film to separate excited charges, the tendency of thin metal films to naturally create ideal broad-band light scattering layers, and the process by which copper interacts with ambient gases through, and with the help of, a graphene covering are examples of the new interesting science contained in this thesis. These ideas have applications throughout materials science research, including optical devices, corrosion control, and controlled growth of oxides, independent of photovoltaic applications.

Future directions for this research should address improving the quality of the aSi:H absorber layer in order to allow for thinner cells to be fabricated without the risk of pinhole shorting. In addition, the light trapping and tri-sheet graphene protective layer strategies outlined here can be applied to a wide array of solar cells and other devices to improve performance.

Bibliography

- [1] P. K. Acharya, H. D. Banerjee, K. L. Chopra, S. C. Saha, and Swati Ray. Effect of hydrogen dilution in silane on light induced degradation of hydrogenated amorphous silicon films for solar photovoltaic applications. *Solar Energy Materials and Solar Cells*, 32:21–28, 1994.
- [2] Energy Information Administration. International energy outlook. 2011.
- [3] Y. A. Akimov and W. S. Koh. Tolerance study of nanoparticle enhancement for thin-film silicon solar cells. *Applied Physics Letters*, 99(6):3, 2011.
- [4] LG De Arco, Y Zhang, A Kumar, and CW Zhou. Synthesis, transfer, and devices of single- and few-layer graphene by chemical vapor deposition. *IEEE Transactions on Nanotechnology*, 8(2):135–138, 2009.
- [5] European Photovoltaics Industry Association. Epia annual report. 2011.
- [6] The Atlantic. Here comes the sun. Jun 26 2008.
- [7] L Brey and H. A. Fertig. Electronic states of graphene nanoribbons. *Physical Review B*, 73:235411, 2006.
- [8] CX Chen, Y Lu, ES Kong, YF Zhang, and ST Lee. Nanowelded carbon-nanotube-based solar microcells. *SMALL*, 4(9):1313–1318, 2008.
- [9] S. S. Chen, L. Brown, M. Levendorf, W. W. Cai, S. Y. Ju, J. Edgeworth, X. S. Li, C. W. Magnuson, A. Velamakanni, R. D. Piner, J. Y. Kang, J. Park, and R. S. Ruoff. Oxidation resistance of graphene-coated Cu and Cu/Ni alloy. *ACS Nano*, 5(2):1321–1327, 2011.
- [10] K.L. Chopra, P.D. Paulson, and V. Dutta. Thin-film solar cells: An overview. *Progress in Photovoltaics: Research and Applications*, 12:69–92, 2004.
- [11] Eduardo Cruz-Silva, Florentino Lopez-Urias, Emilio Munoz-Sandoval, Bobby G. Sumpter, Humberto Terrones, Jean-Christophe Charlier, Vincent Meunier, and Mauricio Terrones. Electronic transport and mechanical properties of phosphorus- and phosphorus-nitrogen-doped carbon nanotubes. *ACS Nano*, 3(7):1913–1921, 2009.

- [12] Pablo A Denis, Ricardo Faccio, and Alvaro W. Mombru. Is it possible to dope single-walled carbon nanotubes and graphene with sulfur. *ChemPhysChem*, 10:715–722, 2009.
- [13] C. Eminian, F. J. Haug, O. Cubero, X. Niquille, and C. Ballif. Photocurrent enhancement in thin film amorphous silicon solar cells with silver nanoparticles. *Progress in Photovoltaics*, 19(3):260–265, 2011.
- [14] M Endo, H Muramatsu, T Hayashi, YA Kim, M Terrones, and NS Dresselhaus. 'buckypaper' from coaxial nanotubes. *Nature*, 433:476, Feb 2005.
- [15] TT Feng, D Xie, YX Lin, YY Zang, TL Ren, R Song, HM Zhao, H Tian, X Li, HW Zhu, and LT Liu. Graphene based schottky junction solar cells on patterned silicon-pillar-array substrates. *Applied Physics Letters*, 99(23), 2011.
- [16] TT Feng, D Xie, YX Lin, HM Zhao, Y Chen, H Tian, TL Ren, X Li, Z Li, KL Wang, DH Wu, and HW Zhu. Efficiency enhancement of graphene/silicon-pillar-array solar cells by HNO₃ and PEDOT-PSS. *Nanoscale*, 4:2130–2133, 2012.
- [17] Vivian E. Ferry, Jeremy N. Munday, and Harry A. Atwater. Design considerations for plasmonic photovoltaics. *Advanced Materials*, 22(4794-4808), 2010.
- [18] Vivian E. Ferry, Marc A. Verschuuren, Hongbo B. T. Li, Ewold Verhagen, Robert J. Walters and Ruud E. I. Schropp, Harry A. Atwater, and Albert Polman. Light trapping in ultrathin plasmonic solar cells. *Optics Express*, 18(S2), June 2010.
- [19] H. W. Gao, C. Liu, H. E. Jeong, and P. D. Yang. Plasmon-enhanced photocatalytic activity of iron oxide on gold nanopillars. *ACS Nano*, 6(1):234–240, 2012.
- [20] Hong-Zhang Geng, Dae Sik Lee, Ki Kang Kim, Gang Hee Han, Hyeon Ki Park, and Young hee Lee. Absorption spectroscopy of surfactant-dispersed carbon nanotube film: Modulation of electronic structures. *Chemical Physics Letters*, 455:275–278, 2008.
- [21] Adolf Goetzberger, Christopher Hebling, and Hans-Werner Schock. Photovoltaic materials, history, status and outlook. *Materials Science and Engineering Reports*, 40:1–46, 2003.
- [22] M. A. Green and S. Pillai. Harnessing plasmonics for solar cells. *Nature Photonics*, 6(3):130–132, 2012.
- [23] R. Groenen, J. Löffler, J.L. Linden, R.E.I. Schropp, and M.C.M. van de Sanden. Property control of expanding thermal plasma deposited textured zinc oxide with focus on thin film solar cell applications. *Thin Solid Films*, 1-2(492):298–306, December 2005.

- [24] Viktoria Gusak, Bengt Kasemo, and Carl Hagglund. Thickness dependence of plasmonic charge carrier generation in ultrathin a-Si:H layers for solar cells. *ACS Nano*, 5(8), 2011.
- [25] HX Hu, ZH Zhang, XH Liu, M Qiu, and KH Ding. Tight binding studies on the electronic structure of graphene nanoribbons. *Acta Physica Sinica*, 58(10):7156–7161, OCT 2009.
- [26] Z. S. Hu, F. Y. Hung, S. J. Chang, K. J. Chen, Y. W. Tseng, B. R. Huang, B. C. Lin, W. Y. Chou, and J. Chang. Improvement of n-ZnO/p-Si photodiodes by embedding of silver nanoparticles. *Journal of Nanoparticle Research*, 13(10):4757–4763, 2011.
- [27] Yi-Fan Huang, Surojit Chattopadhyay, Yi-Jun Jun, Cheng-Yu Peng, Tze-An Liu, Yu-Kuei Hsu, Ci-Ling Pan, Hung-Chun Lo, Chih-Hsun Hsu, Yuan-Huei Chang, Chih-Shan Lee, Kuei-Hsien Chen, and Li-Chyong Chen. Improved broadband and quasi-omnidirectional anti-reflection properties with biomimetic silicon nanostructures. *Nature Nanotechnology*, 2:770–774, December 2007.
- [28] S. Iijima. *Nature*, 354(56), 1991.
- [29] Y Jia, JQ Wei, KL Wang, AY Cao, QK Shu, XC Gui, YQ Zhu, DM Zhuang, G Zhang, BB Ma, LD Wang, WJ Liu, ZC Wang, JB Luo, and D Wu. Nanotube-silicon heterojunction solar cells. *ADVANCED MATERIALS*, 20(23):4594–4598, 2008.
- [30] J. Kim, A. J. Hong, J. W. Nah, B. Shin, F. M. Ross, and D. K. Sadana. Three-dimensional a-Si:H solar cells on glass nanocone arrays patterned by self-assembled Sn nanospheres. *ACS Nano*, 6(1):265–271, 2012.
- [31] C. Koch, M. Ito, and M. Schubert. Low-temperature deposition of amorphous silicon solar cells. *Solar Energy Materials and Solar Cells*, 68:227–236, 2001.
- [32] Mei-Ling Kuo, David J. Poxson, Yong Sung Kim, Frank W. Mont, Jong Kyu Kim, E. Fred Schubert, and Shawn-Yu Lin. Realization of a near-perfect antireflection coating for silicon solar energy utilization. *Optics Letters*, 33(21):2527–2529, 2008.
- [33] W. Z. Li, S. S. Xie, L. X. Qian, B. H. Chang, B. S. Zhou, W. Y. Zhou, R. A. Zhao, and G. Want. Large-scale synthesis of aligned carbon nanotubes. *Science*, 274:1701–1703, December 1996.
- [34] Xinmin Li, Honwei Zhu, Kunlin Wang, Anyuan Cao, Jinqian Wei, Chunyan Li, Yi Jia, Zhen Li, Xiao Li, and Dehai Wu. Graphene-on-silicon schottky junction solar cells. *Advanced Materials*, 22:2743–2748, 2010.

- [35] XS Li, WW Cai, JH An, S Kim, J Nah, DX Yang, R Piner, A Velamakanni, I Jung, E Tutuc, SK Banerjee, L Colombo, and RS Ruoff. Large-area synthesis of high-quality and uniform graphene films on copper foils. *SCIENCE*, 324(5932):1312–1314, 2009.
- [36] XS Li, CW Magnuson, A Venugopal, JH An, JW Suk, BY Han, M Borysiak, WW Cai, A Velamakanni, YW Zhu, LF Lu, EM Vogel, E Voelkl, L Colombo, and RS Ruoff. Graphene films with large domain size by a two-step chemical vapor deposition process. *Nano Letters*, 10(11), 2010.
- [37] Xuesong Li, Yanwu Zhu, Weiwei Cai, Mark Borysiak, Boyang Han, David Chen, Richard D. Piner, Luigi Colombo, and Rodney S. Ruoff. Transfer of large-area graphene films for high-performance transparent conductive electrodes. *Nano Letters*, 9(12):4359–4363, 2009.
- [38] ZR Li, VP Kunets, V Saini, Y Xu, E Dervishi, GJ Salamo, AR Biris, and AS Biris. $SOCl_2$ enhanced photovoltaic conversion of single wall carbon nanotube/n-silicon heterojunctions. *APPLIED PHYSICS LETTERS*, 93(24):–, 2008.
- [39] H. Liu, Yunqi Liu, and Daebon Zhu. Chemical doping of graphene. *Journal of Materials Chemistry*, 21:3335–3345, 2011.
- [40] Steven G. Louie. *Topics in Applied Physics*, volume 80. Springer-Verlag, 2001.
- [41] Antonio Luque and Steven Hegedus. *Handbook of Photovoltaic Science and Engineering*. John Wiley and Sons, 2003.
- [42] L. Muller-Meskamp, Y. H. Kim, T. Roch, S. Hofmann, R. Scholz, S. Eckardt, K. Leo, and A. F. Lasagni. Efficiency enhancement of organic solar cells by fabricating periodic surface textures using direct laser interference patterning. *Advanced Materials*, 24(7), 2012.
- [43] R. R. Nair, P. Blake, A. N. Grigorenko, K. S. Novoselov, T. J. Booth, T. Stauber, N. M. R. Peres, and A. K. Geim. Fine structure constant defines visual transparency of graphene. *SCIENCE*, 320(5881):1308, June 2008.
- [44] G. Nandamuri, S. Roumimov, and R. Solanki. Chemical vapor deposition of graphene films. *Nanotechnology*, 21(14):4, 2010.
- [45] Jenny Nelson. *The Physics of Solar Cells*. Imperial College Press, 2003.
- [46] Cecilia Noguez. Surface plasmons on metal nanoparticles: The influence of shape and the physical environment. *Journal of Physical Chemistry C*, 111(10):3806–3819, February 2007.

- [47] K. S. Novoselov, A. K. Geim, S. V Morozov, D. Jiang, Y. Zhang, S. V. Dubonos, I. V. Grigorieva, and A. A. Firsov. Electric field effect in atomically thin carbon films. *SCIENCE*, 306(5696):666–669, OCT 2004.
- [48] D. Prasai, J. C. Tuberquia, R. R. Harl, G. K. Jennings, and K. I. Bolotin. Graphene: Corrosion-inhibiting coating. *ACS Nano*, 6(2):1102–1108, 2012.
- [49] The Sunshot Program. One dollar per watt photovoltaic systems workshop summary, 2010.
- [50] D. Ritter, K. Weiser, and E. Zeldov. Steady-state photocarrier grating technique for diffusion-length measurement in semiconductors: Theory and experimental results for amorphous silicon and semi-insulating GaAs. *Journal of Applied Physics*, 62(11):4563–4570, 1987.
- [51] AV Rozhkov, S Savel’ev, and Franco Nori. Electronic properties of armchair graphene nanoribbons. *Physical Review B*, 79(12), MAR 2009.
- [52] M Schriver, W Regan, M Loster, and A Zettl. Carbon nanostructure-aSi:H photovoltaic cells with high open-circuit voltage fabricated without dopants. *Solid State Communications*, 150(13-14):561–563, 2010.
- [53] Thomas Seyllor. <http://www.graphene.nat.uni-erlangen.de/grapheneng.htm>, 6/28/2011.
- [54] A.V. Shah, R. Platz, and H. Keppner. Thin-film silicon solar cells: A review and selected trends. *Solar Energy Materials and Solar Cells*, 38:501–520, 1995.
- [55] Shuran Sheng, Xianbo Liao, Zhixun Ma, Guozhen Yue, Yongqian Wang, and Guanglin Kong. Hydrogenated amorphous silicon films with significantly improved stability. *Solar Energy Materials and Solar Cells*, 68:123–133, 2001.
- [56] W. Shockley and H.J. Queissar. *Journal of Applied Physics*, 32:510, 1961.
- [57] Wim Simke. Photovoltaic solar energy.
- [58] Solarbuzz, 2012.
- [59] Y. W. Son, M. L. Cohen, and S. G. Louie. Energy gaps in graphene nanoribbons. *Physical Review Letters*, 97:216803, 2006.
- [60] W. E. Spear. The study of transport and related properties of amorphous silicon by transient experiments. *Journal of Non-Crystalline Solids*, 59:1–14, 1983.
- [61] D. L. Staebler and C. R. Wronski. Reversible conductivity changes in discharge-produced amorphous si. *Applied Physics Letters*, 31(4):292–294, 1977.

- [62] Nidhi Subbaraman. Flexible touch screen made with printed graphene. *Technology Review*, June 21 2010.
- [63] Hairen Tan, Rudi Santbergen, Arno H. M. Smets, and Miro Zeman. Plasmonic light trapping in thin-film silicon solar cells with improved self-assembled silver nanoparticles. *Nano Letters*, page DOI: 10.1021/nl301521z, 2012.
- [64] Bo Tang, Hu Guoxin, and Hanyang Gao. Raman spectroscopy characterization of graphene. *Applied Spectroscopy Reviews*, 45(5), 2010.
- [65] T. L. Temple and D. M. Bagnall. Optical properties of gold and aluminium nanoparticles for silicon solar cell applications. *Journal of Applied Physics*, 109(8):13, 2011.
- [66] M. Topsakal, H. Sahin, and S. Ciraci. Graphene coatings: An efficient protection from oxidation. *Physical Review B*, 85(15):7, 2012.
- [67] M. A. Tsai, H. W. Han, Y. L. Tsai, P. C. Tseng, P. C. Yu, H. C. Kuo, C. H. Shen, J. M. Shieh, and S. H. Lin. Embedded biomimetic nanostructures for enhanced optical absorption in thin-film solar cells. *Optics Express*, 19(14):A757–A762, 2011.
- [68] Vincent C Tung, Li-Min Chen, Matthew J Allen, Jonathon K. Wassei, Kurt Nelson, Richard B. Kaner, and Yang Yang. Low-temperature solution processing of graphene-carbon nanotube hybrid materials for high-performance transparent conductors. *Nano Letters*, 9(5):1949–1955, 2009.
- [69] USGS, 2002.
- [70] Lenntech B. V. Aluminum - (Al) - chemical properties, health and environmental effects. <http://www.lenntech.com/periodic/elements/al.htm>.
- [71] Lucas K. Wagner and Jeffrey C. Grossman. Microscopic description of light induced defects in amorphous silicon solar cells. *Physical Review Letters*, 101:265501, 2008.
- [72] Xuan Wang, Linjie Zhi, and Klaus Mullen. Transparent, conductive graphene electrodes for dye-sensitized solar cells. *Nano Letters*, 8(1):323–327, 2008.
- [73] Peter Würfel. *Physics of Solar Cells*. Wiley-VCH, 2005.
- [74] E Yablonovitch and GD Cody. Intensity enhancement in textured optical sheets for solar-cells. *IEEE Transactions on Electron Devices*, 29(2), 1982.
- [75] L. Yarris. *science@berkeleylab*, 11/30/2007.

- [76] Jong-Hwan Yoon and Kee-Tae Lee. Light-induced effects in hydrogenated amorphous silicon films grown from high hydrogen dilution of silane. *Journal of Non-Crystalline Solids*, 299-302:487–491, 2002.
- [77] S. Zhang, X. Liao, L. Raniero, E. Fortunato, Y. Xu, G. Kong, H. Aguas, I. Ferreira, and R. Martins. Silicon thin films prepared in the transition region and their use in solar cells. *Solar Energy Materials and Solar Cells*, 90:3001–3008, 2006.